028

TEK LABS

INTEGRATED OPTICS AND APPLICATION

Cathy Lin-Hendel

027

APPLIED RESEARCH

TECHNICAL REPORT

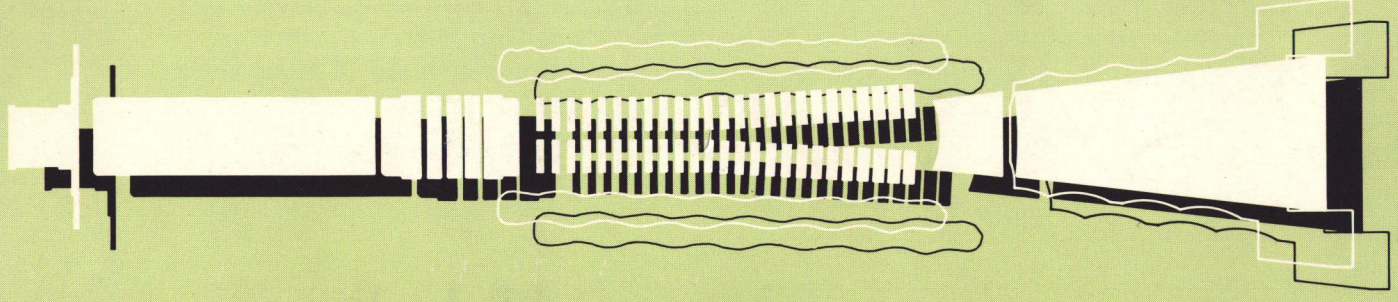

TEK PRIVATE

TEKTRONIX®

INTEGRATED OPTICS AND APPLICATION

Cathy Lin-Hendel

021

August 30, 1981

PREFACE

This report is written for several purposes. First, it should serve as a guide and reference for continuous work in integrated optics in Technology Group. Second, it should serve as an introduction of the field and its potential applications to the managers and engineers in Business Divisions. Finally, it should serve as a state-of-the-art report and a recommendation to the management.

It has not been easy for me to accommodate all three purposes. A good compromise nonetheless is achieved. Chapter 1 involves mainly introductory and review material. Chapter 2 summarizes the coupling methods. Chapter 3 and 4 review the state-of-the-art of acoustooptics and electrooptics and disclose several unique applications for Tektronix. Chapter 5 summarizes the optical sources and detectors and their important characteristics. Recommendation for Tek involvement in this area is also summarized in Section 5.3.

It is not possible to cover all the aspects of technologies and applications related to integrated optics with one report. Through the course of study, I have investigated areas such as optical nonlinearity in semiconductors for direct light amplifications, and two-dimensional Fourier transform for image processing. These subjects are excluded because of their relatively immature or impractical status, or their lack of uniqueness or room for innovation at Tek. There may also be some areas I have overlooked. In such case, please accept my apologies.

All chapters in this report are relatively independent of one another. Readers are encouraged to pick topics of their interest, if the available time is limited. Readers who intend to be technically involved in integrated optics and fiber optics or their applications should read all chapters. Comprehensive refer-

ence listings are also prepared for these readers.

A summary is written for higher level technology managers, in which specific sections disclosing unique applications are listed. When time allows, consultations to other sections and chapters would be helpful.

I am indebted to my manager, Robert Li, for his guidance, his continuous interest, and mostly, his understanding of what is involved in such a task, which allowed me the luxury of time and freedom to do a good job. I thank Emmanuel Sang, Arnie Frisch, Rudi Hendel and Tom Reeder for reading the manuscript and for their helpful comments. I also would like to express my sincere appreciation to Anne Schultz, whose excellent UNIX "gurutise" and her patience have made my writing a pleasant experience. Anne's contribution to this report is invaluable. I also thank Caryl MacMillan for her help in the final completion.

SUMMARY

As optical fiber communications technology becomes mature, integrated optics is emerging to be a viable technology for solving bandwidth problems in many data acquisition, signal processing, data transmission applications in test and measurement instruments and systems. This report reviews the state-of-the-art of integrated-optics and related technologies, and discloses their unique potential applications at Tektronix.

Section 3.4, Subsection 3.4.5 in particular, describes an application in hard-copying, where acoustooptic Bragg diffraction is used to deflect a character shaped laser beam to desired position on a printing medium.

Section 3.5 describes a novel method to parallelly route switch a large number of optical video programs to a large number of receiving channels, using acoustooptic Bragg diffraction.

Section 4.5 describes a novel electro-optic approach to achieve similar capability in routing switch optical video signals. This approach uses simpler mechanism, and its device easier to fabricate. However, the performance is next to the acoustooptic approach.

Section 4.6 describes several novel approaches to solving a problem of long-standing at Tek--the circuit probing and testing problem. The magnitude of the benefit of these inventions could be very large to Tektronix. However, the magnitude of the effort needed to implement these inventions is also large.

Section 5.3 describes integrated semiconductor laser array, integrated semiconductor transistor laser, and integrated repeater array as worthwhile applications of GaAs technology to electrooptics.

If a good program is established to pursue some of the above-mentioned applications, the spin-off benefits will be large, especially in the areas of data transmission and ultra-high-speed signal sampling.

I recommend a program involving both technology and device teams, and further employ systems team when initial feasibility of devices is proven. Table I categorizes the program from a technology and device point of view, and relate the devices to the application areas. Table II and III categorize the program from systems point of view, and relate systems applications to devices and technologies needed. It is important that the program manager is able to comprehend both viewpoints. The program team should have a balance of processing and fabrication engineers, test and measurement engineers, physicists, optical engineers and system designers and related technicians. Very high speed photo-detection is not necessary at this point yet. However, if it becomes a requirement (10's of psec) in the future, amorphous silicon photodetectors could be a viable solution.

I also recommend patent applications being filed for the contents of sections 3.4.2, 3.4.3, 3.5, 4.5 and 4.6.

Table I

INTEGRATED-OPTICS PROGRAM

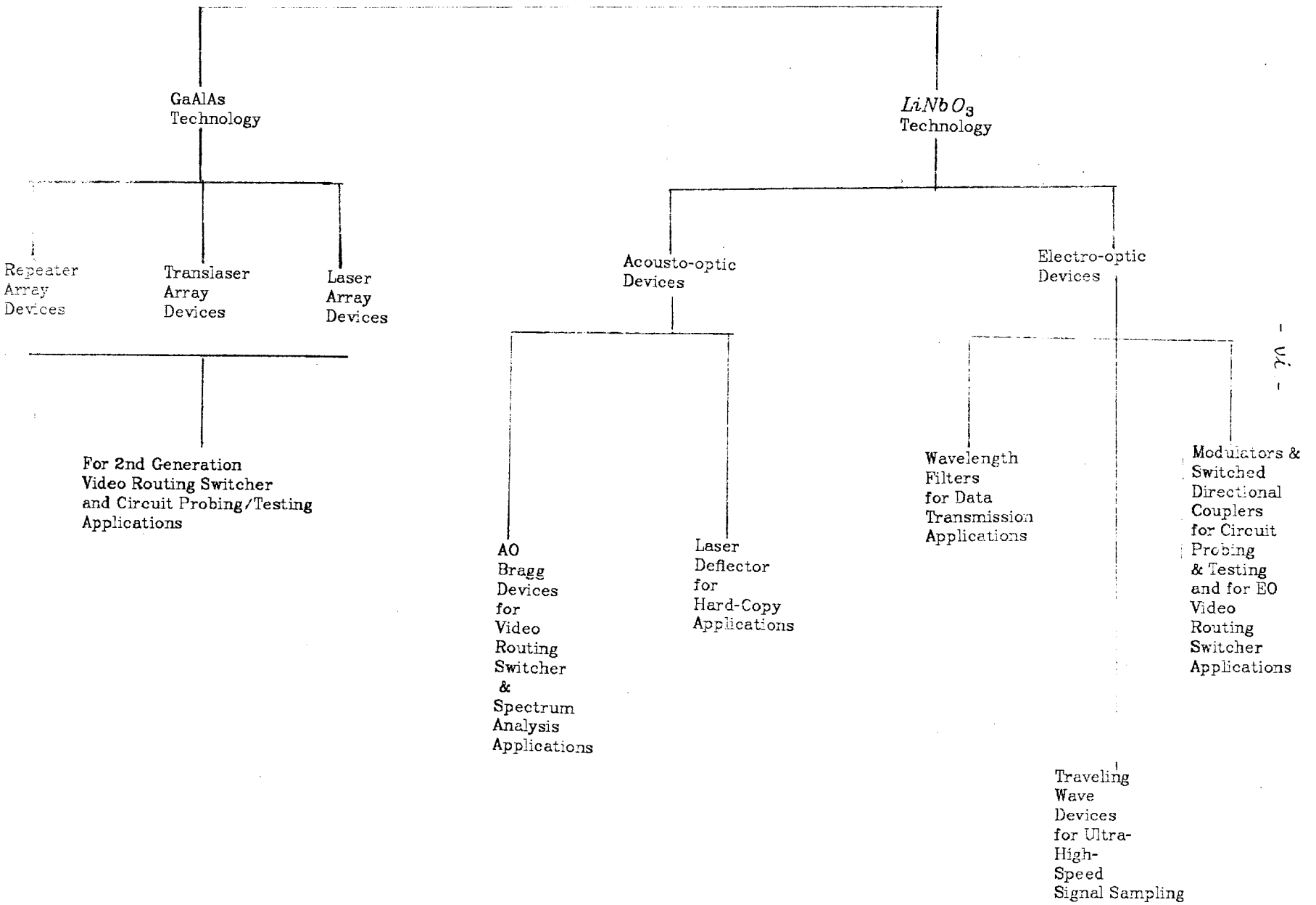

Table II

INTEGRATED-OPTICAL

STIMULUS/RESPONSE CIRCUIT PROBE

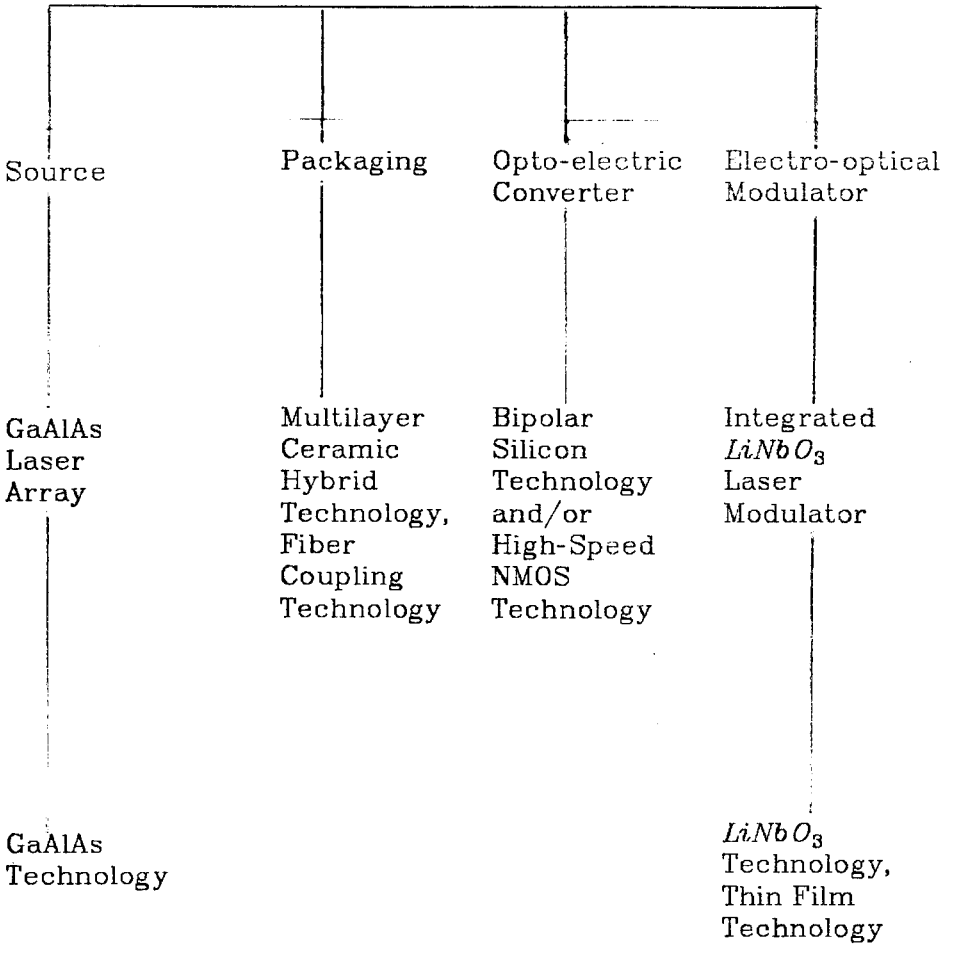

Table III

AO
DIGITAL VIDEO ROUTING SWITCHER

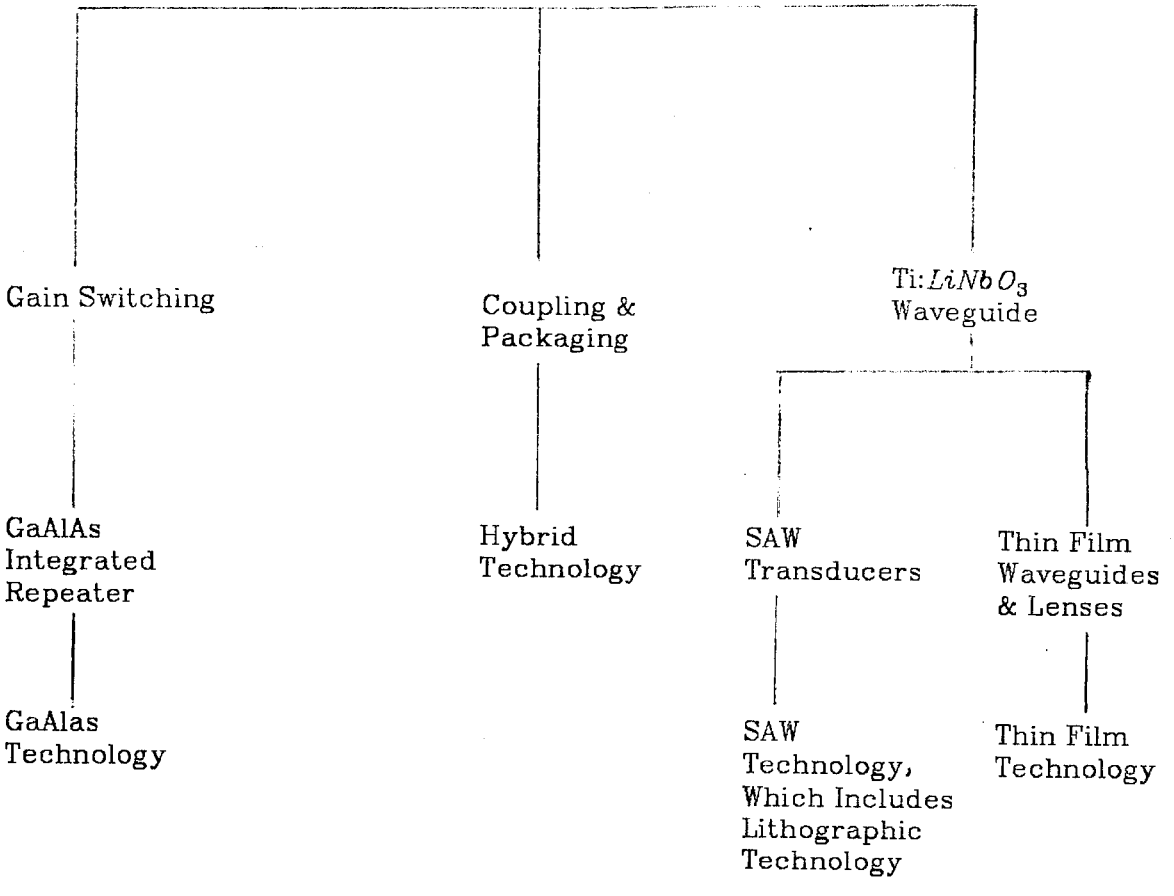

TABLE OF CONTENTS

TABLE OF ILLUSTRATIONS

LIST OF TABLES

CHAPTER 1

INTRODUCTION

1.1 Communications, Optical Signal Processing and Integrated Optics

1.1.1 Light Wave as a Signal Carrier

The very high frequency of light waves ($10^{14} \sim 10^{15}$ Hz, 10^4 to 10^5 times higher than the frequency of microwaves) makes light waves a signal with immense information carrying capacity. A 10^4 fold increase in information capacity and processing speed is theoretically possible. Besides the large increase in **bandwidth**, there are also other important advantages to be considered, such as **immunity to electro-magnetic interferences, cable cross talk** and **ground loop problems.**

1.1.2 Light Wave Communications

Historically, the main barriers to the realization of optical communications were the lack of an economical coherent source and the lack of a low loss, low cost light transmission medium. Gas lasers, already well advanced during the 1960s, required high power, high current operation and massive cooling systems. Light waves traveling in atmosphere suffer tremendous loss, spatial spread and dispersion due to absorption, scattering and diffraction of light in the atmosphere.

The rapid improvements experienced in the development of GaAs based semiconductor heterojunction lasers and low loss (<0.2dB/km - 1.dB/km) opti-

cal fibers during the last few years have definitely brought lightwave communications to practice. Fiber optical transmission and data communications systems are already proven superior at many installations (Table 1-1,1-2)[1]. Bell System has announced the "Northeast Corridor Program" to service Boston-Washington, D.C., area (~600 miles) with 80,000 voice circuits beginning early 1980, and to be completed by 1984. A southwest program is also planned to service the greater San Francisco Bay area in the near future (Table 1-3, 1-4). A single mode, 250 megabit undersea cable system is planned to be installed by 1988[2]. Besides the above-mentioned advantages, **optical fiber systems** also enjoy **light weight, low volume; low material cost** (silica). Fiber cables also have very **high environmental endurance**. All these fringe benefits build into this new technology an intrinsic economical feature.

The main impact of optical technology to the communications industry to date has been in the realm of transmission plants, however, it is expected that light waves will be gradually entering switching, routing and processing plants to replace electronics functions. Such a process would decrease or even avoid the electrical to optical and optical to electrical conversions and thus increase the efficiency, reduce the power and cost. **The switching, routing and processing plants are the areas where integrated optics will play a significant role.**

1.1.3 Problems of Free Space Optical Systems

For over a hundreds years, free space optical systems have consisted of bulky and heavy components which required careful alignment and protection against vibration, moisture and temperature drift in the ambient air. Typical separations between components range from a few centimeters to a foot; aggregation of apparatus in a single-channel free space experimental laser repeater

is measured in square-feet and beyond. To make optical techniques more compatible with the modern technology of fiber optical communications, **integrated optics** was proposed and came into being[3-6] during the early 1970's. The essence was a miniature form of laser beam circuitry.

1.1.4 Integrated Optics

Integrated optics, as its original proposal, entails thin film technology and lithographic techniques to build on a single substrate, many minute, reliable and economical optical circuits to perform a wide variety of signal generation, modulation, processing and detection functions for optical communications systems. Although this original goal remains an attractive but somewhat ambitious target, many individual components, such as waveguide lasers, lenses, grating couplers, frequency filters, directional couplers, acousto-optical and electro-optical modulators, and single-stage switches, have already been proven feasible. The fringe benefits brought by the integrated optics research to application areas outside of communications and defense industry are apparent. It especially brought new capabilities to data transmission, signal processing and test and measurement systems. In chapters 3 and 4 we will discuss in detail some of these applications. References 8 to 12 list some of the monographs containing detailed past developments in integrated optics. Interested readers are encouraged to browse through these monographs.

1.1.5 Applications in Optical Signal Processing

Signal processing using optical methods has the potential advantages of tremendous parallelism and real-time capabilities. The high velocity of light and the parallelism result in exceptionally wide bandwidth and high throughput. The

coherent optics also have an intrinsic Fourier transform relationship between the front and rear focal planes of a lens. These advantages, however, are offset by the expense, power, bulkiness, and sensitivity to vibration, ambient temperature gradient and temperature changes as mentioned before.

Integrated optics, by using light waves propagating in a planar or strip thin film waveguide on a substrate, alleviates all these problems and results in greatly reduced size and power requirement, and increased ruggedness. However, integrated optics is not an inexpensive technology; stringent material and surface requirements, micrometer linewidth and sophisticated thin film technology are required.

Semiconductor sources and detectors, Optical data links, optical delay lines, guided wave acousto-optical (AO) laser scanners, acousto-optical tunable color filters (AOTF), **AO spectrum analyzers, high speed A/D converters, high speed switches, high rate data comparators**, ... etc., have been topics of publications in the area of integrated-optics research. The current definition of integrated optics covers all explorations of guided-wave techniques used to construct optical devices and systems with better reliability, better mechanical and thermal stability, lower power consumption and lower drive voltages.

1.1.6 Relevance to Tektronix

Tektronix, with our recent involvement in communications industry, computer terminals and graphics systems, our historical market stake in high speed test and measurement instruments, and our new thrust in video processing, it is important that we begin to explore along the learning curve in this high growth (70% compounded annual growth) new technology area. The benefit of this new technology could bring us leapfrogging advancements in many lines of our

products. The tools involved, such as thin-film, high resolution lithographic and GaAs techniques, high speed photodetectors, $LiNbO_3$ material and processing expertise, and surface acoustic wave technology, either exist in-house or are important to other vital technology areas needed at Tektronix.

The present GaAs research efforts at Tek provide us a base on developing integrated optical transmitter and receiver for high rate (> 200 MHz) serial data communication. Utilizing the Surface Acoustic Wave technology we have in house in combination with integrated optics, we could provide significant high technology barriers to our hard copy systems and T.V. measurement instruments. Optical delay lines, high speed sampling using integrated-optical gates and optical A/D converters will bring new capabilities to our high speed test and measurement instruments. Optical video routing switcher (Chapter 3, 5) as well as the integrated optical transmitter, receiver and repeater (Chapter 5.4) could give us a strong thrust into the video processing business area. Integrated-optical modulators could help us realize high speed programmable circuit testing system for boards and ICs (Chapter 4.6).

1.2 Dielectric Optical Waveguides

The theory of dielectric waveguides has been described in detail by D. Marcuse[13,14], N.S. Karpary & J.J. Burke[15], H. Kogelnic[16], P.K. Tien[17]. In this and the remaining sections of this chapter, fundamental physical concepts, terminologies, and application oriented characteristics of waveguides are introduced. Ray optics or wave theory will be adopted wherever suitable for simplicity and clarity. For detailed mathematical treatments, readers are encouraged to explore the above mentioned references.

1.2.1 Types of Dielectric Waveguides

Optical fibers are used for signal and data transmission between apparatuses, systems, machines, plants, sites and over long distances. In **integrated optical** devices, thin-film dielectric waveguides are used to confine the light in very small cross-sections over the length of the device (relatively long compared to the cross-section) to minimize loss and dispersion. The optical fibers guide light waves within the core, surrounded by a cladding layer with a lower refractive index. The planar waveguides (Fig. 1-1) confine light to a two dimensional thin-film slab. The strip guides (Fig. 1-2) are lithographically processed and confine light to a prepatterned, one-dimensional path. Whether planar, strip, or fiber, the light guiding uses the principle of total internal reflection. In this and the following sections we will focus mainly on the integrated optical thin film guides.

1.2.2 Total Internal Reflection

Total internal reflection can be realized when the incident ray angle ϑ exceeds critical angle ϑ_c, if the refractive index of the waveguide n_f is larger than both the refractive index of the substrate n_s, and cover material n_c. The critical angle ϑ_c is given by

$$\begin{aligned} \sin \vartheta_{cs} &= n_s / n_f \\ \sin \vartheta_{cc} &= n_c / n_f \\ \vartheta_c &= \max (\vartheta_{cc}, \vartheta_{cs}) \\ n_f &> n_c, n_s \end{aligned} \qquad (1.1)$$

The refractive index difference between the waveguide film and the substrate is typically in the range of 10^{-3} to 10^{-2}:

$$\Delta n = n_f - n_s = 0.01 \text{ to } 0.001$$

1.2.3 Thickness, linewidth and loss

The typical dimensions of a single mode (Section 1.3) strip guide are heights of 0.5 μm, and width of 2 to 3 μm, length of submillimeters to centimeters.

The state-of-the-art loss on thin-film waveguides is approximately equal to or less than 1dB/cm.

1.2.4 Material, Fabrication, and Integration

A number of materials can be used as waveguide substrates, depending on the application, modulation technique, and the transparency of the material at interested wavelength region.

The waveguide films are usually formed by sputtering, thermal deposition, thermal diffusion, chemical vapor deposition or molecular beam epitaxy of a higher refractive index material over the substrate surface. For example: the rf sputtering of higher index glass on a lower index glass substrate has been used to fabricate directional couplers and waveguide filters; Ti or Nb in-diffusion in ferroelectric crystals, such as $LiNbO_3$ and $LiTaO_3$ is used to fabricate waveguides for electro-optical modulators. GaAs is of particular interest for monolithic integration because of its capability to form waveguide lasers and photodetectors. In the case of GaAs, Al dopant is used to lower the refractive index of the substrate and the cover material. Crystalline layer of $Ga_{1-x}\ Al_x\ As$ is grown on top of a GaAs substrate by liquid phase epitaxy. A pure GaAs layer is then grown on top of the $Ga_{1-x}\ Al_x\ As$ layer, which in turn is covered by another layer of $Ga_{1-x}\ Al_x\ As$ layer.

Channel waveguides are patterned using high definition lithographic techniques common to that used for semiconductor processing.

Monofunctional integration in integrated optical devices, such as an array of laser sources or detectors is easier to fabricate from material's point of view, since the performance can be optimized with one base material. However, in most applications multifunctional integration will ultimately be needed.

The optimal material for components performing different functions in an integrated optical system are usually drastically different. For example, The III-V semiconductor crystal is used to construct semiconductor lasers and photo diodes. However, the electro-optical coefficient of GaAs is 30 times smaller than that of $LiNbO_3$, and its acousto-optical figure of merit* is 10 times smaller than that of α-HgS film. $LiNbO_3$ has the highest piezoelectric and electrooptic coefficient and lowest acoustic loss, however, its acoustooptical figure of merit is only 7, compared to 104 of GaAs and 960 of α-HgS. This means that GaAs would be the choice material for detectors and/or sources; $LiNbO_3$ is the optimal material for EO modulators, switches, and acoustic transducer, and α-HgS is the better AO material.

Hybrid integration is frequently adapted approach to optimize the multifunctional integration, in which the source and detector are usually prism coupled, or grating coupled, or butt-jointed to the modulator. Some optical loss is suffered in the coupling process (see Chapter 2). It is possible that a technique to crystalize onto a common substrate, layers of thin-film materials tailored to optimize individual components on a common substrate would be developed in the future. This would then be an ultimate solution for true optimized monolithic, multifunctional integration of guided-wave optical systems. Molecular beam epitaxy, chemical vapor deposition, or laser processing are possible tools to achieve such crystalization processes. Further discussion on the fabrication of Ti-diffused $LiNbO_3$ waveguides is given in Appendix A.

* Figure of merit is a direct indication of acousto-optic coupling efficiency (see Chapter 3).

1.3 Modes of Dielectric Waveguides

The "Mode" in optics is a very confusing term. We hear TE (Transverse Electric) and TM (Transverse Magnetic) modes frequently. We have single and multi-mode fibers and lasers. In thin-film waveguides we have radiation, guided, substrate and evanescent modes. What do all these "modes" mean? What are the implications?

1.3.1 Modes

Any electromagnetic wave can generally be written as a wavefunction ψ_k (**r**,t), where:

$$\psi_{\mathbf{k}}(\mathbf{r},t) = \psi_o \; e^{i(\omega t - \mathbf{k}\cdot\mathbf{r})}$$
$$k^2 = \omega^2 \mu \varepsilon \tag{1.2}$$

At a constant time t, be $t = 0$

$$\psi_{\mathbf{k}}(\mathbf{r}) = \psi_o \; e^{-i\mathbf{k}\cdot\mathbf{r}} \tag{1.3}$$
$$\textit{where} \quad \mathbf{k} = k_x\mathbf{x} + k_y\mathbf{y} + k_z\mathbf{z}$$
$$\text{and} \quad k_x^2 + k_y^2 + k_z^2 = k^2 = \left(\frac{2\pi}{\lambda}\right)^2 = \left(\frac{2\pi\nu n}{c}\right)^2.$$

The energy of the wave E_ν is related to the frequency of the wave ν by Planck's constant $E_\nu = h\nu$. The wave vector **k** denotes a "mode". The direction of **k** is the propagation direction of the wave and the wave number $|k|$ is associated with the frequency and energy of the wave. For each **k**, either different in direction, or in magnitude, there is a mode $\psi_{\mathbf{k}}$. Physical constraints or boundary conditions of a system usually give sets of quantized discrete values to the solutions of (k_x, k_y, k_z) and $|k|$ (Figure 1-3).

1.3.2 TE and TM Modes

Let us define the coordinates **x**, **y**, **z** such that **x** is perpendicular to the interface planes, **y** is parallel to the interface planes, and **z** is the principal guided propagation direction. There are two ways of defining **Transverse Electric** (TE) and **Transverse Magnetic** (TM) modes. In ray theory, TE modes indicate those waves having electric field perpendicular to the incident plane, formed by the incident ray and the normal to the interface plane; i.e., $\mathbf{E} = \mathbf{E_y}$, $E_x = E_z = H_y = 0$. TM modes are those waves having a magnetic field perpendicular to the incident plane; i.e. $\mathbf{H} = \mathbf{H_y}$, $H_x = H_z = E_y = 0$.

In wave theory, TE modes indicate those waves which have zero longitudinal electric field, $E_z = 0$. TM modes indicate those waves which have zero longitudinal magnetic field $H_z = 0$. However from Maxwell's equations, we can conclude that for TE modes $E_z = E_x = H_y = 0$, for TM modes $H_z = H_x = E_y = 0$, identical with the ray theory definitions. **In a cavity or waveguide, TE and TM modes can coexist. However, they can be separated by means of polarizers at either the input or the output port.**

1.3.3 Modes of the planar slab guide

The three sets of modes of an asymmetric slab waveguide with $n_f > n_s > n_c$ are classified by the incident angle ϑ (Figure 1-4).

1. guided modes:
   The light waves satisfy the total internal relection condition:
   $\vartheta > \vartheta_{cs}, \vartheta_{cc}$,
   and propagate within the waveguide, where ϑ_{cs} and ϑ_{cc} are the critical angles of the film-substrate and film-cover interfaces.

2. radiation modes:

   The light waves is incident on the substrate with a small angle ϑ.

   $\vartheta < \vartheta_{cs}, \vartheta_{cc}$.

   and radiate back into the free space.

3. substrate radiation modes:

   The light waves incident angle is between the critical angles ϑ_{cs} and ϑ_{cc}:

   $\vartheta_{cc} < \vartheta < \vartheta_{cs}$, or $\vartheta_{cs} < \vartheta < \vartheta_{cc}$.

   In this case the light waves incident from the substrate are reflected back from the guide-cover (substrate) interface and radiate into the substrate.

1.3.4 Guided Modes

The constructive interference (or self-consistent) condition imposed on a guided wave results in a discrete set of allowable incident angles ϑ_m for a given $|k|$ (or frequency ν):

$$2k\, n_f\, h\, \cos\vartheta - 2\varphi_s - 2\varphi_c = 2m\pi \tag{1.4}$$

where k is the wave number, h is the height of the waveguide, $-2\varphi_s$ and $-2\varphi_c$ are the phase shifts introduced at the waveguide boundaries.

This set of constructively interfering modes ψ_m are called "propagation modes" or "guided modes". The number of propagation modes a waveguide can support for a given ν depends on the thickness of the waveguide. **A thicker waveguide can support more modes.** When a waveguide's thickness is such that it can support only one mode, it is called a "single mode" waveguide. Otherwise, it is a multimode waveguide.

Simplistically speaking, the different waveguide modes are the different zig-zag waves (Figure 1-5) traveling at different ray angles. For example, a 0.78 μm thick Ta_2O_5 film 0.78 μm thick deposited on a glass substrate supports four waveguide modes. **Figure 1-6 shows these four waveguide modes for TE polarization.** In the first order mode (m=0), the rays nearly graze the surface of the

film. As the order of the mode, m increases, the ray angle becomes correspondingly smaller. For the last supported mode, the ray angle approaches the critical angle ϑ_c. The field distribution associated with each mode are shown at the right side of the figure. We see that the order of the mode is equal to the number of nodes in the field distribution. In channel waveguides, the propagating mode in a waveguide could be coupled into adjacent guides, if the spacing and interaction length of the guides are appropriate. Optical directional couplers are often fabricated in this manner.

1.3.5 Modes in Fibers and Lasers

Fibers

The physical concepts of modes in Section 1.3 are also generally applicable to waveguide lasers and optical fibers. The mathematical treatment for optical fibers is simpler due to the cylindrical symmetry. A typical stepped index multimode fiber with 40 μm to 100 μm diameter can support hundreds or even thousands of modes. The fractional bandwidth dependence on propagation loss is negligible. The noise caused by modal dispersion and the pulse dispersion, however, makes stepped index multi-mode fiber unsuitable for long distance or very high data rate (>100MHz) applications.

Single mode optical fibers are realized by decreasing the core diameter. A typical stepped index single mode optical fiber has a core diameter between 1.5 μm to 8 μm. Freedom from modal noise and the much smaller pulse dispersion (broadening) in single mode fibers make them suitable for very high data rate (>100MHz) and very long distance applications. The pulse broadening in single mode fibers however is proportional to the fractional spectral bandwidth of the light source. A narrower spectral width of the light source is thus desirable

when optimization in data rate is an objective.

Graded index optical fibers employ a radially parabolic varying core index to compensate the group velocity difference between modes and thus minimize pulse broadening. By gradually lowering the refractive index in the core toward cladding, we speed up the higher order modes which travels more distance in the lower refractive index region and thus compensate the delay caused by the additional light path traveled compared to the lower order modes (see Section 1.5.2). Theoretically, a factor of 1000 improvement over stepped-index multimode fibers is possible. However, due to the difficulties in controlling the index profile, improvement of a factor of 100 is realistic. The propagation and pulse dispersion (see Section 1.5.2) of a light pulse in the three types of fibers are illustrated in Figure 1-7.

Lasers

The hole-electron recombination region of a semi-conductor laser is in fact a rectangular thin-slab waveguide. We can consider this waveguide as a resonance cavity in which the lightwave is confined (Fig. 1-8). The cavity length L, along z-axis has two mirrored (or cleaved) end faces.

The cavity modes of a laser are separated into 2 sets, the TE ($E_z=0$) and the TM ($H_z=0$) modes. The modes of each set are characterized by three mode numbers (q, s, m), the quantum numbers of the (x, y, z) axes as described in subsection 1.3.2. The three mode numbers represent the number of "half-sinusoidal" variations (Figure 1-3) of the field along the three major axes of the cavity. The **longitudinal modes** are denoted by m, at fixed q and s. m determines the principal structure in the frequency spectrum. The **transverse** (direction perpendicular to the junction planes) **modes** are denoted by q, at fixed s and m, and depend on the dielectric variation along the axis perpendicu-

lar to the junction plane in the recombination region. The transverse modes are important to the spatial and threshold current characteristics of the laser. The lateral modes in the plane of the junction are denoted by s. Lateral modes are determined by diode width and the side wall preparation. The wavelength separation of lateral modes is usually only a fraction of an angstrom compared to a few Å wavelength separation of the longitudinal modes. It is important in selecting a single mode laser to specify single longitudinal mode for spectrum purity and single transverse mode for spatial characteristics.

1.4 Waveguide Losses

1.4.1 Scattering and Volume Losses

The optical power loss in a dielectric waveguide is caused by volume absorption and interface surface scattering (Rayleigh loss). The volume absorption depends on the material property and can be considered as a constant for all waveguide modes. The scattering loss occurs due to the fact that the interface surfaces are not perfectly smooth, and edge roughness is introduced during processing. For the typical thickness of a thin film waveguide, it would take 1000 zig-zags for a guided mode to travel 1 cm along the waveguide. If the interface surfaces are not perfectly smooth, each bounce at the interface will suffer some scattering loss. Thus we can understand that the **scattering loss increases rapidly with the increasing order of the guided mode**[19], because the higher the order of the mode, the more bounces it takes for the wave to travel through the waveguide.

Figure 1-9 shows the measured sum of the volume and surface scattering losses for the four waveguide modes in a Ta_2O_5 film. The volume loss is obtained

by extending the measured curve in Figure 1-10 to $\beta/k = n_f$. That is, ϑ=90°, a straight through wave, we can see that thin-film waveguides are practically single mode devices. To minimize the loss of optical power, it is preferred to use only the first order mode, m=0, even if the waveguide can support more than one mode.

1.4.2 Bending Loss

Irregularities in the waveguide boundaries can couple energy from one propagating mode to another propagating mode or to radiation modes. The irregularity can be unintentional due to processing imperfections, or intentional, such as bends in an integrated strip guide circuit, or a periodic grating. The radiation loss due to bends will impose a lower limit on the size and extent of integration. The intentional periodic irregularities, for example, a grating, may be used in our advantage, such as coupling lightwaves in-and-out of the waveguides.

Marcuse[20,21], Marcatili[22], and Goell[23] had vigorously treated the theory of mode coupling and bending loss. I will introduce the results on bending loss in this subsection.

The bending loss is a very fast function of the radius of curvature:
Define rate of power loss α:

$$\alpha = \frac{1}{2P_0}\frac{dP}{dz} \qquad \textit{where z is the propagation axis}$$

and P_0 is the initial power at z=0. Using wave velocity approach[24], one obtains the relationship between α and the bending radius R:

$$\alpha = C_1 \exp(-C_2 R). \tag{1.8}$$

Figure 1-10 shows radiation loss versus bend radius for a waveguide with n_f = 1.5, n_s = n_c = 1.485 and width 1.04 μm as calculated by Goell[23]. Bending

loss for a 90° bend versus radius of curvature is also calculated by Goell using Marcatili's Modal Analysis. The result is plotted in Figure 1-11 for various Δn values. For a given bend radius, **one can reduce the bending loss by increasing** Δn, the difference of the refractive index of the guide n_1 and that of the surrounding media n_3 next to the guide along the bend axis (Fig. 11). A 1% radiation attenuation (0.087dB) in a guide length equal to bending curvature R can be achieved by the following values[18]:

$\frac{1}{n_1}(n_1 - n_3)$	a / λ	R / λ
0.1	0.745	30
0.01	2.36	1060
0.001	7.45	37000

1.4.3 Coupling Loss

Whether coupling from fiber to fiber or integrated optical waveguide to fiber, misalignment is the most serious cause of loss. A >70% coupling efficiency is achievable for both cases when alignment is handled carefully. A >90% coupling can be achieved in fiber to fiber connection by V-groove alignment. Theoretically, several methods allow the source to film guide coupling efficiency to be near 100%. However, in practice, an 80% efficiency was experimentally measured. Details in coupling methods will be discussed in Chapter 2.

1.5 Dispersion

Two types of dispersion need to be considered. One is beam dispersion (spreading) in spatial domain, another is pulse dispersion (broadening) in time domain.

1.5.1 Beam Spreading

From the dispersion equation (1.4) in section 1.3, we obtain the dispersion equation for fundamental mode:

$$\frac{2\pi n_f h}{\lambda} Cos\ \vartheta = \varphi_s(\vartheta) + \varphi_c(\vartheta) \qquad (1.9)$$

By plotting both sides of the equation as functions of ray angle ϑ, we can obtain the solution ϑ_0 at the cross-section of the two curves. Figure 1-12 shows the curves for both symmetric guides ($n_s = n_c$) and asymmetric guides ($n_s > n_c$). We see from Figure 1-12 that if our light source contains a spectrum spread $\lambda = \lambda \rightarrow \lambda + \Delta\lambda$, the ray angle of the fundamental mode would also spread $\vartheta_0 = \vartheta_0 \rightarrow \vartheta_0 + \Delta\vartheta_0$. A 10% fractional bandwidth of the light source will result to approximately 5° spread in ray angle ϑ_0.

1.5.2 Pulse Broadening

The effect of pulse broadening is to pose an upper limit on the bandwidth (data rate) of the system. Pulse broadening in dielectric waveguides has been mathematically treated for cylindrical waveguides[25-27]. Since the result measures in nanosecond per kilometer units, it is more of a concern for optical fibers than thin-film waveguides which typically guide light in millimeter or centimeter lengths. In a multi-mode fiber, pulse broadening is primarily caused by the group velocity difference of the different excited modes. The higher order modes travel slower and thus arrive late. The lower order modes travel fast and arrive early. The time difference per kilometer between the fastest and the slowest modes is approximately proportional to the numerical aperture of the fiber. **For a typical stepped index multimode fiber, the pulse dispersion is in the order 50ns/km.**

Graded index multi-mode fiber uses a radial parabolic varying core index to compensate the group velocity differences between higher order and lower order modes. Theoretically, 3 to 4 orders of magnitude improvement can be achieved. However, the control of the radial index profile is difficult. A practical improvement of a factor of 100 was obtained. Figure 1-7 shows conceptually the dispersion of a pulse through the three types of optical fibers.

The pulse broadening in single mode fibers is caused by chromatic effect; i.e., the combination of material and waveguide dispersion due to the spectral width of the light source and the modulating signal. The pulse broadening per unit length is approximately

$$\Delta t/L \approx \frac{1}{V_g} \approx \frac{\lambda^2}{c^2} \frac{\Delta \lambda}{\lambda} \frac{d^2 n}{d \lambda^2} \tag{1.10}$$

where V_g is the group velocity, c is the speed of light in vacuum and λ, the wavelength of the light source, $\frac{\Delta \lambda}{\lambda}$ is the fractional spectral bandwidth of the light source. A 20ps/km pulse spread is typical in single mode fibers using a laser source. A LED source with single mode fiber typically results to 100ps/km spread. The pulse dispersion and transmission bandwidth versus source spectral width for several types of optical fibers[28] are illustrated in Figure 1-13.

Table 1-1

BELL SYSTEM LIGHTWAVE PROGRAM
(Installed)

Location	*Cut-Over*	*Route Miles*	*Fiber-Km*	*Digital Level*
Atlanta, GA	1/76	0.4	94	3
Chicago, IL	5/77	1.5	18	3
Orlando, FL	3/79	0.6	15	1
Phoenix, AZ	10/79	1.7	18	3
Sacramento, CA	10/79	2.7	155	2
Trumbull, CT	11/79	4.0	156	3
Lake Placid, NY	2/80	2.5	50	2
New York, NY	5/80	2.3	90	2
Atlanta, GA	9/80	6.3	400	3
Colorado Springs, CO	9/80	18.3	240	3
San Francisco, CA	10/80	3.6	270	3
Chester, NJ	2/81	3.0	208	2
Pittsburgh, PA	4/81	40.6	2,800	3

Table 1-2

System	*Cut-Over*	*Fiber-Km*	*Use*	*Bit Rate*	*Remarks*
Chicago, IL	5/77	4	F	DS-3	Experimental
		12	T		
Orlando, FL	2/79	15	F	DS-1	General Trade
Phoenix, AZ	8/79	18	F	DS-3	General Trade
Sacramento, CA		155	T	DS-2	Field Trial
Trumbull, CT		156	F	DS-3	Pre-Standard FT3
Lake Placid, NY	2/80	38	F	DS-2	Custom
Bernal Hts., CA	10/80	270	T	DS-3	Pre-Standard FT3
Smyrna, GA	12/80	400	T	DS-3	Standard FT3
Pittsburgh, PA	2/81	2,800	T	Ds-3	Standard FT3
San Francisco, CA	4/81	2,000	T	DS-3	Standard FT3
White Plains, NY	6/81	1,300	T	DS-3	Standard FT3

Table 1-3

BELL SYSTEM LIGHTWAVE PROGRAM
(Planned - 1981)

Location	*Cut-Over*	*Route Miles*	*Fiber-Km*	*Digital Level*
White Plains, NY	6/81	27.6	3,200	3
San Francisco, CA	6/81	8.8	2,000	3
Los Angeles, CA	6/81	6.7	1,625	3
Greenville, TX	6/81	2.1	41	3C
Lindenhurst, NY	6/81	2.9	224	3
Philadelphia, PA	7/81	16.8	3,100	3
Willowcrest, IL	8/81	3.9	226	3
San Francisco, CA	8/81	14.0	1,670	3
Orlando, FL	11/81	9.5	1,136	3
Gardena, CA	11/81	14.5	1,670	3
Sherman Oaks, CA	11/81	10.0	1,152	3
Melville, NY	11/81	3.9	377	3
Newark, NJ	12/81	26.1	3,012	3

Table 1-4

BELL SYSTEM LIGHTWAVE PROGRAM
(Planned Long Haul - 1982-1984)

Location	*Route Miles*	*Fiber-Km*	*Digital Level*
West Coast			
Oakland-Stockton	82	12,000	3C
Stockton-Sacramento	54	5,200	3C
Hayward-San Jose	29	1,100	3C
Northeast Corridor			
Washington-New York	377	50,000	3C
New York-Boston	244	30,000	3C

Figure 1-1 Thin film slab waveguide:

Sideview of a slab waveguide showing propagation of the zig-zag waves corresponding to a guided mode.

Figure 1-2 Channel (strip) waveguides:

Cross-sections of four types of strip waveguides.

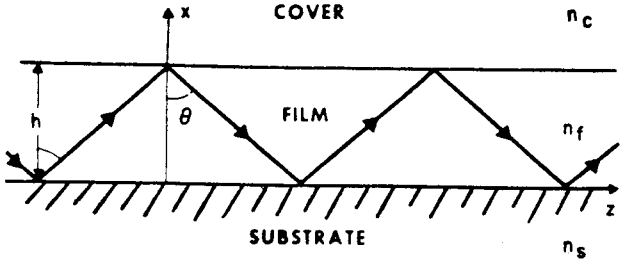

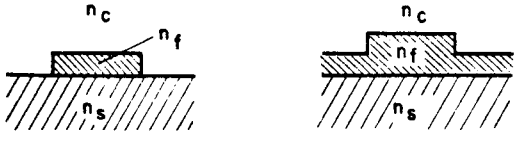

a.) raised strip

c.) ridge guide

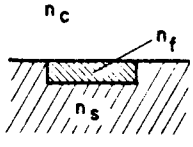

b.) embedded strip

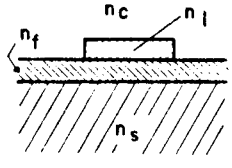

d.) strip-loaded guide

Figure 1-3 The modes of a cavity ψ_q's for fixed s and m:

The order of the modes q, s, m corresponds to the number of "half-sinusoidal" variations of $\vec{\psi_k}$ along the three major axes of the cavity.

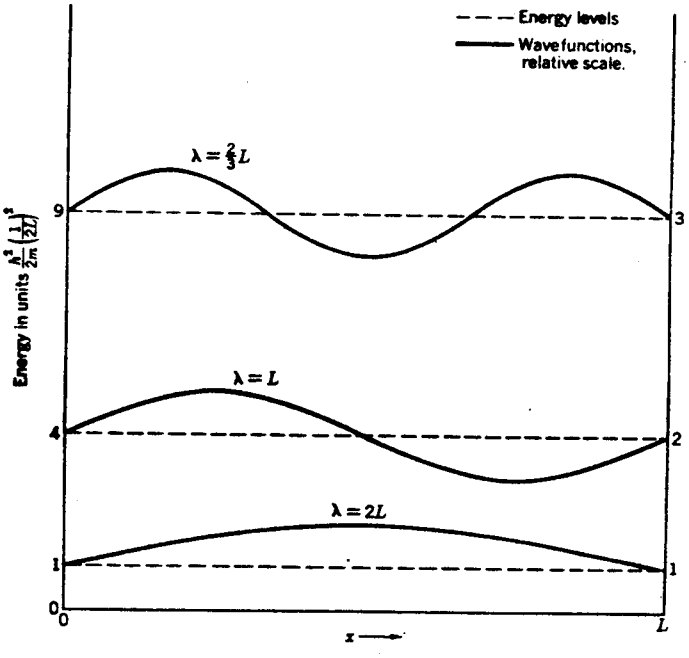
Energy levels
Wave functions, relative scale.
λ = 2/3 L
λ = L
λ = 2L
9
4
1
0
3
2
1
0
L
x
Energy in units A²/2m (1/2L)²

Figure 1-4 Waveguide modes:

Ray-picture of (a) radiation modes, (b) substrate radiation modes, (c) guided modes in a slab waveguide.

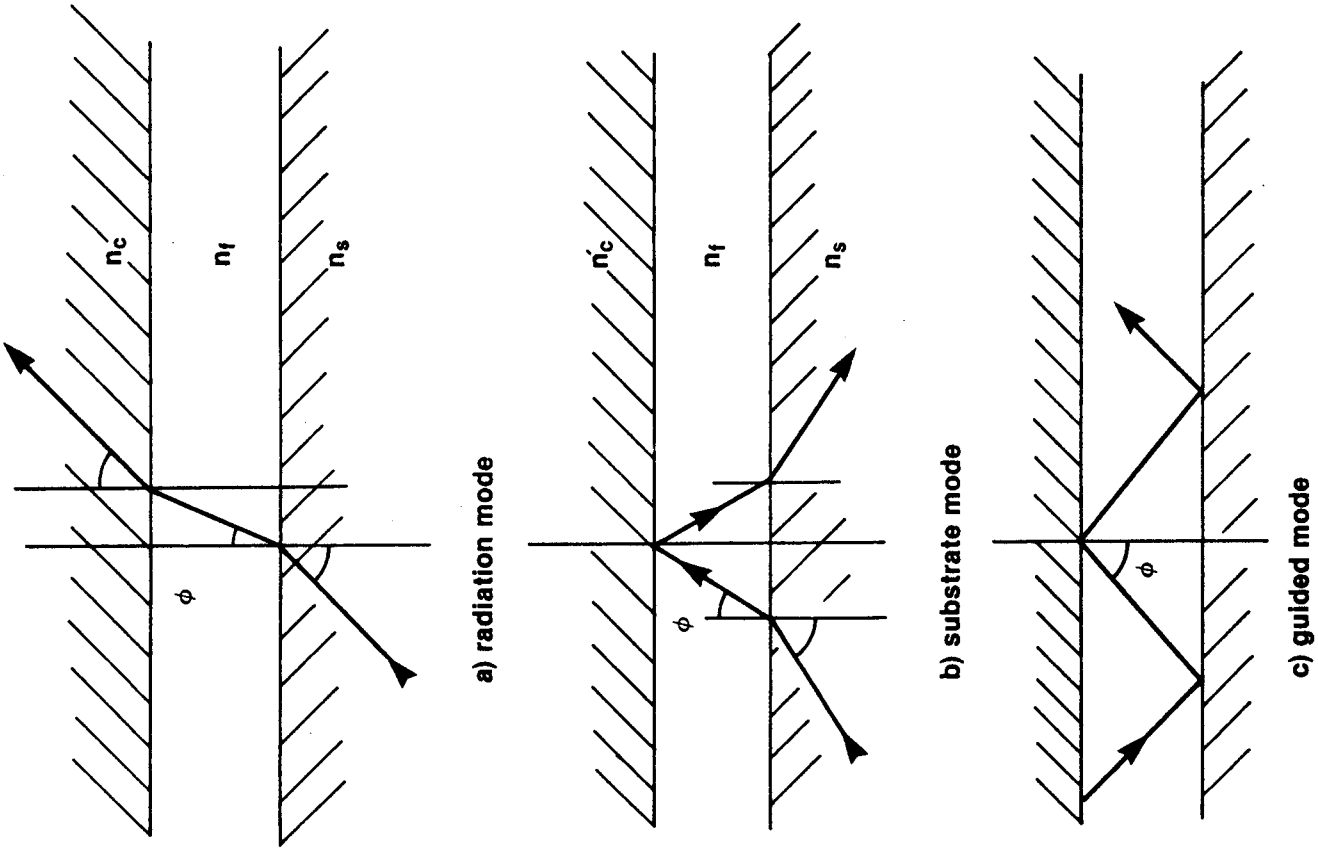
n_c
n_f
n_s
ϕ
a) radiation mode
n_c
n_f
n_s
ϕ
b) substrate mode
ϕ
c) guided mode

Figure 1-5 Zig-zag waves:

An infinitely wide plane wave is folded back and forth into itself between the upper and lower waveguide interfaces.

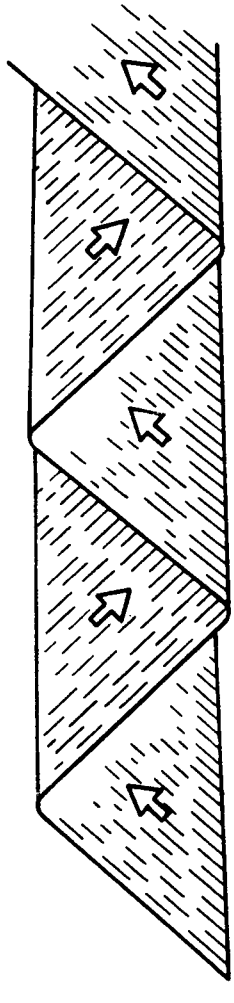

Figure 1-6 The four guided modes of a Ta_2O_5 film waveguide:

A Ta_2O_5 film of 0.776 microns thick propagates four waveguide modes. The electric field distributions and the zig-zag waves associated with these waveguide modes are shown at the right and the left of the figure, respectively.

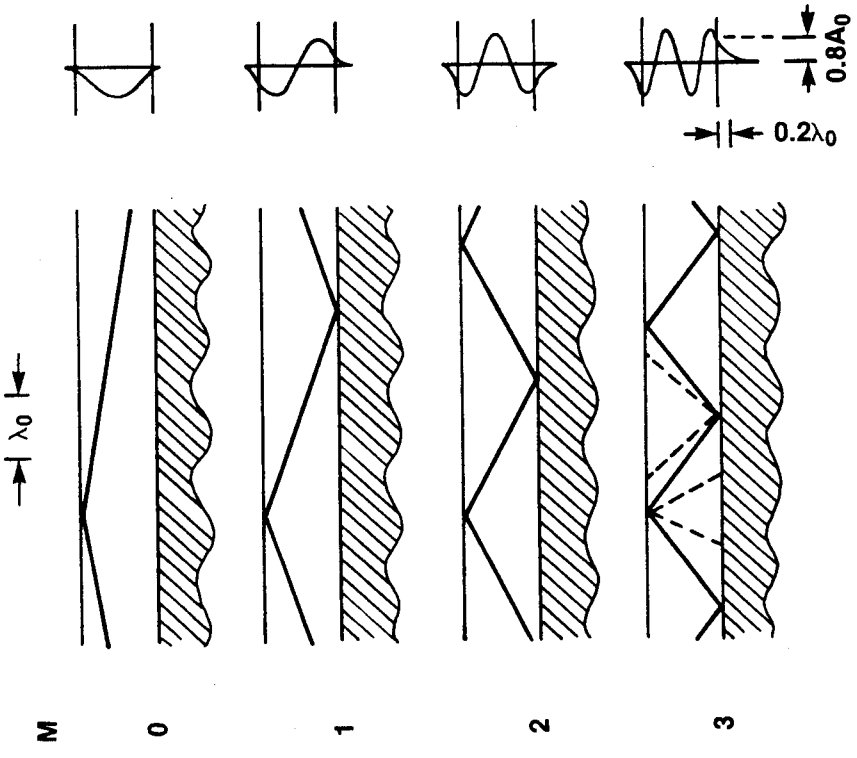
0.8A0
0.2λ0
λ0
M
0
1
2
3

Figure 1-7 Dispersion in optical fibers:

The time-dispersion of optical pulses propagating through the three types of optical fibers.

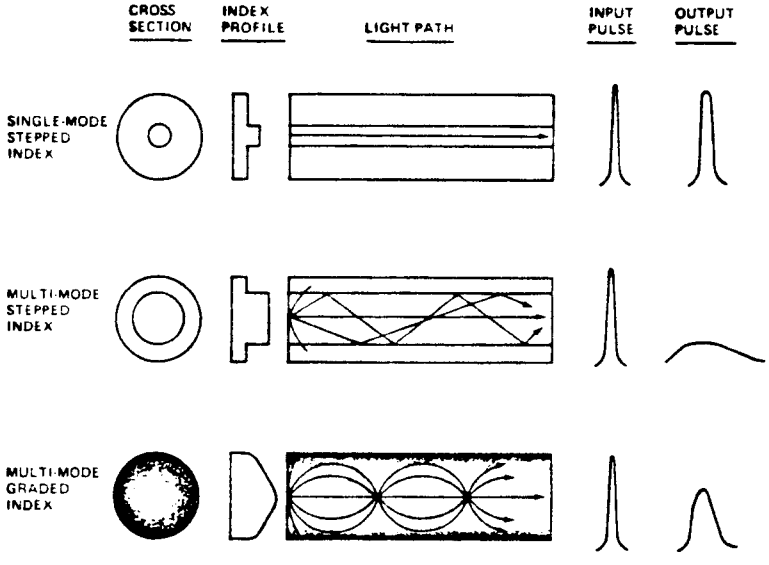
CROSS SECTION
INDEX PROFILE
LIGHT PATH
INPUT PULSE
OUTPUT PULSE
SINGLE-MODE STEPPED INDEX
MULTI-MODE STEPPED INDEX
MULTI-MODE GRADED INDEX

Figure 1-8 Configuration of semiconductor junction laser:
(a) Broad area laser,
(b) strip-contact laser,
(c) waveguide model,
(d) radiation from the end facet of an injection laser.

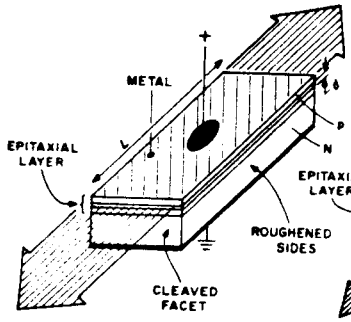

BROAD-AREA LASER

(a)

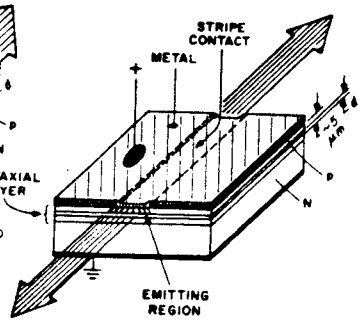

STRIPE-CONTACT LASER

(b)

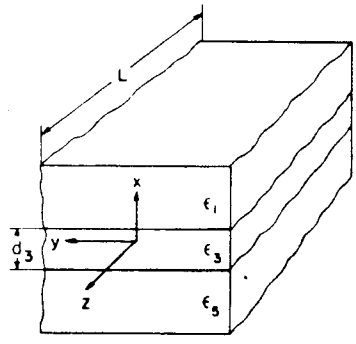

$\epsilon_3 > \epsilon_1, \epsilon_5$

(c)

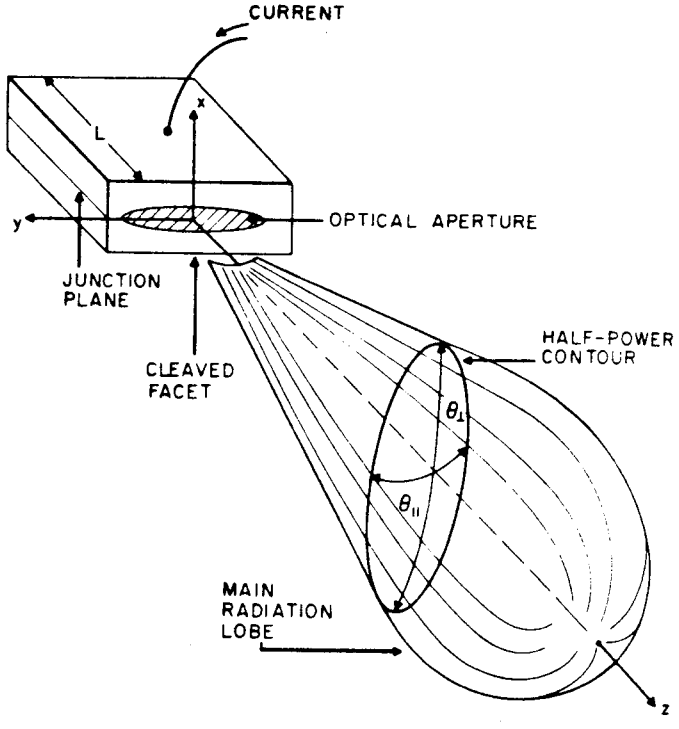

(d)

Figure 1-9 Loss versus waveguide *modes*:[15]

The horizontal axis is the β/k values of the waveguide modes, where

$$\beta_m = kn_f \sin \vartheta_m$$

is the propagation constant. A HeNe laser of wavelength 0.6328 μm was used in the measurement. The volume absorption loss is extrapolated as the loss of the light wave energy at ϑ=90°, i.e., when the light wave propagates straight through waveguide without bounces.

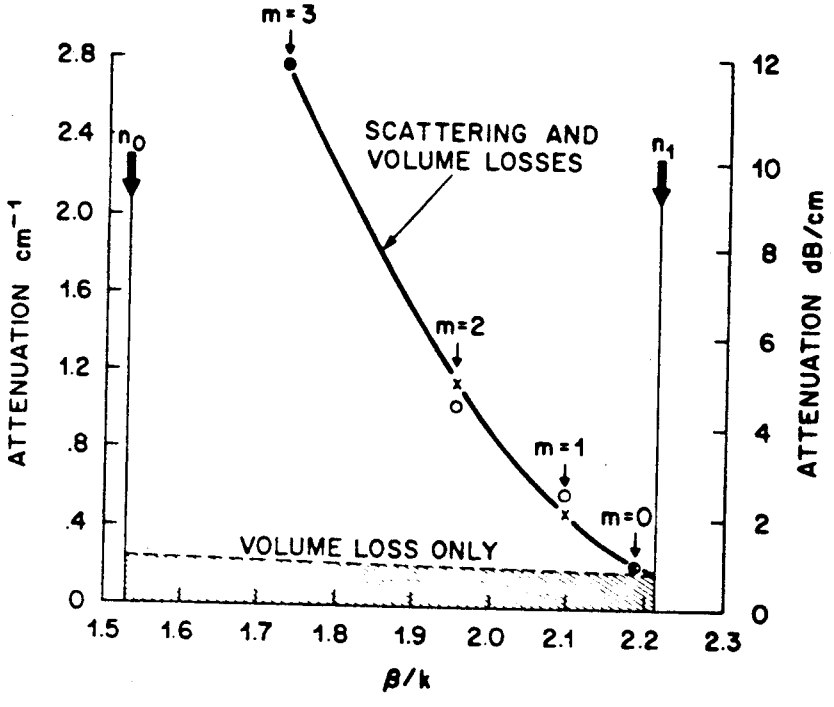
m=3
SCATTERING AND
VOLUME LOSSES
n_0
n_1
m=2
m=1
m=0
VOLUME LOSS ONLY
ATTENUATION cm^{-1}
ATTENUATION dB/cm
2.8
2.4
2.0
1.6
1.2
.8
.4
0
12
10
8
6
4
2
0
1.5
1.6
1.7
1.8
1.9
2.0
2.1
2.2
2.3
β/k

Figure 1-10 Radiation loss versus bend radius of strip waveguides.

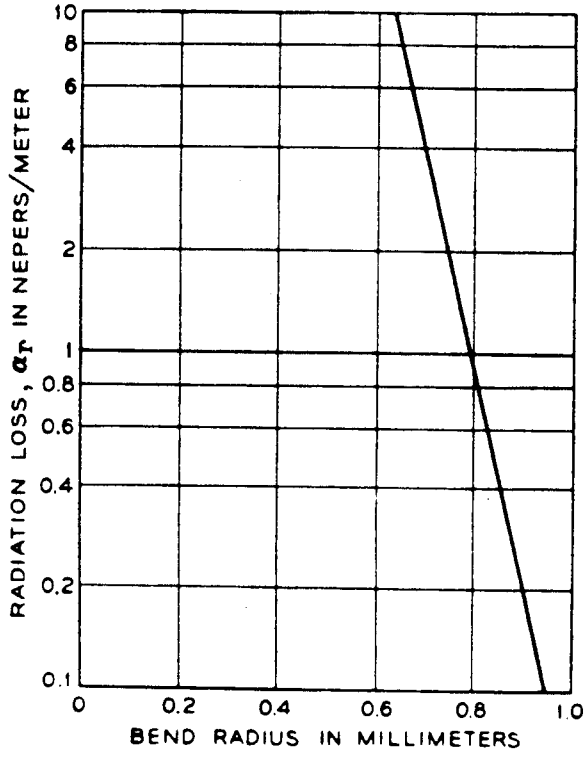
RADIATION LOSS, α_r IN NEPERS/METER
10
8
6
4
2
1
0.8
0.6
0.4
0.2
0.1
0
0.2
0.4
0.6
0.8
1.0
BEND RADIUS IN MILLIMETERS

Figure 1-11 Bend loss for various Δn:

Bend loss for a 90° bend versus radius of curvature of the bend for various Δ.

$$A = \lambda/2 \, (n_1^2 - n_3^2)$$

$$\Delta = n_1 - n_c$$

$$(1 - k_y/k_z) \approx 1$$

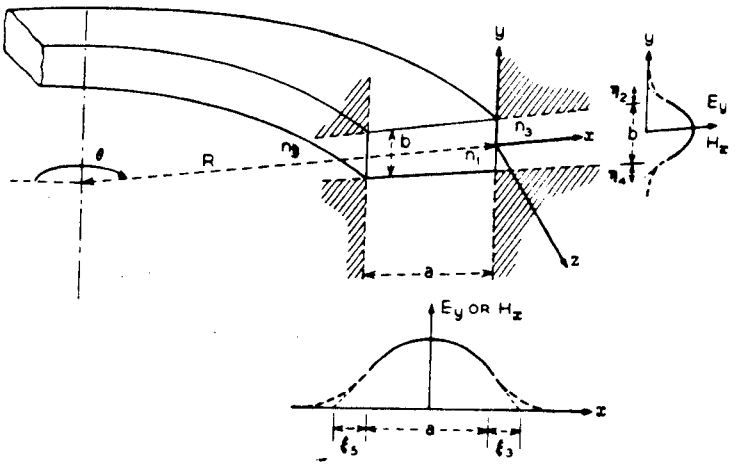
y
x
z
θ
R
b
a
n_3
n_1
n_2
E_y
H_x
E_y OR H_x
ξ_5
ξ_3

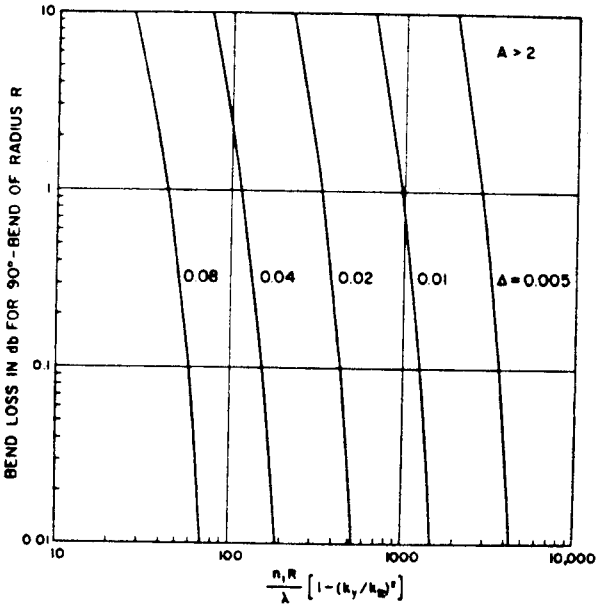
BEND LOSS IN db FOR 90°-BEND OF RADIUS R
10
1
0.1
0.01
10
100
1000
10,000
A > 2
0.08
0.04
0.02
0.01
Δ = 0.005
$\frac{n_1 R}{\lambda}\left[1-(k_y/k_0)^2\right]$

Figure 1-12 Dispersion caused by spectral spread:

Graphical solution of dispersion equation for the fundamental modes (m=0) of a slab waveguide. The curve in between the dotted curves is the values of $kn_f h\sin\vartheta$ as a function of ϑ. The solid line is the Goos-Haenchen shift of a symmetric waveguide $\vartheta_c = \vartheta_2$, the dashed line is that of an unsymmetric guide ($\vartheta_c \neq \vartheta_s$).

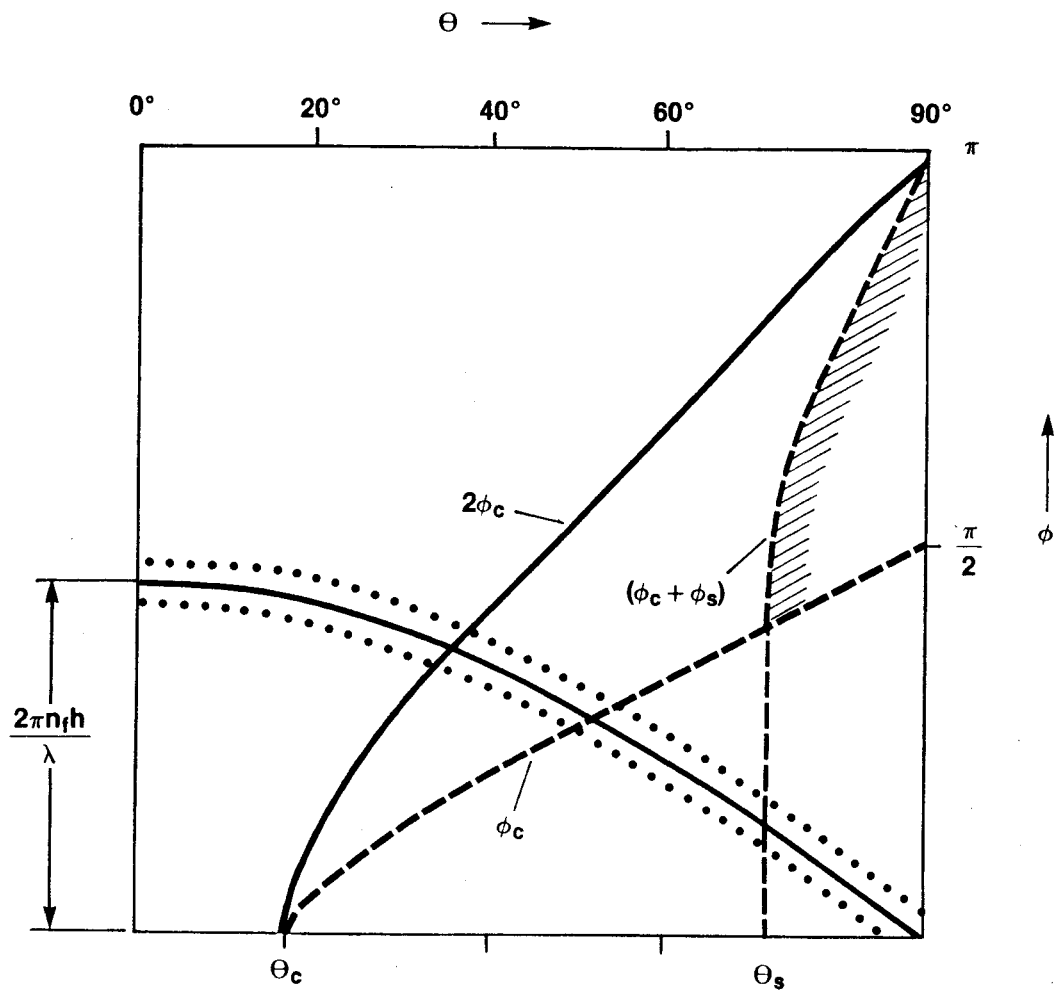
Θ
0°
20°
40°
60°
90°
π
2φc
(φc + φs)
π/2
φ
2πnfh/λ
φc
Θc
Θs

Figure 1-13 Pulse dispersion:

Pulse spreading and transmission bandwidth (data rate-fiber length product) versus source spectral width for: multimode fiber of step-index profile, $GeO_2 \cdot B_2O_3 \cdot SiO_2$ glass, $\Delta = 0.01$; multimode graded-index fiber, $GeO_2 \cdot B_2O_3 \cdot SiO_2$ glass, $\Delta = 0.01$, bandwidth improvement factor = 100; and single-mode fiber, $B_2O_3 \cdot SiO_2$ glass, $\Delta = 0.001$. The pulse spreading and spectral width are twice their respective root-mean-square values. The dashed line corresponds to the fundamental low limit to pulse spreading in silica-based fibers (after Li)[28].

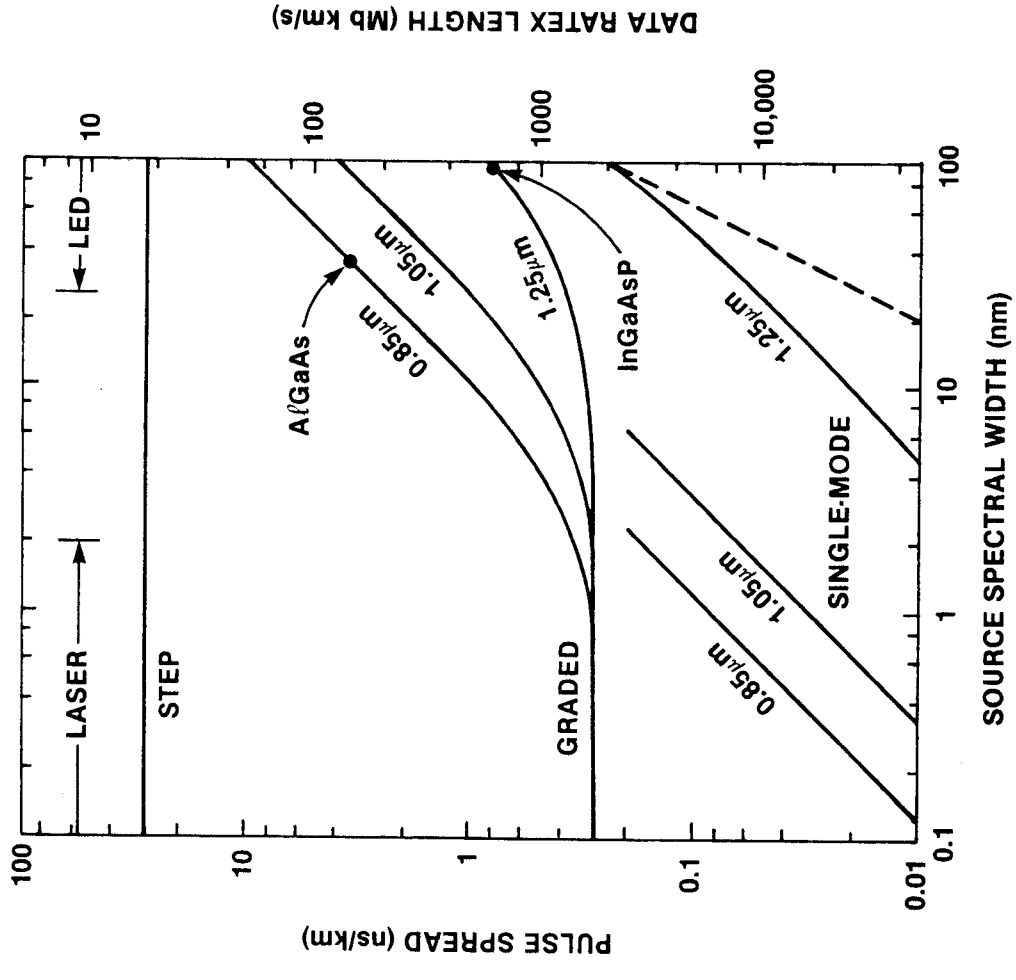
DATA RATEX LENGTH (Mb km/s)
10
100
1000
10,000
LED
LASER
STEP
GRADED
SINGLE-MODE
AℓGaAs
0.85μm
1.05μm
1.25μm
InGaAsP
1.25μm
1.05μm
0.85μm
PULSE SPREAD (ns/km)
100
10
1
0.1
0.01
0.1
1
10
100
SOURCE SPECTRAL WIDTH (nm)

REFERENCE LISTING - CHAPTER 1

1. J.S. Cook, "Bell System Light Wave Links," Technical Digest, IOOC '81, MCI, SFO, April 27-29, 1981.

   International Data Corporation, "Fiber Optics Report."

   Kessler Marketing Intelligence, "Fiber Optics Report."

   Gnostic Concepts, Inc., "Fiber Optics Report."

   M.I. Schwartz, P.F. Gagen, N.E. Hardwick III, "FT^3 Light Guide Transmission Medium - Initial Performance Results," Technical Digest, IOOC '81,

2. P.K. Runge, "Future Transatlantic Fiber Optical Communication Systems," Technical Digest, IOOC '81, MF^1, SFO, April 27-29, 1981.

3. S.E. Miller, "Integrated Optics: An Introduction," Bell System Technical Journal, E.A.J. Marcatili, "Dielectric Rectangular Waveguide and Directional Coupler for Integrated Optics," Vol. 48, No. 7, pp. 2059 and 2071, September 1969.

4. H. Kogelnik, "An Introduction to Integrated Optics," IEEE Trans. Microwave Theory and Techniques, Vol. MTT-23, No. 1, p. 2, 1975.

   H. Kogelnik, "Review of Integrated Optics," AGARD/NATO Symposium on Optical Fibers and Integrated Optics, London, May 1977.

   R. Alferness, "Guided-Wave Devices for Optical Communication," IEEE J. QE, Vol. QE-17, No. 6, p. 946. June 1981.

5. P.K. Tien, "Integrated Optics and New Wave Phenomena in Optical Waveguides," Review of Modern Physics, Vol. 49, No. 2, p. 361, April 1977.

6. Amnon Yariv, "Guided-Wave Optics," Scientific American, Vol. 240, p. 64, January 1979.

7. E.M. Conwell, "Integrated Optics," Physics Today, Vol. 29, p. 48, May 1976.

8. Monographs:

   "Integrated Optics," Editor T. Tamir, Topics in Applied Physics, Vol. 7, First Edition 1975, Second Edition 1979, Springer-Verlag.

9. "Introduction to Integrated Optics," Editor M.K. Barnoski, 1974, Plenum Press.

10. "Integrated Optics," Editor D. Marcuse, 1973, IEEE Press.

11. "Fiber and Integrated Optics," Edited by D.B. Ostrowsky, NATO Advanced Study Institutes Series, Plenum Press 1979.

12. IEEE Transactions on Circuits and Systems, December 1979, Vol. CAS-26, No. 12, "Special Issue on Integrated and Guided Wave Optical Circuits and Systems."

    IEEE J. of Quantum Electronics, "Special Issue on Communications Aspects of Single-Mode Optical Fiber and Integrated Optical Technology," IEEE, Vol. QE-17, No. 6, June 1981.

13. D. Marcuse, "Theory of Dielectric Optical Waveguides," Academic Press, N.Y., 1974.

14. D. Marcuse, "Light Transmission Optics," Van Nostrand Reinhold Co., New York, 1972.

15. N.S. Kapany, J.J. Burke, "Optical Wave Guides," Academic Press, New York, 1972.

16. H. Kogelnic, "Theory of Dielectric Wave Guides," Topics in Applied Physics, Vol. 7 - Integrated Optics, Edited by T. Tamir.

17. P.K. Tien, "Film-Waveguides and Zig-Zag Waves," Introduction to Integrated Optics, Edited by M.K. Barnoski, Plenum Press, 1974.

18. J. McKenna, "The Excitation of Planar Dielectric Waveguides at p-n Junctions, I," Bell Syst. Tech. J., Vol. 46, p. 1491 (1967).

19. P.K. Tien, "Light Waves in Thin Film and Integrated Optics," Appl. Opt., Vol. 10, No. 11, p. 2395 (1971).

20. D. Marcuse, "Mode Conversion Caused by Surface Imperfections of a Dielectric Slab Waveguide," Bell syst. Tech. J., Vol. 48, No. 10, p. 3187, December 1969.

21. D. Marcuse, "Coupling Coefficient for Imperfect Asymmetric Slab Waveguides," Bell Syst. Tech. J., Vol. 52, No. 1, p. 63, February 1972.

22. E.A.J. Marcatili, "Bends in Optical Dielectric Guides," Bell Syst. Tech. J., Vol. 48, p. 2103, September 1969.

23. J.E. Goell, "Loss Mechanisms in Dielectric Waveguides," Introduction to Integrated Optics, Edited by M.K. Barnoski, Plenum Press.

24. E.A.J. Marcatili, S.E. Miller, "Improved Relations Describing Directional Control in Electromagnetic Waveguides," Bell Syst. Tech. J., Vol. 48, No. 7, p. 2161, September 1969.

25. D. Gloge, "Dispersion in Weakly Guiding Fibers," Appl. Optics, Vol. 10, p. 2442, November 1971.

26. S.D. Personick, "Time Dispersion in Dielectric Waveguides," Bell Syst. Technical Journal, Vol 50, p. 843, 1971.

27. F.P. Kapron, D.B. Keck, "Pulse Transmission Through a Dielectric Optical Waveguide," Appl. Optics, Vol. 10, p. 1519, July 1971.

28. T. Li, "Optical Fiber Communication--The State of the Art," IEEE Trans. Commun., Vol. *COM-26*, p. 946, July 1978.

CHAPTER 2

BEAM AND WAVEGUIDE COUPLERS

2.1 Introduction

The basic differences between a dielectric optical waveguide and a metallic microwaveguide are:

1) a dielectric optical waveguide has micrometer dimension and a microwaveguide has centimeter dimension;

2) a dielectric optical waveguide is "open" in that the field extends into the exterior space although most of the energy is within the guide, while the microwaveguide is "closed" and all the wave energy is confined within the guide;

3) The optical laser source which is used to excite a dielectric optical waveguide usually has aperture much larger than the microwave source.

When coupling an optical excitation into a dielectric waveguide, these differences cause different considerations from those involved in coupling microwaves.

The application areas of optical waveguide couplers can be classified into the following categories: beam-to-planar waveguide couplers, beam-to-channel waveguide couplers, planar-to-channel waveguide couplers, channeled-to-channel waveguide couplers, and fiber-to-waveguide couplers. The couplers applicable to the beam-to-planar guide coupling are usually also applicable to the beam-to-channel guide coupling provided some modifications. The channel-

to-channel guide coupling are usually achieved by bringing two guides close to each other. The planar-to-channeled guide couplers usually serve as an intermediate stage for beam to channel guide coupling. The fiber-to-waveguide couplers are the most important for many systems applications.

2.2 Beam-to-Planar Guide Couplers

The coupling of a beam into a planar guide, i.e., one which has a large width, as opposed to channel guides, has been the concern of most coupling experiments performed previously. The various beam-to-planar guide couplers can be classified into two categories: transverse couplers and longitudinal couplers.

2.2.1 Transverse Couplers

The laser beam is incident directly onto the transversal (edge) plane of the waveguide. An optical lens is used to horn-in the beam into the waveguide. This method is also referred to as "head on" or "end fire" coupling.

Two methods of this "head on" approach are illustrated in Figure 2-1. Theoretically, the field-contour matching can be made nearly perfect, for instance, by shaping the lens appropriately. Thus, in principle, the coupling efficiency can nearly be 100%. In practice, however, considerable losses occur if the planar guide edge is not perfectly smooth and clean. Also, critical alignment is needed because the waveguide film thickness is in the order of 1 μm.

2.2.2 Longitudinal Couplers

The laser beam is incident obliquely onto the cover-to-film boundary of the waveguide via a prism, a grating or a taper structure. The prism and grating

couplers are the most important among these couplers.

Prism Coupler

The principle of operation of prism couplers is illustrated in Figure 2-2. Theoretical coupling efficiencies of this type of couplers are nearly 100%. The measured values[1] are approximately 88%.

Grating Coupler

The principle of operation of grating couplers is illustrated in Figure 2-3. The efficiency of this type of couplers can be nearly 100% if the grating thickness and profile shape are suitably designed. However, experimentally measured values have been less than the coupling efficiency of prism coupler.

Tapered Thin-Film Waveguide Couplers

The principle of operation is illustrated in Figure 2-4. This type of waveguide couplers consist of a thin film tapered down onto the substrate. A guided optical wave incident on the taper therefore undergoes zig-zag bounces whose angle of incidence on the film-substrate boundaries decreases progressively as the taper narrows down. As a result, at some point P, the angle of incidence becomes smaller than the critical angle of total reflection and the energy starts refracting into the substrate. This energy is augmented by that of subsequent rays, so that ultimately most of the incidence energy is transformed into an outgoing beam. Although the coupling efficiency of this method is rather high (~70% or more), the divergence of the outgoing rays is large (1° to 20°).

2.3 Planar-to-Channel Waveguide Couplers

Since most of the integrated-optical circuitries will be carried out by means of channel waveguides, it is necessary to be able to transfer further the lightwaves in planar guides into the channel guides.

The most straightforward approach is to gradually taper down the width of the planar guide until it is reduced to the width of the channel guide (Figure 2-5 (a)). A 90% coupling efficiency can be achieved in this coupling scheme.

A different approach is analogous to the prism coupler discussed previously. Here, the planar guide is terminated into a slanted end. The channel guide couples to the planar guide via the evanescent field which appears in the gap between the two guides (Figure 2-5 (b)). To achieve good efficiency, it is necessary to have an accurate and well-defined gap between the two guides. This, however, may not be easily realizable.

2.4 Channel-to-Channel Waveguide Couplers

Channel-to-channel waveguide couplers are used in direction coupling and switching of lightwaves. The two types are described as follows:

2.4.1 Synchronous Type

If two identical channel waveguides are parallel and close to each other over a length L, they will couple energy due to the evanescent field between them (Figure 2-6 (a)). All of the optical energy can theoretically be transferred from one waveguide to another if the coupling length L is chosen correctly. However, the fabrication tolerances are very critical. Thus, the complete energy transform from one channel to the other is very difficult to achieve.

2.4.2 Tapered Coupling

To avoid the tolerance difficulty in the synchronous coupling, Wilson and Teh proposed using a tapered coupling region, as shown in Figure 2-6 (b). Near total energy coupling can theoretically be obtained with a substantially smaller tolerance requirements[3].

2.5 Waveguide-to-Fiber Couplers

The coupling problem of greatest practical importance in integrated optics is to transfer light energy from a planar or channel waveguide to an optical fiber or vice-versa. However, work on these coupling devices has not been extensively studied and no fully satisfactory schemes are as yet available. The difficulty lies primarily on developing a connection scheme which is sufficiently rigid and that the optical coupling efficiency is high enough. Three schemes are illustrated in Figure 2-7, and described in the following:

Leaky-Wave Scheme[4]

A high index immersion fluid is deposited onto the guide-to-fiber junction. The optical fiber picks up the optical energy leaked into the fluid. A coupling efficiency of 50% is usually achieved. However, this scheme is not satisfactory for a permanent set-up, since its rigidity is not sufficient.

Tapered Film Coupler[5]

The fiber is introduced into the substrate through a cylindrical hole and is sealed with an index matching epoxy. The end of the hole is hemispherical and is positioned to collect the energy of the beam radiated through the taper.

Although high coupling efficiency (70%) can be achieved, this method is not suitable for single-mode fibers.

Externally Mounted Coupler[6]

This method uses a rectangular fiber mounted on a tapered channel waveguide. Coupling between linear and strip waveguides to fibers can be achieved with coupling efficiences of 70%.

Figure 2-1 Transverse method for coupling a light beam into a surface waveguide.

(a) Film edge is flush with substrate edge

(b) Film edge is embedded in substrate

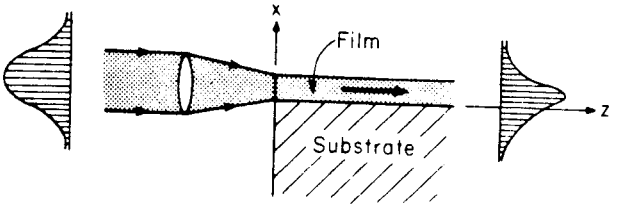

(a)

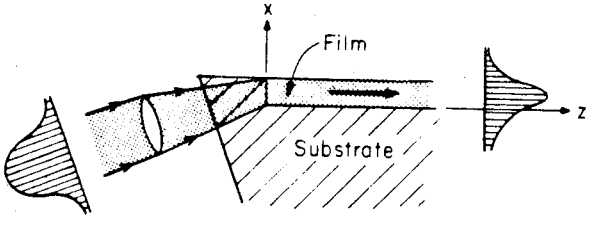

(b)

Figure 2-2 Coupled mode description of prism couplers.

(a) Field of a plane wave incident from a denser medium and undergoing total reflection at the interface to a rarer medium. i.e., $\vartheta > \vartheta_c = \sin^{-1}(n_a/n_p)$.

(b) Field of a surface wave propagating along a thin film with $n_f > n_a, n_s$.

(c) The two preceding configurations can be brought together by letting h_a, become very small, thus obtaining the prism-air-gap-thin-film structure shown here. The incident field now couples to the surface wave via the evanescent field in the air gap.

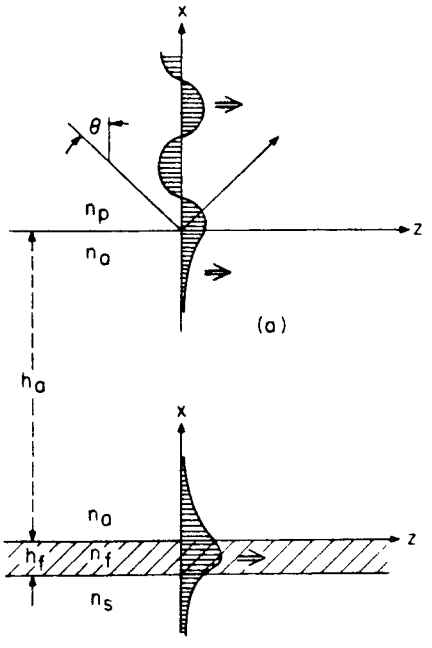

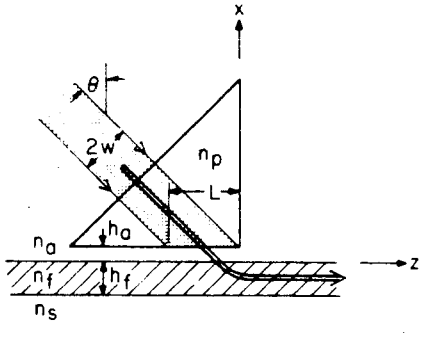

(c)

Figure 2-3 Schematic diagram of a grating coupler.

In well designed couplers, the intensities of the reflected and transmitted beams are weak and most of the energy is coupled to the surface wave. If d/λ is large, additional (diffracted) beams may occur which usually cause undesirable losses.

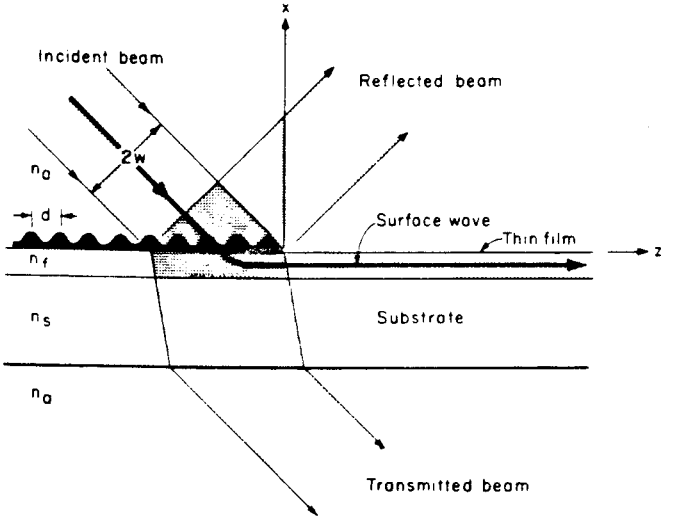
x
Incident beam
Reflected beam
2w
n_a
d
Surface wave
Thin film
z
n_f
n_s
Substrate
n_a
Transmitted beam

Figure 2-4 The tapered thin-film waveguide coupler.

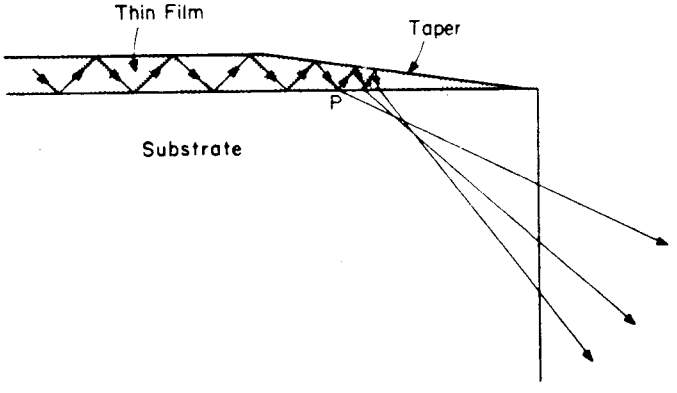
Thin Film
Taper
P
Substrate

Figure 2-5 Connecting a planar guide to a linear guide.
(a) Horn transition.
(b) Prism and gap transition.

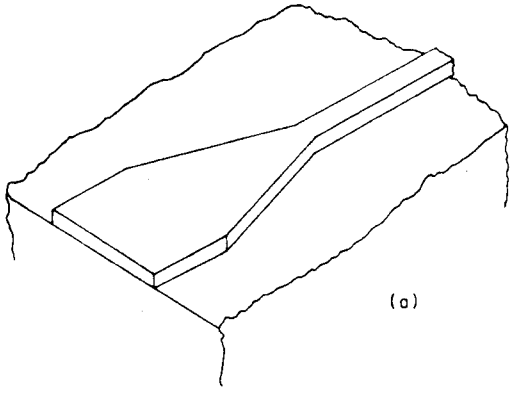
(a)

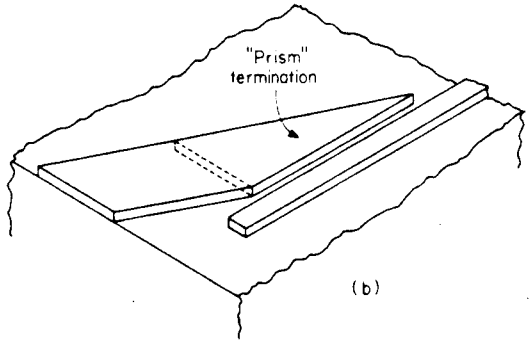
"Prism"
termination
(b)

Figure 2-6 Directional couplers.

(a) Synchronous type.

(b) Tapered coupling. By suitably adjusting the coupling length L, the input power P_{in} may be split into equal or arbitrarily unequal output power P_1 and P_2. For complete energy coupling: $P_1 = 0$ and $P_2 = P_{in}$.

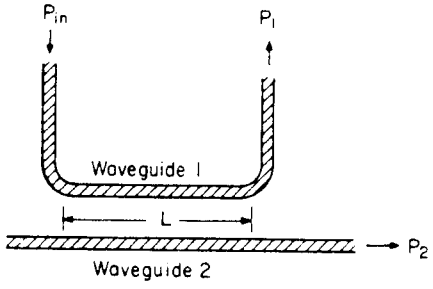
P_{in}
P_1
Waveguide 1
L
P_2
Waveguide 2

(a)

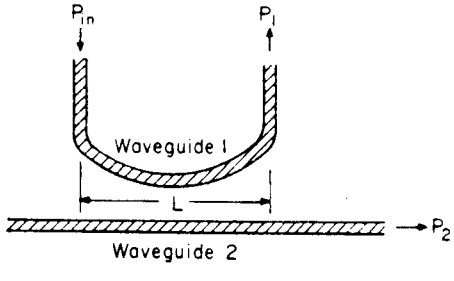
P_{in}
P_1
Waveguide 1
L
P_2
Waveguide 2

(b)

Figure 2-7 Coupling of a waveguide to a fiber.

(a) Leaky-wave coupler.

(b) Tapered-film coupler.

(c) Coupling using a tapered film and an externally mounted fiber.

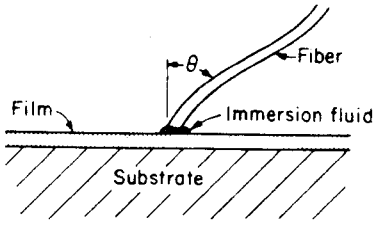
θ
Fiber
Film
Immersion fluid
Substrate

(a)

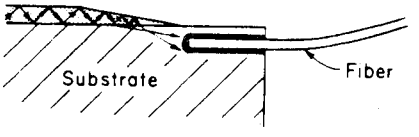
Substrate
Fiber

(b)

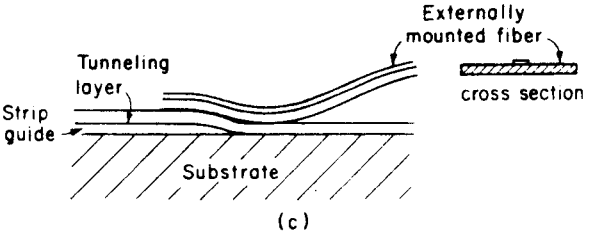
Externally
mounted fiber
Tunneling
layer
cross section
Strip
guide
Substrate

(c)

REFERENCE LISTING - CHAPTER 2

1. J.H. Harris, R. Shubert, "Variable Tunneling Excitation of Optical Surface Waves," IEEE Transaction of Microwave Theories and Techniques, MTT-19, No. 3, p. 269, 1971.

2. S.T. Peng, T. Tamir, "Directional Blazing of Waves Guided by Asymmetrical Dielectrics Gratings," Optical Comm. Vol. 11, No. 4, p. 405, August 1974.

3. M.G.F. Wilson, G.A. Teh, "Improved Tolerance in Optical Directional Couplers," Electron. Lett., Vol. 9, No. 19, p. 453, September 1973.

   "Tapered Velocity Coupling Improves Tolerance in Optical Directional Couplers," Digest of Technical Papers, Topical Meeting on Integrated Optics, p. WB5-1, (Optical Society of America, 1974).

4. R.T. Kersten, "Coupling Between Slab-Waveguide and Glass Fibers," Digest of Technical Papers, Topical Meeting on Integrated Optics, p. WB5-1 (Optical Society of America, 1974).

5. P.K. Tien, G. Smolinsky, R.J. Martin, "Theory and Experiment on a New Film-Fiber Coupler," Digest of Technical Papers, Topical Meeting on Integrated Optics, p. WB6-1 (Optical Society of America, 1974).

6. D.G. Dalgoutte et. al., "Externally Mounted Fibers for Integrated Optics Interconnections," Appl. Opt., Vol. 14, No. 8, p. 1860, August 1975.

CHAPTER 3

THE ACOUSTO-OPTICAL APPLICATIONS

3.1 Bragg Diffraction (Deflection) of Optical Beams

An optical beam incident into an acoustic field can be diffracted by the acoustic waves in the manner a moving grating diffracts the optical beams. The diffracted beam position depends on the frequency of the acoustic waves. The diffracted beam intensity depends, in the first order, on the power of the acoustic waves. The significance is that the acoustic wave can be tuned electronically and thus the diffraction direction and intensity of the optical beam. Multiple diffraction occurs when the acoustic waves have multiple frequency components. Laser scanners, light directional couplers, multichannel light switches, optical convolvers, correlators, optical pulse compressors and real time rf spectrum analyzers can be fabricated using this principle.

Besides the dependence on the acoustic waves, the diffraction also depends on the wavelength of the incident optical beam. An electronically tuned color filter can be realized using this principle.

Bragg diffraction is the result of momentum and energy conservation between the interacting light and acoustic waves. There are two major types of Bragg cells: the isotropic (Fig. 3-1) and the anisotropic (Fig. 3-2). The isotropic diffraction takes place in certain isotropic media, in which the refractive index is constant for the two orthogonally polarized light waves. No polarization change occurs between the incident and the diffracted beams. The anisotropic diffraction takes place in birefringent crystals, in which the refractive index n_e for the extraordinarily polarized light differs from the refractive index n_o for

the ordinarily polarized light. A polarization change between the incident and diffracted beams occurs in this case.

The Bragg conditions for the two types of diffraction are as follows:

$$\textit{Isotropic}: \quad \sin \vartheta_i = \sin \vartheta_d = \sin \Theta_B = (\lambda_o / 2nv_a) \cdot f_a \qquad (3\text{-}1)$$

$$\alpha = 2\,\vartheta_i$$

$$\textit{Anisotropic}: \quad \sin \vartheta_i = \frac{\lambda_o}{2n_i v_a} \left(f_a + \frac{v_a}{f_a \lambda_o^2} (n_i^2 - n_d^2) \right) \qquad (3\text{-}2)$$

$$\sin \vartheta_d = \frac{\lambda_o}{2n_d v_a} \left(f_a - \frac{v_a}{f_a \lambda_o^2} (n_i^2 - n_d^2) \right)$$

$$\alpha = \left[\vartheta_i \right] + \left[\vartheta_d \right]$$

Where ϑ_i = incident beam angle relative to the normal of the acoustic wave traveling direction

ϑ_d = the diffracted beam angle

Θ_B = isotropic Bragg angle

α = the angle between the incident and the diffracted beams

λ_o = incident light wavelength in air

v_a = acoustic wave velocity

f_a = acoustic wave frequency

n = refractive index of the isotropic AO medium

n_i, n_d = refractive indices for the incident beam and diffracted beam (ordinary and extraordinarily polarized lights)

For most materials, Θ_B is in the order of 1° to 2°. Therefore, the angle between the incident and diffracted beams is small. The optical angular aperture is also rather small in single transducer isotropic Bragg devices. In the anisotropic case, the second term in the Bragg formulation (eq. 3-2) dominates; thus, ϑ_i and ϑ_d can vary within a wide range (Fig. 3-3). When $\vartheta_i \sim \vartheta_d \sim \frac{\pi}{2}$; i.e., the optical beams traverse approximately parallel to the acoustic wave, the Bragg cell is called *collinear*. The differentiation between the incident and

deflected beams are performed by polarizer/analyzer.

The optimal performance is usually obtained in non-collinear anisotropic Bragg diffraction, which has high diffraction efficiency, while retaining the large angular aperture. The non-collinear, anisotropic diffraction has both polarization and angular differentiation between the incident and diffracted light beams. The use of polarizers is thus not a requirement. The non-collinear diffraction also allows optimal choice of material.

3.2 The Bulk Acousto-Optical Tunable Filter (AOTF) Traditional Application I

The AOTF devices generally consist of an acoustic transducer bounded to an acousto-optical medium. Optical lenses and polarizers are used depending on the type of AO interaction used and the intended application. The color selection is tuned by varying the acoustic frequency, which is in turn tuned by the input electrical frequency to a given acoustic transducer. The most significant features of AOTFs are their high resolving power, wide tunable range, large angular aperture and their compactness, and the electronic tunability.

No guided-wave approach has been mentioned in the literature to date. The single-mode nature of the thin-film slab waveguide could be the inhibiting factor. However, higher diffraction efficiency and larger dynamic range can be obtained by the guided-wave approach. One could see possible applications of a guided wave AOTF in mode and frequency filtering of a light source, or in measurements of the loss versus frequency of single mode fibers.

3.2.1 Historical Account

A. H. Rosenthal[1], *Fairchild, 1955*

Analyzed and experimented the concept of using ultrasonic waves as a grating monochrometer. The experiments were performed using an ultra-sonic cell consists of an ultra-sonic wave transducer attached to a water tank. The problems of this system were its low optical angular aperture and the generally low performance figures.

R. W. Dixon[2], *Bell Labs, 1967*

Performed theoretical analysis and experiments of acoustic light diffraction in anisotropic AO crystal. The experiments were performed using crystal quartz medium and CdS acoustic transducer.

S. E. Harris and R. W. Wallace[3], *Stanford University, 1969*

First proposed collinear anisotropic AOTF using $LiNbO_3$ (Fig. 3-4).

Advantage: Large angular aperture.

Problem: Low diffraction efficiency, limited material choice, required polarizers.

Z. C. Chang[4,5], *Applied Technology, 1974*

Proposed non-collinear anisotropic AOTF in visible light range using TeO_2 (Fig. 3-5).

Advantages: An order of 500-fold improvement on diffraction efficiency versus electrical power characteristics, while retaining the large angular aperture. The use of polarizers is no longer a requirement.

3.2.2 Recent Activities

Applied Technology, ITEK

Continuous effort on improving spectral resolving power, filtering bandwidth, angular aperture and image resolution. Active in R/D efforts on military applications[6] (Figures 3-6, 3-7).

Matsushita Electronics Components Co. Ltd.

Commercialized (1980) AOTF in visible light regime for TV measurements using far-off axis anisotropic Bragg Diffraction[7] in TeO_2.

Rockwell International

Applied AOTF in tuning the 2-D IR detector arrays in the satellite-based earth-looking IR telescopes[8].

Hughes Aircraft Company

Extensive R & D activities in AOTF military applications.

3.2.3 Current Performance Limitation Figures

Spectral Tuning Range:	200nm to 11 μm using multiple transducers (Fig. 3-8)
Transmission:	>95% for polarized light
Resolving Power:	10 to 10,000
Fractional Bandwidth ($\Delta\lambda/\lambda$):	10% to 0.01%
Angular Aperture:	Up to28°
Linear Aperture:	mm-cm range
Random Access Time:	In the order of μsec to several μsec

Field of View:	14° with polarizers
	6° without polarizers
Drive Power:	A few hundred mW
Contrast Ratio:	2000/1 without polarizers
Image Resolution:	100 lines/mm

3.2.4 Relevance to Tektronix

With the increasing trend of the communications and TV industry turning to fiber optics, our Communications Division is interested in developing a fiber measurement instrument to measure the group envelope delay and the light loss vs. frequency characteristics of optical fibers. The measurement of the spectral sensitivity of TV cameras, the spectral analysis of displays and shutters are also areas of considerable interest to Tektronix. Although the above applications can be achieved by bulk devices, a guided-wave AOTF could provide us with a significant technological barrier in single mode optical fiber measurement instruments.

3.3 Real Time Acousto-Optic Spectrum Analysis (AOSA) Traditional Application II

Acousto-optic spectrum analysis (AOSA) uses an acoustic wave replica of the rf signals under analysis (RFUA) to diffract a coherent light beam. The positions of the diffracted beams correspond to the frequencies of the RFUA components. The intensity of each diffracted beam corresponds to the power of that particular rf component.

3.3.1 Advantages and Deficiencies

The main advantages of AO spectral analysis technique are the real time open receival, 100% intercept, parallel processing capabilities. The deficiencies are the lower dynamic and frequency ranges in comparison to the conventional electrical heterodyne spectrum analyzers. The dynamic range of AOSA systems is presently limited by the amplification circuitry of the optical detectors ($\leq$ 50 dB) employed in the system. The dynamic range of Bragg cell itself usually ranges between 50 dB to 60 dB.

3.3.2 Device Construction

Figure 3-9 shows typical bulk and guided wave AOSA constructions[9,10]. The guided wave version of AOSA has larger dynamic range, greater compactness and ruggedness when compared to the bulk version. Other performance capabilities are approximately the same. Figure 3-10 shows two of the possible SAW transducer configurations of a wide-band guided-wave AOSA device[11].

3.3.3 Applications and Performance Figures

The applications mainly lie in the realms of radar and electronic warfare surveillance, or in some communication areas where the signal environment is dense and a fast processing of the signals is required. AOSA is the most useful when the band of interest contains a large number of signals of different types of amplitudes and frequencies, or when the signals are pulsed; for example, when frequency hopping spread-spectrum techniques are applied to the generation of the signals under analysis.

Applied Technology manufactures bulk Bragg cells and Instantaneous Fourier Transform (IFT) processors using bulk Bragg cells. Their performance figures, limitations and the costs are summarized as follows:

Bragg Cells

Bandwidth	40 MHz → 1 GHz
Central Frequency	60 MHz → 2 GHz
Resolution	0.1 MHz → 1 MHz
Optical Scattering (Noise)	-55 dB
Linearity	0.1% non-linearity across the band
Processing Time Aperture	in the order of μsec, depending on the resolution requirement
Diffraction Efficiency	70% → 0.7%/rf Watt, depending on the frequency bandwidth of the cell
Input Power Capability	0.5 watt average
Costs	6,000 → 8,000 dollars

IFT Processors and Systems

Instantaneous Bandwidth per Bragg Cell	500 MHz - 1 GHz
Frequency Detection Range	up to 18 GHz with 1 GHz windows using multiple Bragg cells and frequency mixer
Frequency Measurement Quantization	512 → 1000 contiguous channels, 1 MHz-wide channels
Measurement Time	0.5 msec → 100 msec
Dynamic Range	25 dB → 60 dB
Costs	40,000 dollars for basic IFP; up to 300,000 dollars for computerized multiple cell systems

The integrated-optic (guided wave) version of the AOSA is still at R/D stage at the present time. Rockwell International[12], Hughes Aircraft Company[10], Westinghouse Electric Company[13] and some major military laboratories have

been the most active pursuers. Performance figures of their results are summarized in Table 3-1. Rockwell International has since abandoned the project. The speculation is that their decision on choosing silicon as the substrate material was not successful.

Figure 3-11 shows a simplified block diagram of an AO receiver.

3.3.4 Related Applications

Convolution and correlation using surface-wave AO technique can achieve more than 5 times increase on interaction time (40 μsec to 80 μsec) compared to pure acoustic or acousto-electric convolvers. The time-bandwidth product achievable with AO devices is generally 5 to 10 times higher than the pure acoustic devices. This is very helpful in real-time detection of spread-spectrum signals in radar, communications and navigation systems. However, the present state of the AO technology is not as mature as the acoustic technology. The bulkiness of the optical components in bulk AO devices is often the major disadvantage when compared to the acoustic devices with comparable performance. The success of the integrated optics technology will be the key to the feasibility of the AO convolvers and correlators.

Figure 3-12 shows a time integrating correlator described by C.S. Tsai[14] of Carnegie-Mellon University. Figure 3-13 shows the concept of a two beam time-integrating correlator. Figure 3-14 shows a possible AO triple product convolver architecture. More detailed discussions on various AO Fourier Transform, convolution and correlation techniques can be found in reference 15.

3.4 AO Laser Scanners for Hard Copy Applications at Tek

AO Bragg diffraction can be used as a laser scanner by varying the frequency of the electrical control signal applied to the acoustic transducers of a

Bragg cell.

3.4.1 Number of Resolvable Spots and Scan Speed

A first order relationship between the total number of resolvable spots N, the device bandwidth Δf and the transit time τ (of acoustic wave across the laser beam width) exists:

$$N = \tau \cdot \Delta f$$
$$\tau = D_o / v_a$$

where D_o is the laser beam width; τ is also the random access time for switching the laser beam from any position N to any other position N' within the scanning range.

Traditionally, it was difficult to obtain large device bandwidth with bulk Bragg cells. To achieve the attractive number of resolvable spots, one usually had to increase the random access time τ to an extent that the scanning speed is no longer satisfactory.

In recent years, the advancements in surface acoustic wave and AO technology have drastically improved the AO device bandwidth. As reported by various laboratories, 500 MHz to 1 GHz bandwidths have been achieved in both bulk and guided wave Bragg devices without major difficulties.

Using a device with 500 MHz bandwidth, the corresponding number of resolvable spot N and random access time τ are as the following:

N	= 500 MHz . τ
2,000	4 μsec
1,000	2 μsec
500	1 μsec

where τ is tailored by the laser beamwidth of the device.

In hard copy operation, it is seldom that all spots on the page are written. A writing ratio W (number of written spots/total number of spots) of 0.25 is a reasonable approximation. We could derive sets of line writing time T and the writing speed S, corresponding to the above N, τ pairs at W=0.25 as follows:

$W = 0.25$
$T = N \cdot W \cdot \tau$
$S = N/T$

T (μsec)	S (spots/sec)	N	τ (μsec)
2,000	10^6	2,000	4
500	$2 \cdot 10^6$	1,000	2
125	$4 \cdot 10^6$	500	1

This set of parameters strongly suggests that AO technology is suitable for high speed non-impact hard copy applications.

3.4.2 Further Increase in N at Constant τ

The number of resolvable spots N could be doubled without sacrificing the random access time τ by using special techniques. The symmetry property of AO Bragg devices is the underlying foundation for the implementation of such techniques. Examples of such implementation are as the following:

Symmetric Waveguides

A laser source can be switched between an interdigitated phase grating. The waveguide channels guide the laser beams to enter the acoustic field at the two symmetric Bragg angles Θ_B and $-\Theta_B$. For the Θ_B incidence, the diffracted beam positions are ranged in the upper half of the writing plane. For the $-\Theta_B$ incidence, the diffracted beam positions are ranged in the lower half of the writing plane. This concept is illustrated in Figure 3-15.

Symmetry property can also be exploited by operating a set of two SAW transducers with mirror symmetry relative to each other. Theoretically, the laser beam will be diffracted to two beams when both transducers are operated independently and simultaneously. In this case, both N and scanning speed S are doubled. Figure 3-16 illustrates this implementation.

However, if the writing intensity is a matter of concern, the two transducers can be operated in a time-sharing manner. Or, a higher power optical source can be used.

A nearly 100% diffraction is important in these type of operations. Otherwise, undesired writing could be caused by the zero order (undiffracted) beam. Employing zero order stops could possibly solve this problem.

3.4.3 Increase in Writing Speed S at Constant N and T

Time parallel multiple diffraction can be implemented to multiply the writing speed without sacrificing the number of resolvable spots N. If we simultaneously drive the SAW transducer of the device with multiple frequencies, the incident laser beam would be diffracted into multiple writing beams positioned by the corresponding frequencies. The total writing speed is thus multiplied. The linearity of the device through the bandwidth is important in this technique. From Section 3.3.3, a 0.1% error in linearity across the band was demonstrated by commercially available Applied Technology bulk Bragg cells.

3.4.4 Performance Summary

A set of performance figures for hard copy application are derived from state-of-the-art capabilities of AO devices:

Resolution	~2000 spots/line
Scan speed	$>10^6$ spots/sec
Contrast	>1000/1 for single diffraction
Linearity	<0.1% error across band
Random access time	order of μsec
Angular scan aperture	a few degrees, expansion optics will be required
Spot shape	Circular Gaussian distribution when using bulk device Rectangular Gaussian distribution when using guided-wave device.

3.4.5 Application Example

Diamond Research Corporation (Ventura, California) has licensed for production a "shaped laser" printer, developed by an independent consultant Joseph T. McNaney (San Diego, California). The "shaped laser" printer uses a stenciled mask plate consisting of 75 characters and symbols, illuminated by 75 laser diodes. An AO Bragg cell deflects the character formed laser beams to the proper positions desired on the printing medium. The selection of the proper character is addressed by turning "on" of a specific laser diode. The placement of the character to the proper position on the printing medium is performed by the AO Bragg cell. The addressing scheme of this approach is extremely simple compared to the "dot matrix" approach. The print quality and flexibility is also much improved. The profit margin of this printer could be very high for its high performance and relatively simple mechanism.

3.5 Optical Digital Video Routing Switcher Application at Tektronix

3.5.1 Performance Criteria

Grass Valley Group of Communications Division has expressed strong interest in optically routing switch optical digital video signals for high data rate digital video processing. The tentative set of desired performance criteria indicated by a Grass Valley engineer are as follows:

- 200 MHz → 300 MHz data rate
- 100 input programs switched to 100 receiving channels
- Capability of switching each input program to any combination of the 100 output channels
- No mixing of more than one program at a given time at any output channel
- 1 μsec switching time
- Parallel switching
- In-station and in-studio operation

3.5.2 Device Description

Integrated-optic AO Bragg diffraction can be utilized in this application (an electro-optic approach will be described in Chapter 4). The digital video signals are impressed on modulated laser sources, then piped down to the switcher by single mode optical fibers. The laser sources can also be directly bounded to or integrated on the switcher substrate (if suitable material and fabrication processes are used), and converged, collimated to required beam width by thin film lenses on the switcher substrate.

The conceived switcher is an integration of a number (M) of "1 input to N output" AO Bragg switches. One set of acoustic transducer is individually responsible for each 1 to N switch. The M output ports of the M input channels corresponding to the same designated receiving channel are converged by a large thin film lens.

The number of switches (M), integrable on one substrate depends on the substrate size, the switch geometry, and the optical beam width required. For our application, it is conceivable that 20 switches can be integrated on a 1.5 inch substrate. A 100 → 100 switcher system can then be composed of 5 substrates.

Figure 3-17 illustrates the concept of the switcher. Symmetric transducer pairs could be used to lower the bandwidth requirement of each device for a given number of receiving channels desired.

The output ports on a single substrate are converged by a large thin film lens. Corresponding output ports on separate substrates can be bundled together by optical fibers. If conversion to electrical signal is desired for signal amplification and processing, photodetector array can be edgebound to or integrated (if suitable material is used) on the substrates. In this case the recombination of the corresponding receiving channels on separate substrates can simply be electrically paralleled together.

The switching of each optical video signal to the designated receiving channels is frequency controlled by the electrical control signals synthesized and applied to the acoustic transducer pair responsible to that input channel. Parallel switching is achieved by parallel application of the control signals to the transducers responsible to the input channels to be switched.

3.5.3 Synthesis of Control Signals

The programming and synthesis of control signals are potentially a difficult task.

A conceivable algorithm is described in Figure 3-18. One hundred oscillators generate sinusoidal oscillations with appropriately spaced frequencies f_n (for the first order, $f_n = f_o + n\Delta f$). The power amplitudes of the oscillators are band-shape adjusted. With programmable electrical switch network, a computer, or data processor selects the set of oscillators for switching the first input channel. The processor then proceeds to select the set of oscillators from the remaining oscillators for the second input channel. Then, the oscillators for switching the third video input channel are selected from the remaining oscillators, ... This process proceeds until all the oscillators are connected to the acoustic transducers, or all the switching operations are completed, whichever comes first. To avoid the mixed receiving of more than one video programs at any one output channel, each oscillator can only be used once.

When symmetric acoustic transducers are implemented, only half the number of oscillators would be needed. In this case, one oscillator can be used twice: once by the "left" side transducers, for the diffraction to the lower half of the receiving channels, once by the "right" side transducers, for the diffraction to the upper half of the receiving channels.

3.5.4 Resolution, Frequency, Bandwidth and Random Access Time

In AO Bragg diffraction terms, the set of system performance criteria described in Section 3.5.1 translates to device frequency resolution, frequency f, frequency bandwidth Δf, and random access (transit) time τ. To be more specific:

- The 100 desired receiving channels correspond to the requirement of $N \geq 100$ ($N \geq 50$ when symmetry property is employed).
- The μsec switching time corresponds to the random transit time $\tau \sim 1$ μsec.
- The 200 MHz to 300 MHz video data rate corresponds to SAW frequencies larger than 400 MHz to 600 MHz (Nyquist criterion).

The time, bandwidth product relationship stated in Section 3.4 is generally applicable to AO Bragg diffraction cells:

$$N = \Delta f \cdot \tau$$
$$\tau = D_o / v_a$$

This results in the following set of device specifications:

Bandwidth

For $N \geq 100$, and $\tau \sim 1$ μsec, the required bandwidth Δf must be larger than 100 MHz (or 50 MHz when symmetry property is used).

The state-of-the-art capability of integrated optical AO Bragg device is well above 500 MHz as reported by several AOSA teams. This allows a large margin above our requirement. A bandwidth larger than that required, however, is helpful in optimizing channel isolation.

SAW Frequency

The 400 MHz to 600 MHz Nyquist frequency is also well below the upper bound of the technology (~ 2 GHz). In fact, it is easier to obtain a larger bandwidth at higher frequencies.

Optical Aperture

The SAW velocity v_a in $LiNbO_3$ is approximately 3.5×10^3 m/sec. This results in an optical aperture (truncated collimated beam width) D_o,

$$D_o \leq 10^{-6}\ sec\ .\ 3.5\ x\ 10^3\ m/sec = 3.5\ mm,$$

which does not imply apparent difficulty.

3.5.5 Sidelobes

The effect of finite optical aperture is to weight the acoustic modulation of the laser beam with a rectangular function. Under Fourier Transform, (which is eventually what we are doing in this device) this rectangular weighting function results in a $sinc^2\ (\pi s)$ power spectrum ($s = f\tau$). The implication is that to each acoustic frequency and each order of diffraction (in Bragg devices, the diffractions above the first order are negligible), there are sidelobes described by the function $sinc^2\ (\pi s)$. The amplitude of the sidelobes are further apodized by the profile of the incident optical beam. Finally the acoustic loss across the laser beam tends to increase slightly the sidelobe level.

The optical intensity at the frequency plane (output plane) can be expressed as:

$$I\ (f\ ,t) = |\overline{V}(f\ ,t)|^2$$

where $\overline{V}$ (f,t) is the Fourier transform of the control electrical waveform at the acoustic transducer weighted by the three factors: finite optical aperture, light beam amplitude profile, and the acoustic loss across the optical beam:

$$\overline{V}\ (f\ ,t) = \int_{-\infty}^{\infty} W_1 \cdot W_2 \cdot W_3\ (t - t')\, V sin\ (2\pi f t') \cdot e^{-2\pi f t'}\, dt'.$$

Finite Aperture

For a rectangular truncation of the incident optical beam, W_1 is described as:

$$W_1\ (t\ ,\tau) = rect\ (\frac{t}{\tau} - \frac{1}{2})$$

where τ is the transit time of the acoustic wave across the optical beam:

$$\tau = D_o / v_a .$$

Gaussian Apodization

Using a truncated Gaussian beam profile the sidelobe level can be drastically apodized:

$$W_2 (t, \tau, T) = e^{-4T^2(\frac{t}{\tau} - \frac{1}{2})^2}$$

Where T is the ratio of the beam aperture to the e^{-2} intensity width of the Gaussian profile:

$$T = D_o / 2u_{1/2}$$

and

$$I (w_{1/2}) = I_o \, e^{-2}$$

Acoustic Loss

The weighting due to acoustic loss is an exponential decay on the index modulation:

$$W_3 (t, \alpha) = e^{-\alpha t},$$

where

$$\alpha = \frac{\Gamma f^2 v_a}{20 \log_{10} e} \cdot nepers/sec,$$

Γ is an acoustic material coefficient governing the acoustic loss in units of dB/cm GHz^2. Since our optical beam aperture D_o is relatively small, the effect of acoustic loss is relatively small when compared with the effect of the Gaussian truncation (Figure 3-19).

The Fourier Transform

The optical intensity at the frequency plane is the square of the Fourier transform of $W \cdot V$:

$$I(f,t) = (F\{W \cdot V\})^2,$$

where

$$W = W_1 \cdot W_2 \cdot W_3$$
$$V = V\sin(2\pi f t').$$

The Fourier transform of $W \cdot V$ is the convolution of the Fourier transform of W and V:

$$F\{W \cdot V\} = F\{W\} * F\{V\}.$$

And

$$F\{W\} = AF\{e^{-\alpha\tau(u+\frac{1}{2})}\} * F\{e^{-(2Tu)^2}\} * F\{rect(u)\}$$

$$where \quad u = \frac{t}{\tau} - \frac{1}{2}.$$

The finite aperture term F {rect (u)} results to a $sinc^2$ ($\pi f\tau$) oscillatory spectrum. The Gaussian apodization term F $\{e^{-(2Tu)^2}\}$ results to a drastic reduction of the sidelobe amplitudes, i.e.,

$$(F\{e^{-(2Tu)^2}\})^2 \ \alpha \ (e^{-T^2} \cdot e^{-(f\tau)^2})^2.$$

Figure 3-19 (a) shows the ratio of the largest sidelobe intensity to be the mainlobe ($I_{sidelobe}/I_{mainlobe}$) in dB, versus the Gaussian truncation ratio T, at zero dB acoustic loss and 12 dB acoustic loss. We see that the sidelobe can be depressed to below -50 dB when T is chosen to be above 2.

This amplitude apodization is achieved at the cost of the half (power) width of the mainlobe. The effect of the widening is shown in Figure 3-19 (b). The mainlobe width, however, does not exceed the node length of the *sinc* function. This implies that if we choose to use only every other resolvable channel, the effect of the sidelobe can be minimized to negligibility in all practical sense.

Temporal and Spatial Frequency Resolution

Since the node length of $sinc^2$ power spectrum is 1, the temporal frequency resolution Δf is thus equal to $1/\tau$. The spatial frequency resolution Δf_x ($f_x = f/v_a$) is equal to $1/D_o$:

$$\Delta s = \Delta f \tau = \Delta (f/v_a) \cdot D_o = 1$$
$$\Delta f = 1/\tau$$
$$\Delta f_x = 1/D_o$$

3.5.6 Intermodulation

When multiple frequencies are applied to an acoustic transducer to generate multiple diffracted beams, each beam is not completely independent of the others. Light in each principal diffracted beam may be rediffracted by another acoustic wave. Each diffracted beam also depletes the source beam from which all diffracted beams are generated. Such complexity causes intermodulation. Figure 3-20 shows an exaggeration of this situation. The magnitudes of the intermodulation modes for two frequencies are shown in Figure 3-20 (b) and discussed in reference 16.

When the diffraction efficiencies are constrained to the order of 1% per frequency channel, and frequency bandwidth is limited to one octave to avoid harmonic responses, the dynamic range of above 50 dB can be achieved.

Since our input channels are isolated from one another, no intermodulation between beams diffracted from different input beams (individual input channels) is expected. The only source of intermodulation is contained within individual input channels. Therefore, the level of intermodulation can be expected to be similar to that of an AO spectrum analyzer. Further discussion will be seen in Section 3.5.7.

3.5.7 Optical Background and Signal to Noise Ratio

The optical background at the output plane is due to optical scattering of the waveguide, the sidelobes, and the intermodulation modes.

Optical scattering was discussed in Chapter 1. Sidelobes can reasonably be suppressed to the level of -50 dB to -70 dB as discussed in Section 3.5.5. Intermodulation level can also be reduced to below -50 dB level as discussed in Section 3.5.6.

For a single channel integrated-optic Bragg device (1 to N diffraction), excluding the photodetectors, the dynamic range is usually 50 dB or better, as reported in IO spectrum analyzer related works (Table 3-1). Since the measured noise level includes all three major noise sources (optical scattering, sidelobes and intermodulation), each individual noise should be considerably less than the total noise.

The effect of the integration of multiple Bragg devices to the system noise mainly lie on the question of whether we have an effect of summing noise.

The fact that each frequency can be used only once, such that no single receiving channel would simultaneously receive more than one input program, eliminates the possibility of summing sidelobes at same location on the frequency (output) plane.

The different frequencies applied to the transducers of separate input channels do not intermodulate since all input channels and their corresponding acoustic fields are isolated from one another. The worst case of intermodulation noise occurs when all 100 receiving channels receive the same program. In this case, all 100 frequencies are biased to the acoustic transducer of the same input channel to diffract the same input light beam. The lowest order intermodulation modes which lie within the bandwidth, are the modes with frequencies $2f_n - f_m$ (where n,m are integers and n,m < 100). For the reason that the control frequencies ($f_n = f_o + n\Delta f$) are uniformly incremented, a considerable number of overlapping modes do occur.

The theoretical calculation of the intensity of the intermodulating modes relative to the source results in approximately a -50 dB intensity for the $2f_n - f_m$ (3rd order) modes and below -80 dB for the $3f_n - f_m$ (5th order) modes, if the diffraction efficiencies for each principal diffracted beams are limited to 10%. The ratio of the intermodulating modes to the principal modes is thus approximately -40 dB (Figure 3-20). Considering the situation where ten overlapping ($2f_n - f_m$) modes occur, the total noise to signal ratio would be -30 dB. However, this intermodulation overlap exists also in the integrated-optical spectrum analyzer, which typically could have well over 500 instantaneous parallel RF detection channels.

Theoretically, we can conclude that the noise level and the dynamic range of the integrated-optical AO network switch should be similar to those observed in the integrated-optical AO spectrum analyzers, as listed in table 3-1.

3.5.8 Coupling Efficiency - Material Considerations

Most integrated-optical acousto-optic devices studied to date are single element devices consisting of a SAW transducer fabricated on a Ti-indiffused $LiNbO_3$ planar waveguide. Higher optical diffraction efficiency in these devices are achieved by increasing the rf driving power applied on the SAW transducer. Power coupling efficiency is generally disregarded.

When integration of an array of devices on a single substrate is needed, such as in our case, the power coupling efficiency becomes very important. The two power coupling efficiency aspects in the acousto-optic diffraction, piezoelectric and acousto-optic, are unfortunately mismatched from the standpoint of material properties.

Piezoelectricity

The conversion efficiency from electric power to acoustic power of a piezoelectric material can be measured in terms of $\Delta v_a/v_a$, the fractional change in the phase velocity of a surface wave due to the piezoelectricity, produced by shorting out the surface *potential*[17] with a conducting layer:

$$\Delta v_a/v = (v_{short} - v_a)/v_a \quad .$$

Out of the commonly known piezo-electric materials $liNbO_3$ has the highest $\Delta v_a/v$ value (Table 3-2). However, the acousto-optic coupling efficiency of $liNbO_3$ is fair at the best when compared to other acousto-optic materials (Table 3-3).

Acousto-Optic Diffraction Efficiency

The acousto-optic diffraction efficiency I, at Bragg regime is determined by:

$$I_1 = \sin^2 [\frac{1}{\sqrt{2}} \frac{\pi}{\lambda_o \cos \vartheta_o} (M_2 \frac{P_a L}{H})^{\frac{1}{2}}] \mathbf{H}$$

where P_a is the acoustic power, L/H is the acoustic aspect ratio, L is the acoustic beam width and H is the beam height, M_2 is the acousto-optic figure of merit. ϑ is the Bragg angle, λ_o is the optical wavelength, **H** is the effective overlapping factor of the acoustic wave and optical wave.

Material constants determine the acousto-optic figure of merit M_2:

$$M_2 = (n_j^6 p_{ijkl}^2 / \rho v_a^3)$$

where n is the refractive index, p is the opto-electric coefficient, ρ is the density of the material, v_a is the acoustic velocity. Table 3-3 shows the acousto-optic figure of merit of various materials. Crystalline α-HgS and amorphous As_2S_3 show the highest M_2 values among those materials listed. More extensive listings can be found in references 18 and 19.

$LiNbO_3$, though has the highest piezoelectric coupling coefficient and the lowest acoustic loss, its acousto-optic figure of merit M_2 is only 7.0 compared to 104 of GaAs, 433 of As_2S_3 and 960 of α-HgS crystal. It is thus most desirable to grow α-HgS crystal layer or deposit As_2S_3 film on a $LiNbO_3$ substrate to obtain better overall power efficiency. The latter is technically more feasible. However with advancing thin film crystal growth technique it may be possible to grow α-HgS crystal on $LiNbO_3$ substrate in the future. Another possibility is to grow thin strip of $LiNbO_3$ crystal as transducer material on a glass substrate and deposit As_2S_3 film as AO medium.

Table 3-4 lists some power data extracted from previous acousto-optic experiments reported by several research laboratories.

3.5.9 Gain Switching

The AO Bragg diffraction will not amplify the input optical signal. If gain switching is required, a repeater array will be needed. This repeater array could consist of photodetectors, heterojunction bipolar transistors, and injection lasers.

Silicon-based photodetector array has been successfully employed in integrated-optic AO spectrum analyzers. GaAs based photodetectors are actively pursued in many laboratories for optical fiber communications application.

Monolithic integration of GaAs/GaAlAs MESFET with injection laser was reported recently[21,22,23]. Monolithic integration of an injection laser with a heterojunction bipolar transistor on an n+ GaAs *substrate*[24], and a monolithically integrated repeater, consisting of three MESFETs and one laser diode, was also reported[25]. When the technology and fabrication processes for an individual element are established, the array integration does not involve a major difficulty. Work is currently under development at Bell Laboratories and Cal Tech on integrating an array of lasers on a single substrate. The prospect of monolithically integrated repeater array on GaAs substrate is promising from the current state-of-the-art and the trend in GaAl As electro-optics research.

For longer wavelength operations, GaInAsP/InP lasers and GaInAs/InP photodetectors have been extensively studied for several years (see Chapter 5). However, no integration has been attempted to date.

Table 3-1

INTEGRATED-OPTICAL SPECTRUM ANALYZER PARAMETERS AND PERFORMANCE

IOSA Device Parameters	*Westinghouse*	*Hughes*	*Rockwell*
RF Signal Bandwidth	400 MHz	500 MHz	230 MHz
Center Frequency	600 MHz	1 GHz	365 MHz
Frequency Resolution (Detector Width & Spacing Limited)	4 MHz	4 MHz	0.76 MHz
Optical Aperture	0.22 cm	0.74 cm	1.4 cm
Lens Focal Length		1.88 cm	1.5 cm
Acoustic Transit Time	0.6 μsec	2 μsec	4 μsec
SAW Transducer	2 Element Interdigital Tilted Array	Modified Chirp	3 Element Interdigital Tilted Array
Diffraction Efficiency	50 to 100%/Watt	5%	20%
Substrate Material	Ti: $LiNbO_3$	Ti: $LiNbO_3$	Silicon
Detector Period	12 μm		4 μm
Detector Width		8 μm	2 μm
Number of Detectors	140		663
Dynamic Range	42dB Demonstrated 50 dB Expected (Detector Amplification Circuitry Limited)	41.5dB Demonstrated 50dB Expected (Detector Amplification Circuitry Limited)	35dB (Optical Scattering Limited)
Optical Cross Talk		-28dB	
Detector Type	Self Scanned Silicon Photodiode Array	Polysilicon MOS	Silicon p-i-n Photodiode Array

Table 3-2 Piezoelectricity: $\Delta V/V$ of Various Materials

Material	$-\Delta V/V$ ($\times 10^{-3}$)
ZnO	4.5
$LiNbO_3$	24-28
GaAs	0.08
Quartz	0.58-1.0
B GO	6.8
TeO_2	0.2

Table 3-3

ACOUSTO-OPTIC FIGURE OF MERIT M_2 OF VARIOUS MATERIALS

Material	Γ ($dB/cmGHz^2$)	$M_2(10^{-18}s^3/g)$	λ (μm)
$LiNbO_3$ (Crystalline)	0.15	7.0	0.4-4.5
GaAs (Crystalline)	30	104	1-11
TeO_2 (Crystalline)	15	34.5	0.35-5
α-HgS (Crystalline)	28.5	960	0.62-16
As_2S_3 (Glass)	170	433	0.6-11

Γ is the acoustic propagation loss.

λ is the optical wavelength.

Table 3-4

DATA AVAILABLE FROM THE PREVIOUS EXPERIMENTS

	Material	$P_{electric}$	$P_{acoustic}$	$P_{effective\ acoustic}$	*Diffraction Efficiency*	M_2
Ohmachi[20]	As_2S_3 on $LiNbO_3$	152 mW	27 mW	1.4 mW	100%	433
Tsai[19]	Ti-diffused $LiNbO_3$	50 mW			70%	7
Tsai	Ti-diffused $LiNbO_3$	200 mW			50%	7
Tsai	Ti-diffused $LiNbO_3$ Phase Array	68 mW	3.5 mW		50%	7
Feasible	As_2S_3 on $LiNbO_3$	20 mW		1.4 mW	100%	433

Figure 3-1 Isotropic Bragg Diffraction:

The AO medium is isotropic ($n_e = n_o = n$). The incident angle ϑ_i is equal to the Bragg angle Θ_B. The diffraction angle is approximately equal to the incident angle. No polarization change takes place.

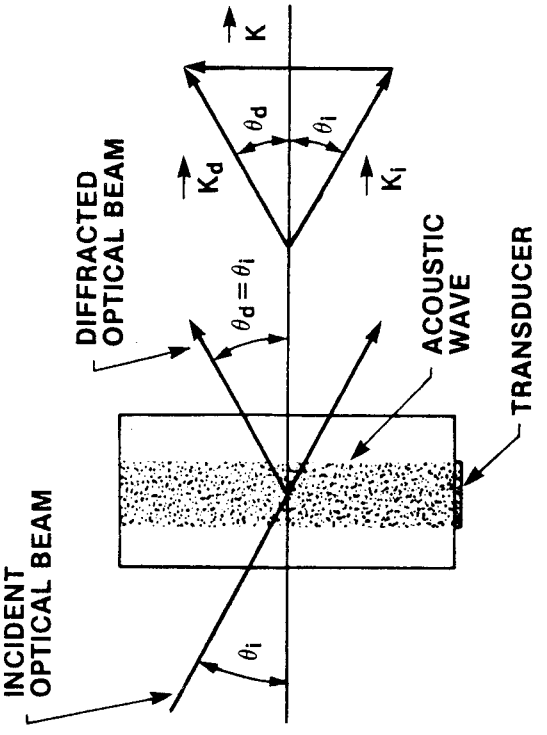
K
K_d
K_i
θ_d
θ_i
DIFFRACTED OPTICAL BEAM
$\theta_d = \theta_i$
ACOUSTIC WAVE
TRANSDUCER
INCIDENT OPTICAL BEAM
θ_i

Figure 3-2 Anisotropic Bragg Diffraction:

The AO medium is anisotropic i.e., $n_e \neq n_o$. The polarization of the diffracted beam is orthogonal to the polarization of the incident beam.

(a) Non-collinear

$\vartheta_i \neq \vartheta_d$, thus the incident and diffracted beams are spatially separated.

(b) Collinear

The incident and the diffracted optical beams both travel parallel to the acoustic waves.

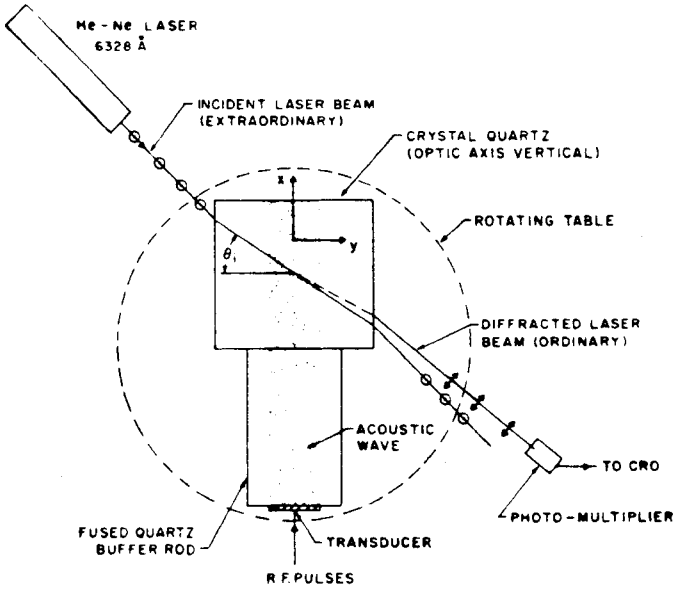
He - Ne LASER
6328 Å
INCIDENT LASER BEAM
(EXTRAORDINARY)
CRYSTAL QUARTZ
(OPTIC AXIS VERTICAL)
ROTATING TABLE
DIFFRACTED LASER
BEAM (ORDINARY)
ACOUSTIC
WAVE
TO CRO
PHOTO - MULTIPLIER
FUSED QUARTZ
BUFFER ROD
TRANSDUCER
R.F. PULSES

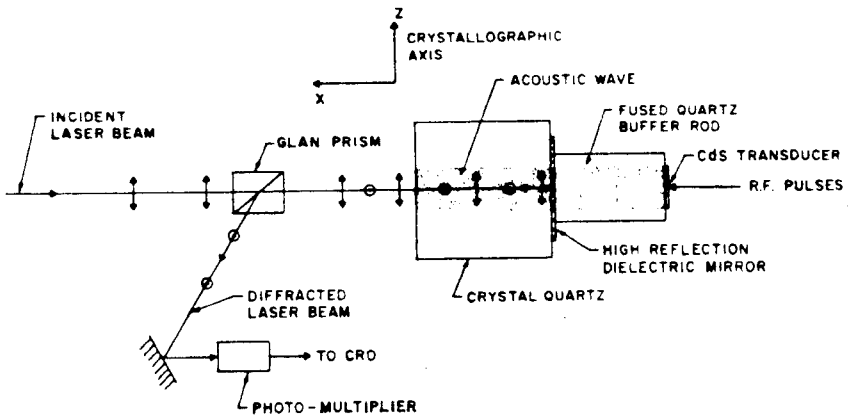
Z
CRYSTALLOGRAPHIC
AXIS
X
ACOUSTIC WAVE
FUSED QUARTZ
BUFFER ROD
INCIDENT
LASER BEAM
GLAN PRISM
CdS TRANSDUCER
R.F. PULSES
HIGH REFLECTION
DIELECTRIC MIRROR
DIFFRACTED
LASER BEAM
CRYSTAL QUARTZ
TO CRO
PHOTO - MULTIPLIER

(a)

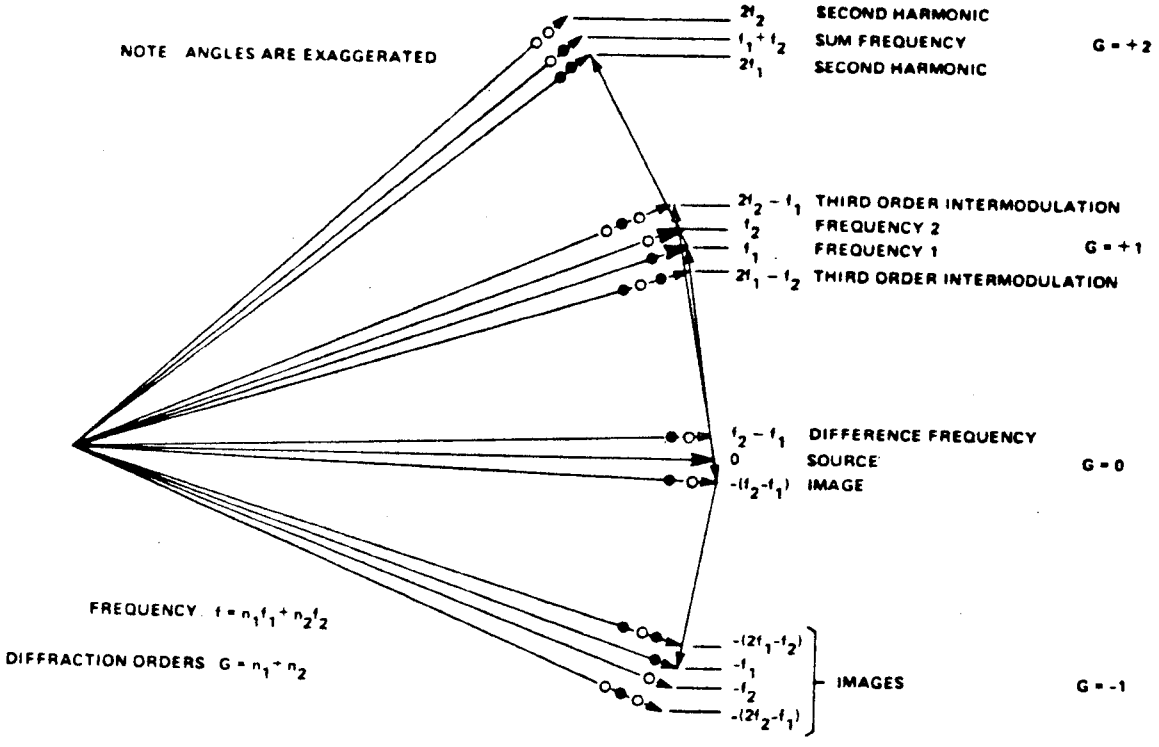
NOTE ANGLES ARE EXAGGERATED
$2f_2$ SECOND HARMONIC
f_1+f_2 SUM FREQUENCY
$2f_1$ SECOND HARMONIC
G = +2
$2f_2-f_1$ THIRD ORDER INTERMODULATION
f_2 FREQUENCY 2
f_1 FREQUENCY 1
G = +1
$2f_1-f_2$ THIRD ORDER INTERMODULATION
f_2-f_1 DIFFERENCE FREQUENCY
0 SOURCE
$-(f_2-f_1)$ IMAGE
G = 0
FREQUENCY $f=n_1f_1+n_2f_2$
DIFFRACTION ORDERS $G=n_1+n_2$
$-(2f_1-f_2)$
$-f_1$
$-f_2$
$-(2f_2-f_1)$
IMAGES
G = -1

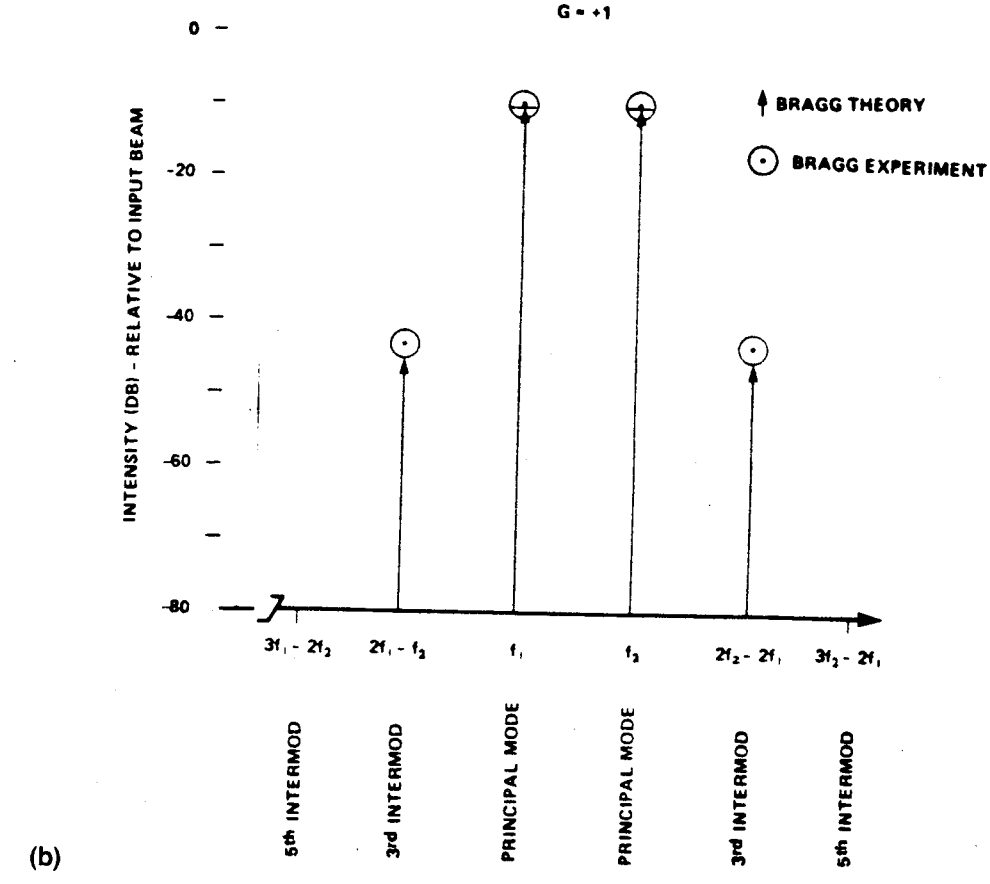
G = +1
0
-20
-40
-60
-80
INTENSITY (DB) - RELATIVE TO INPUT BEAM
BRAGG THEORY
BRAGG EXPERIMENT
$3f_1-2f_2$
$2f_1-f_2$
f_1
f_2
$2f_2-2f_1$
$3f_2-2f_1$
5th INTERMOD
3rd INTERMOD
PRINCIPAL MODE
PRINCIPAL MODE
3rd INTERMOD
5th INTERMOD

(b)

Figure 3-3 Incident angle versus acoustic frequency characteristics of anisotropic Bragg diffraction.

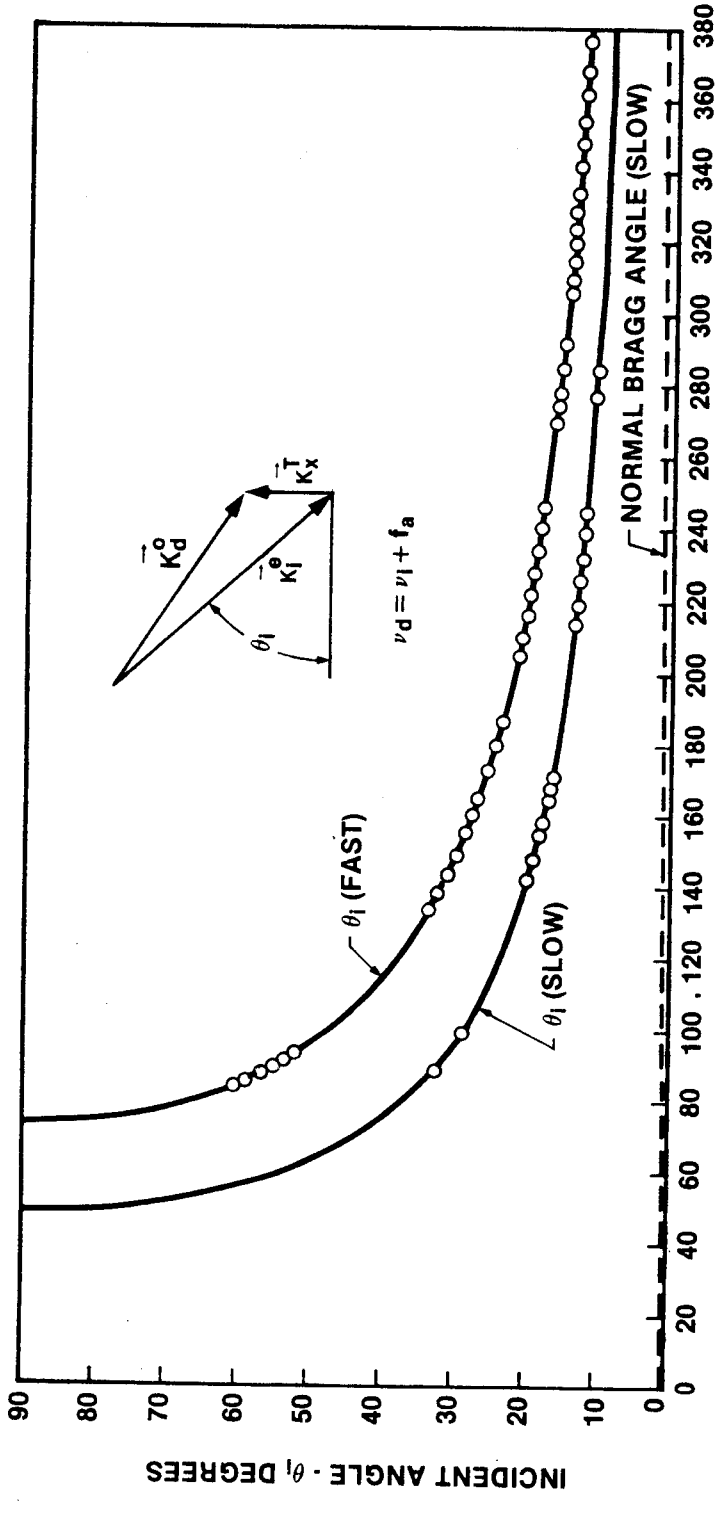
INCIDENT ANGLE - θ_i DEGREES
0
10
20
30
40
50
60
70
80
90
ACOUSTIC FREQUENCY - f_a MHz
0
20
40
60
80
100
120
140
160
180
200
220
240
260
280
300
320
340
360
380
NORMAL BRAGG ANGLE (SLOW)
θ_i (FAST)
θ_i (SLOW)
$\vec{K}_d^o$
$\vec{K}_i^e$
$\vec{K}_x$
θ_i
$\nu_d = \nu_i + f_a$

Figure 3-4 Collinear acousto-optic tunable filter.

Figure 3-5 Non-collinear acousto-optic tunable filter.

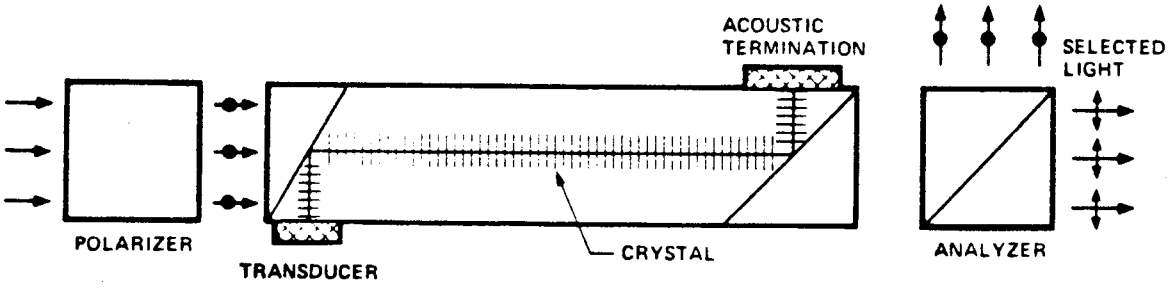
ACOUSTIC
TERMINATION
SELECTED
LIGHT
POLARIZER
TRANSDUCER
CRYSTAL
ANALYZER

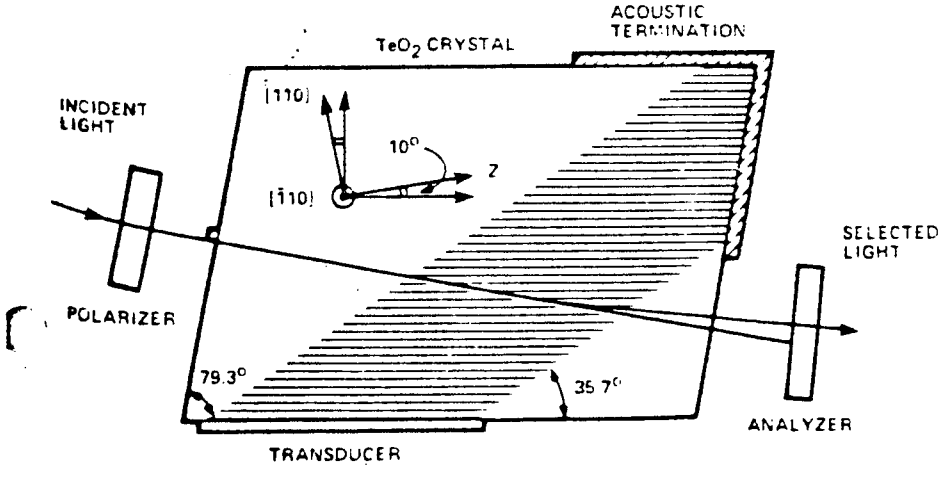
ACOUSTIC
TERMINATION
TeO_2 CRYSTAL
INCIDENT
LIGHT
[110]
10°
Z
[$\bar{1}$10]
SELECTED
LIGHT
POLARIZER
79.3°
35 7°
ANALYZER
TRANSDUCER

Figure 3-6 Image plane color filtering.

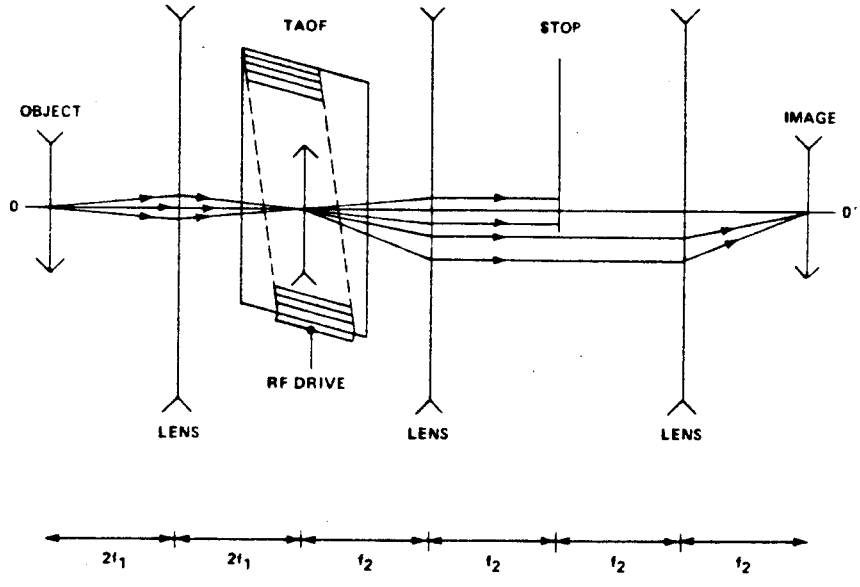
TAOF
STOP
OBJECT
IMAGE
O
O'
RF DRIVE
LENS
LENS
LENS
$2f_1$
$2f_1$
f_2
f_2
f_2
f_2

Figure 3-7 Image plane noise filtering.

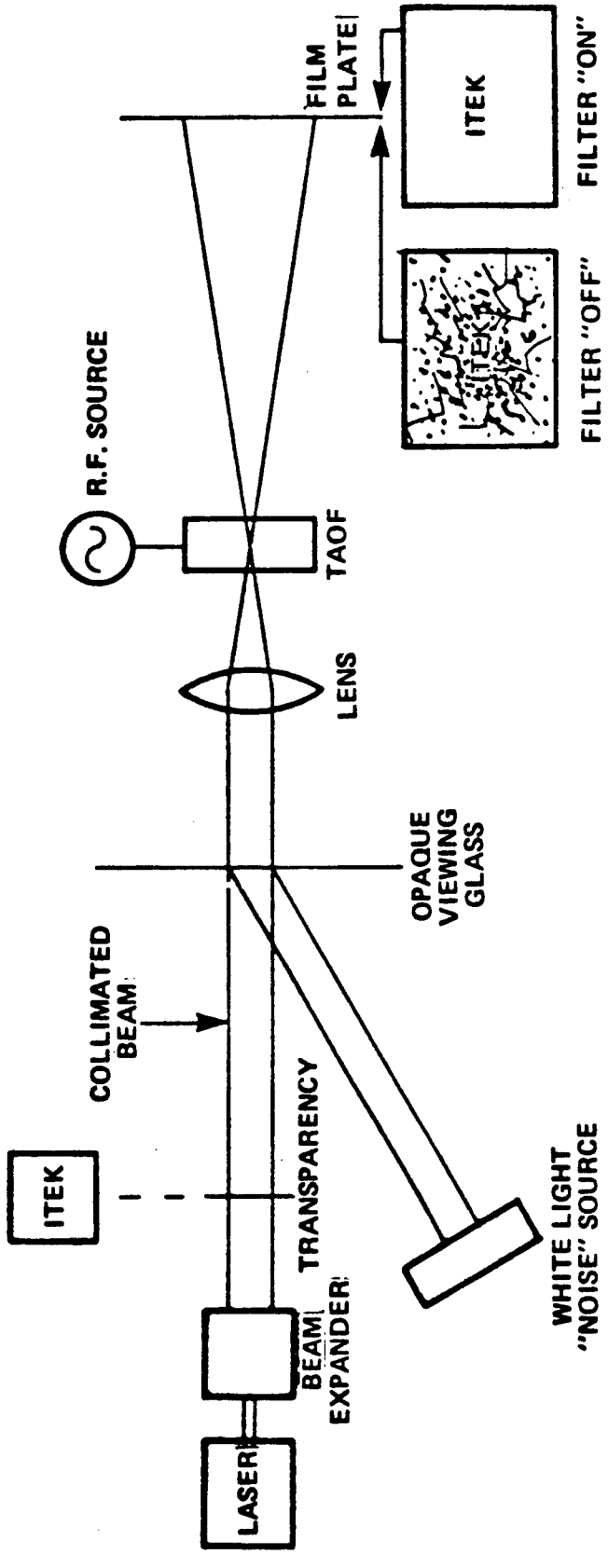
LASER
BEAM EXPANDER
ITEK
TRANSPARENCY
COLLIMATED BEAM
OPAQUE VIEWING GLASS
LENS
TAOF
R.F. SOURCE
FILM PLATE
ITEK
FILTER "ON"
ITEK
FILTER "OFF"
WHITE LIGHT "NOISE" SOURCE

Figure 3-8 Acousto-optical Tunable Filter (AOTF).

(a) Multiple transducer AOTF.

The spectral tuning range can be increased by using multiple transducers with different central frequencies and partially overlapping bandwidth.

(b) AOTF spectral tuning range using 2 transducers.

The "x"s are measured tuning frequencies.

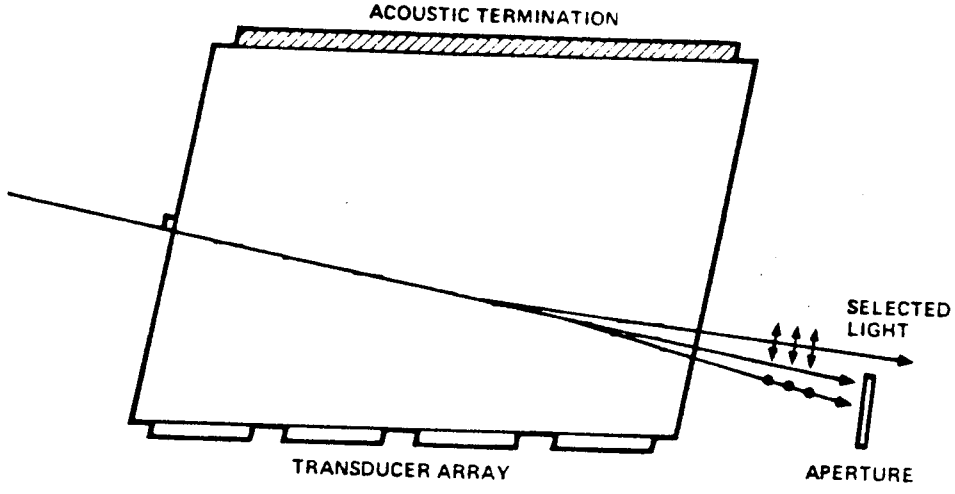
ACOUSTIC TERMINATION
SELECTED LIGHT
TRANSDUCER ARRAY
APERTURE

(a)

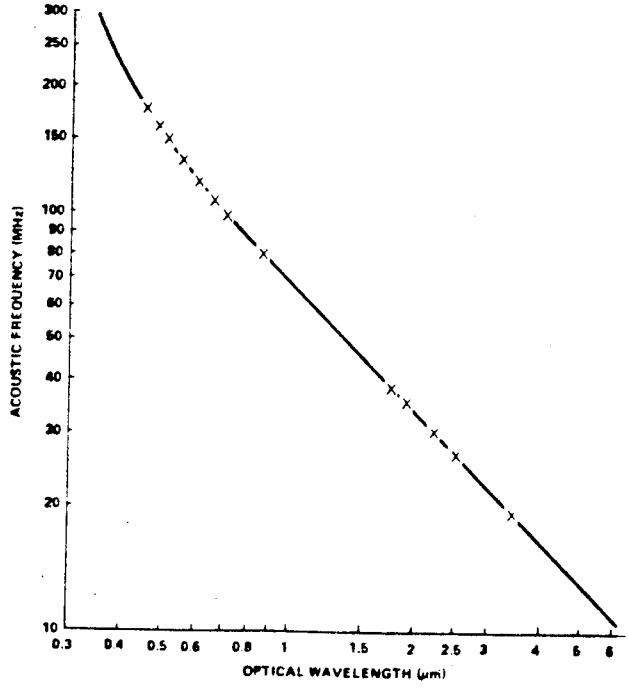
ACOUSTIC FREQUENCY (MHz)
300
250
200
150
100
90
80
70
60
50
40
30
20
10
0.3
0.4
0.5
0.6
0.8
1
1.5
2
2.5
3
4
5
6
OPTICAL WAVELENGTH (μm)

(b)

Figure 3-9 Bulk and integrated optic AO spectrum analyzer.

The rf signals enter the amplification and filtering circuits. The output electrical signals drive the acoustic transducer to produce surface acoustic waves. The collimated and truncated laser beam enters the acoustic field and is diffracted. The positions and intensities of diffracted beams correspond to those of the rf components.

(a) Bulk AO spectrum analyzer.

(b) Integrated-optical AO spectrum analyzer.

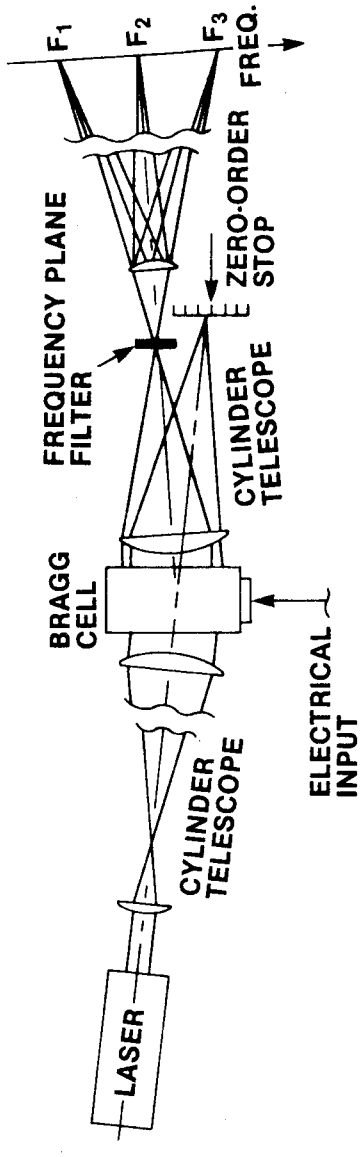
F1
F2
F3
FREQ.
FREQUENCY PLANE
ZERO-ORDER STOP
FREQUENCY FILTER
CYLINDER TELESCOPE
BRAGG CELL
ELECTRICAL INPUT
CYLINDER TELESCOPE
LASER

(a)

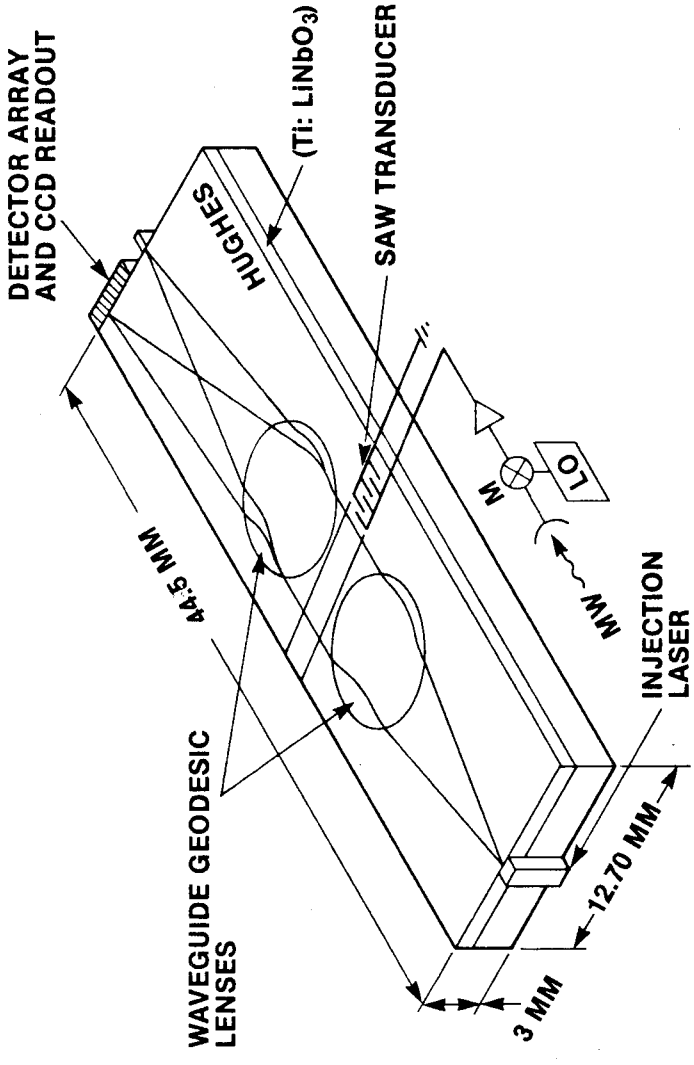
DETECTOR ARRAY AND CCD READOUT
HUGHES
(Ti: LiNbO3)
SAW TRANSDUCER
M
LO
MM
INJECTION LASER
44.5 MM
WAVEGUIDE GEODESIC LENSES
12.70 MM
3 MM

(b)

Figure 3-10 High-bandwidth transducer configurations.

Two examples of many possible configurations of high bandwidth SAW transducers.

(a) Tilted acoustic transducers.

(b) Phased array acoustic transducers.

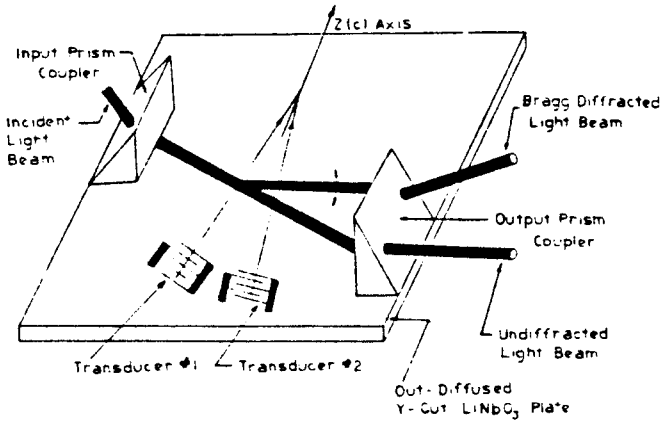
Z (c) Axis
Input Prism Coupler
Incident Light Beam
Bragg Diffracted Light Beam
Output Prism Coupler
Undiffracted Light Beam
Transducer #1
Transducer #2
Out-Diffused Y-Cut $LiNbO_3$ Plate

(a)

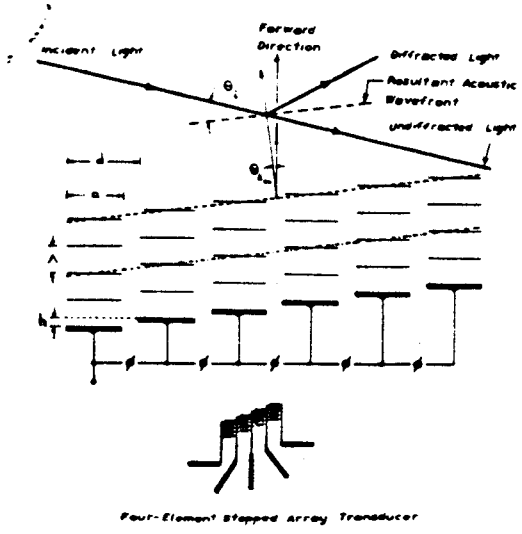
Incident Light
Forward Direction
Diffracted Light
Resultant Acoustic Wavefront
Undiffracted Light
Four-Element Stepped Array Transducer

(b)

Figure 3-11 Block diagram of an acousto-optic radio frequency receiver.

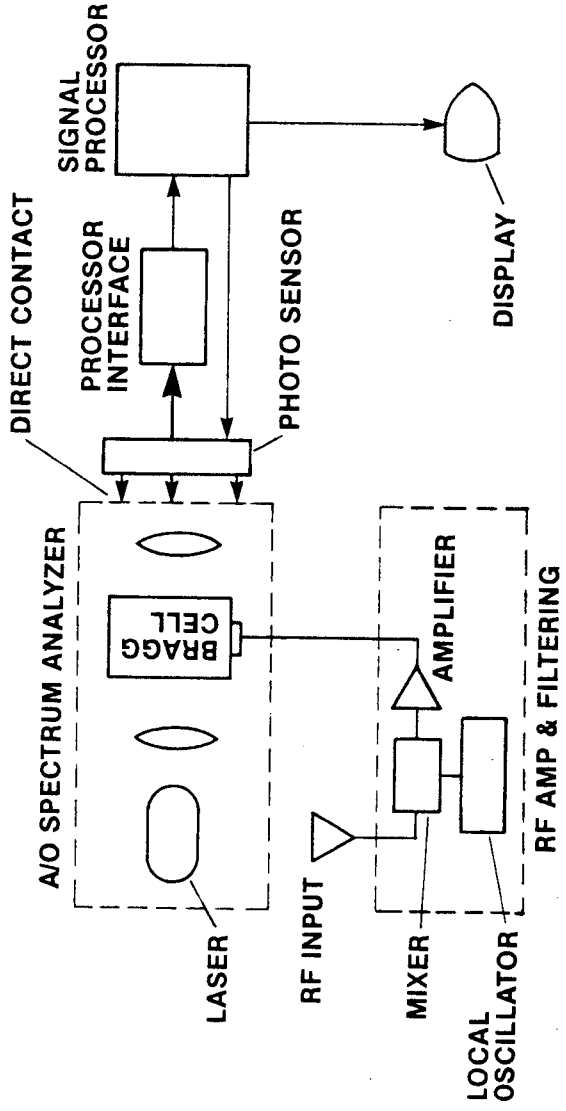
SIGNAL PROCESSOR
DISPLAY
PROCESSOR INTERFACE
PHOTO SENSOR
DIRECT CONTACT
A/O SPECTRUM ANALYZER
BRAGG CELL
AMPLIFIER
RF AMP & FILTERING
LASER
RF INPUT
MIXER
LOCAL OSCILLATOR

Figure 3-12 Time integrating correlator.

An AO time-integrating correlator using hybrid optical waveguide structure.

Figure 3-13 Two beam time integrating correlator.

An AO two beam time integrating correlator using two acoustic sources and one optical source.

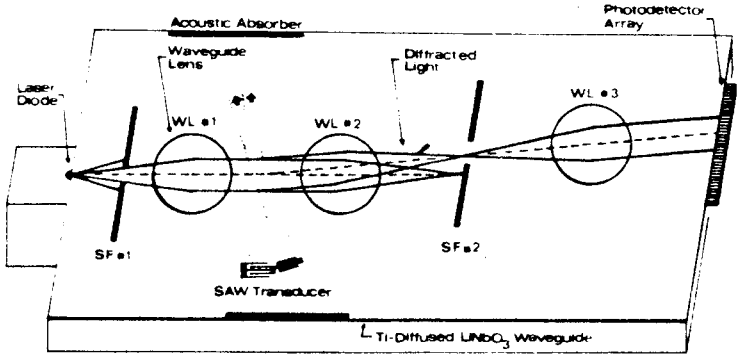
Acoustic Absorber
Photodetector Array
Waveguide Lens
Diffracted Light
Laser Diode
WL #1
WL #2
WL #3
SF #1
SF #2
SAW Transducer
Ti-Diffused $LiNbO_3$ Waveguide

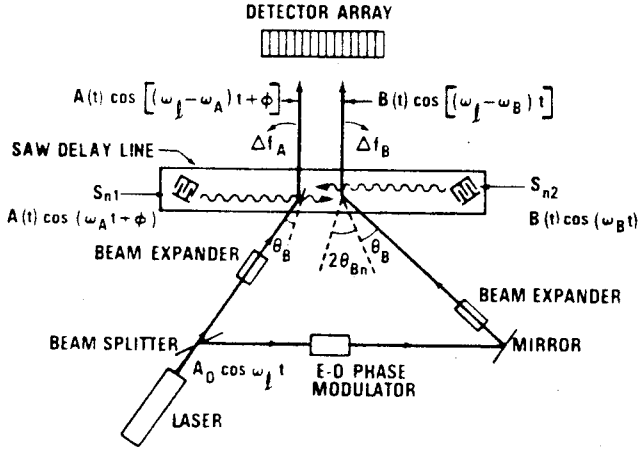
DETECTOR ARRAY
$A(t)\cos[(\omega_l-\omega_A)t+\phi]$
$B(t)\cos[(\omega_l-\omega_B)t]$
Δf_A
Δf_B
SAW DELAY LINE
S_{n1}
S_{n2}
$A(t)\cos(\omega_A t+\phi)$
$B(t)\cos(\omega_B t)$
BEAM EXPANDER
θ_B
$2\theta_{Bn}$
θ_B
BEAM EXPANDER
BEAM SPLITTER
MIRROR
$A_0\cos\omega_l t$
E-O PHASE MODULATOR
LASER

Figure 3-14 The AO triple product correlator using the AO effect. SCN_i's are laser sources and A(t) and B(t) are the two acoustic sources.

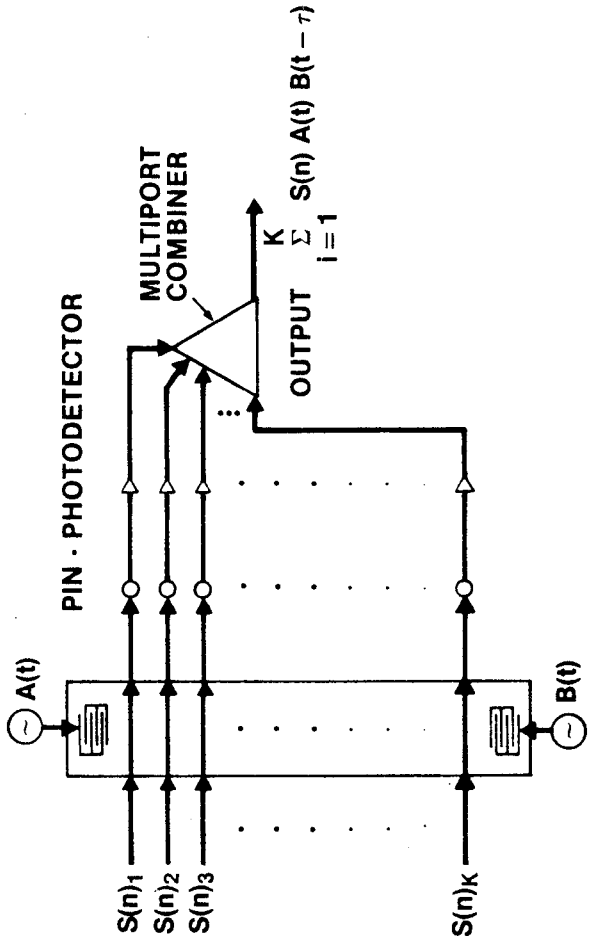
A(t)
PIN - PHOTODETECTOR
MULTIPORT COMBINER
OUTPUT
K
Σ S(n) A(t) B(t − τ)
i=1
B(t)
S(n)1
S(n)2
S(n)3
S(n)K

Figure 3-15 Symmetric Bragg diffraction using symmetric optical incidences.

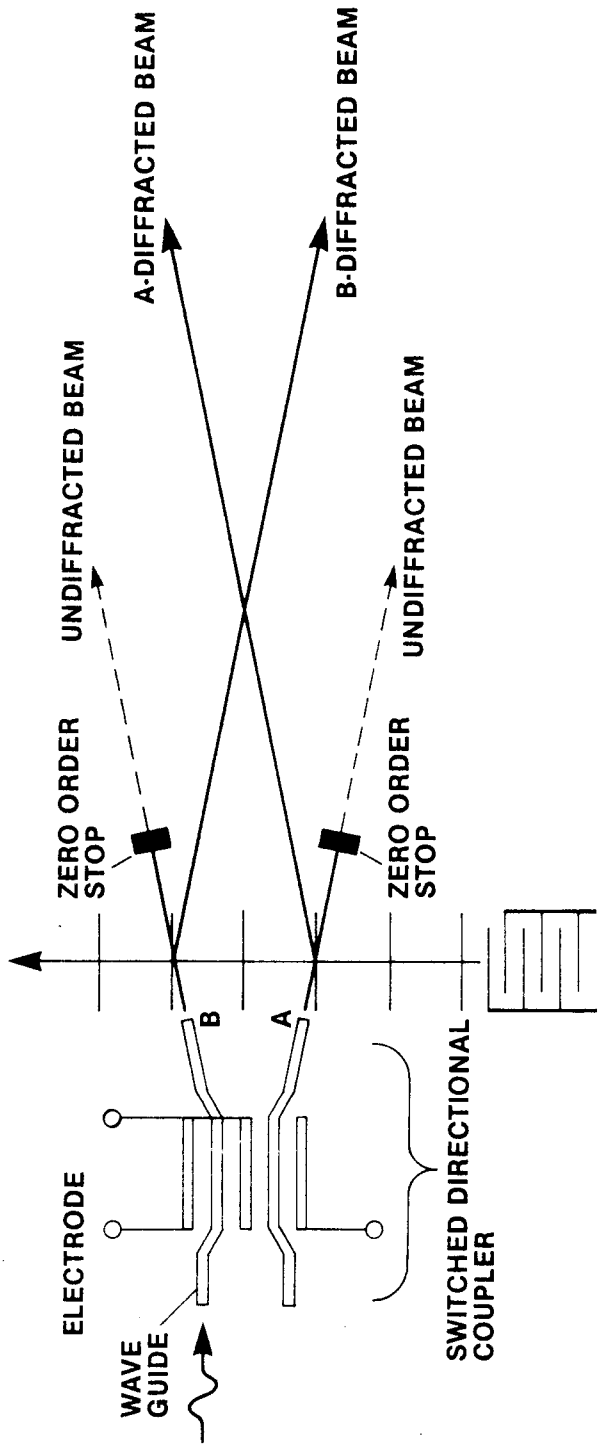
A-DIFFRACTED BEAM
B-DIFFRACTED BEAM
UNDIFFRACTED BEAM
UNDIFFRACTED BEAM
ZERO ORDER STOP
ZERO ORDER STOP
B
A
ELECTRODE
WAVE GUIDE
SWITCHED DIRECTIONAL COUPLER

Figure 3-16 Symmetric Bragg diffraction using symmetric acoustic transducers.

(a) Symmetric tilted transducers.

(b) Symmetric phased-array transducers.

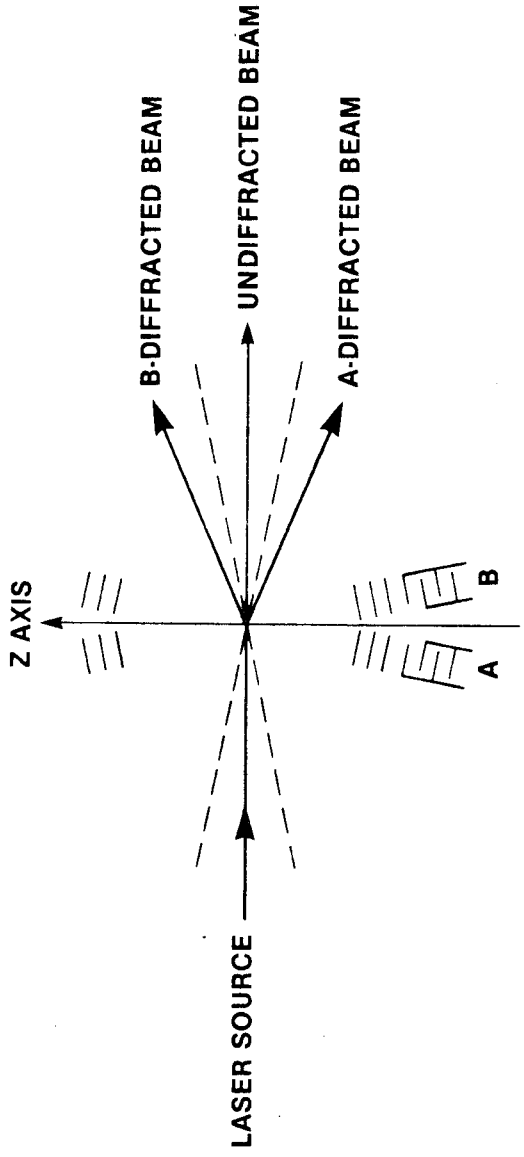
B-DIFFRACTED BEAM
UNDIFFRACTED BEAM
A-DIFFRACTED BEAM
Z AXIS
B
A
LASER SOURCE

(a)

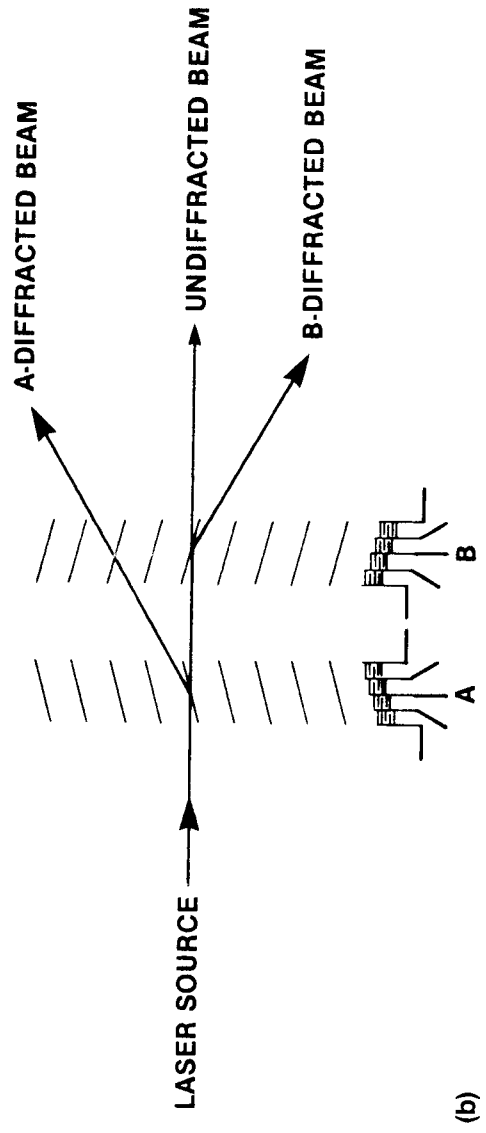
A-DIFFRACTED BEAM
UNDIFFRACTED BEAM
B-DIFFRACTED BEAM
LASER SOURCE
A
B

(b)

Figure 3-17 AO network switcher.

(a) One input to 100 (multiple) output switch.

(b) M input to N output switch.

(c) Hybridation of multiple substrates to achieve a large number of available input channels.

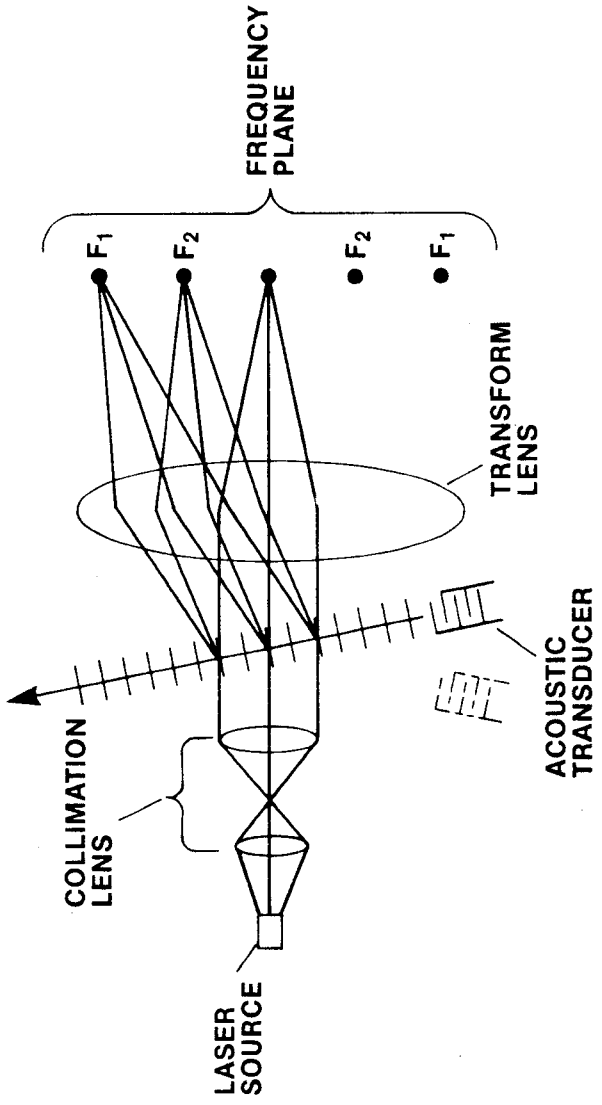
FREQUENCY PLANE
F1
F2
F2
F1
TRANSFORM LENS
ACOUSTIC TRANSDUCER
COLLIMATION LENS
LASER SOURCE

(a)

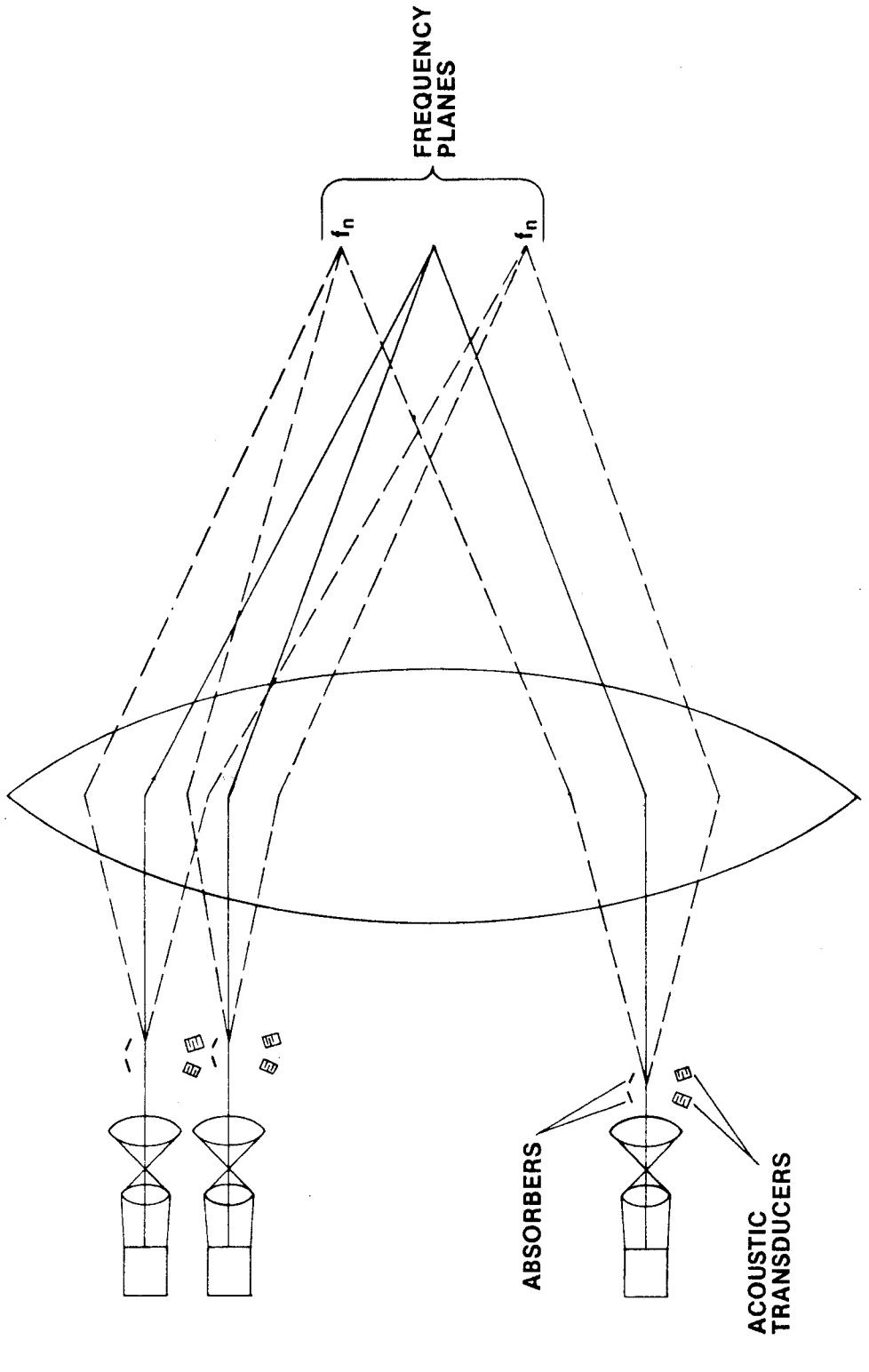

(b)

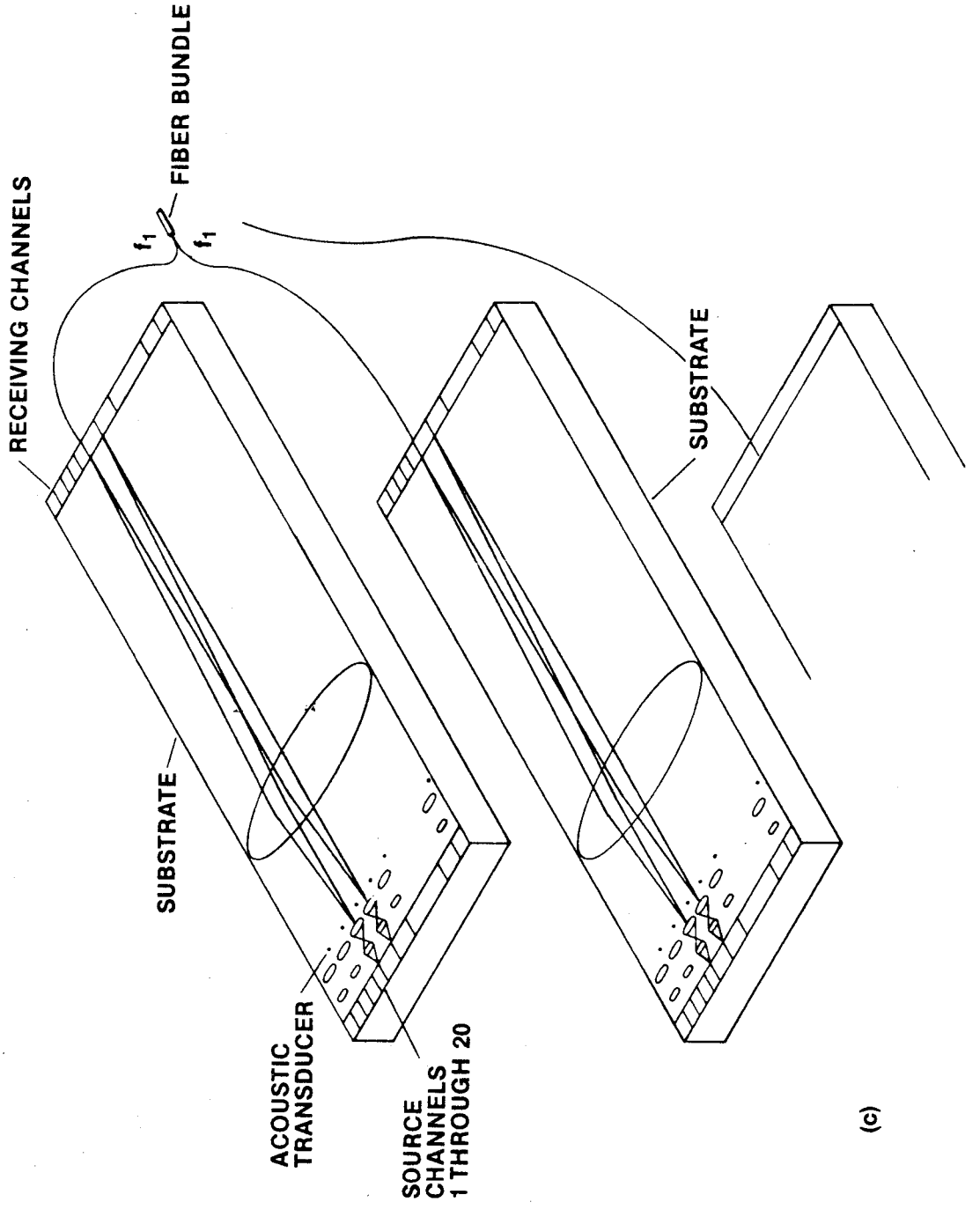
RECEIVING CHANNELS
FIBER BUNDLE
f_1
f_1
SUBSTRATE
SUBSTRATE
ACOUSTIC TRANSDUCER
SOURCE CHANNELS 1 THROUGH 20
(c)

Figure 3-18 Selection of oscillators for the AO network switch control.

(a) 100 oscillators are needed for an "N to 100" switching capacity.

(b) Only half as many oscillators are needed when symmetric transducers are employed.

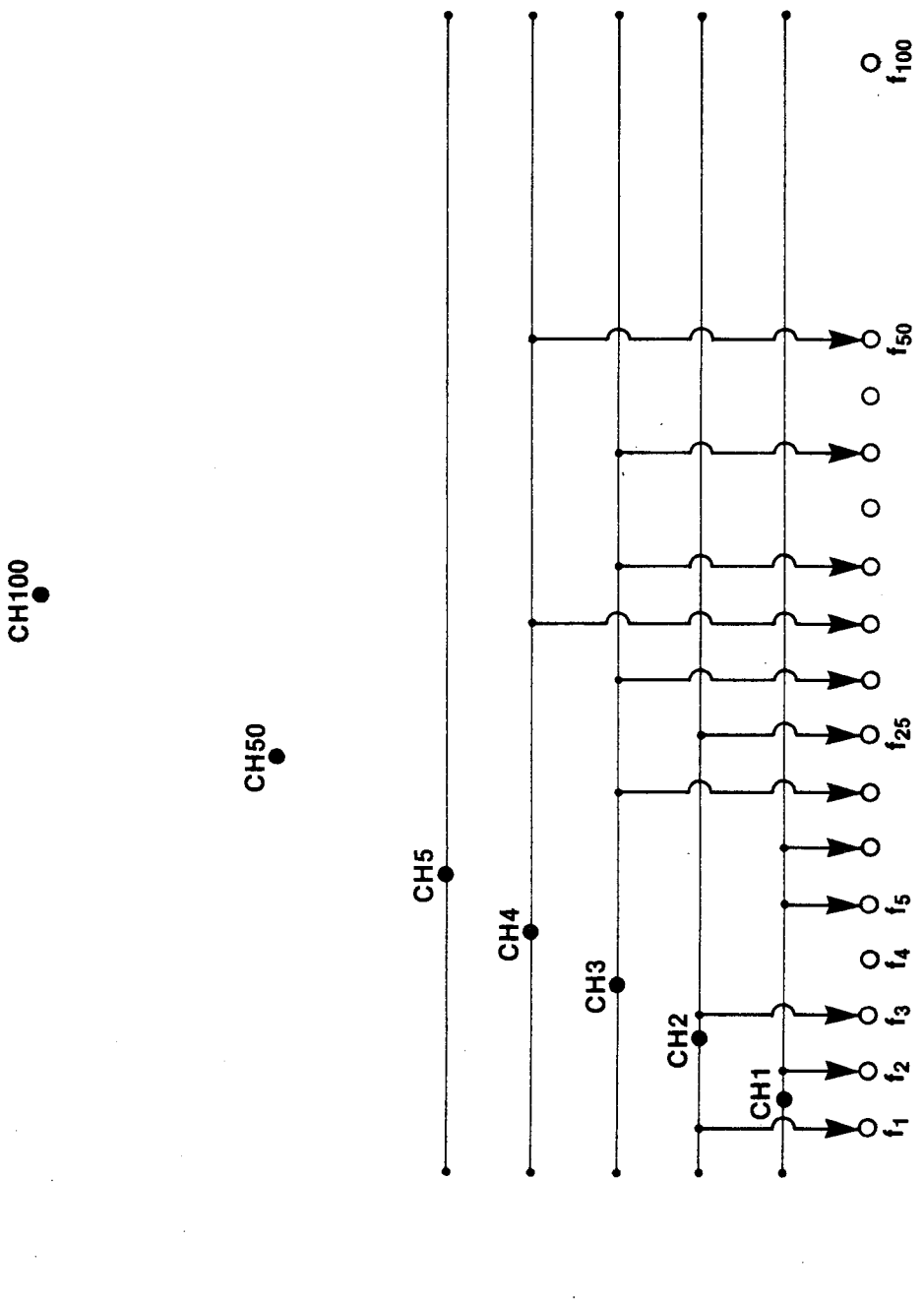

(a)

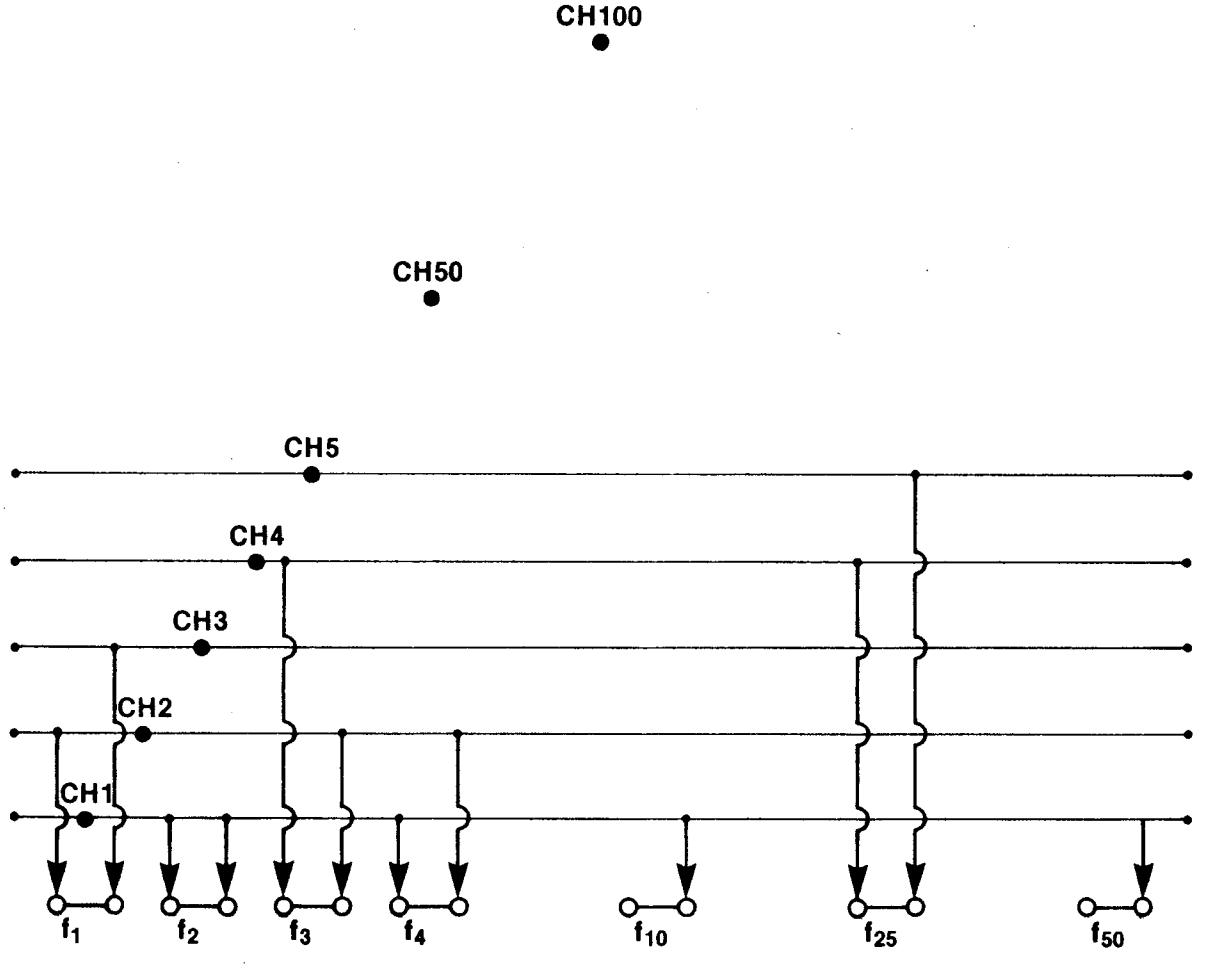

(b)

Figure 3-19 Sidelobe level and the mainlobe halfwidth versus the truncation ratio T.

(a) The ratio of the sidelobe intensity to the mainlobe intensity in dB versus the truncation ratio T at 0 dB and 12 dB acoustic losses.

(b) Relative mainlobe halfwidth versus truncation ration T at 0 dB and 12 dB acoustic losses. We can see that the sidelobe level can be depressed at the cost of increased mainlobe width.

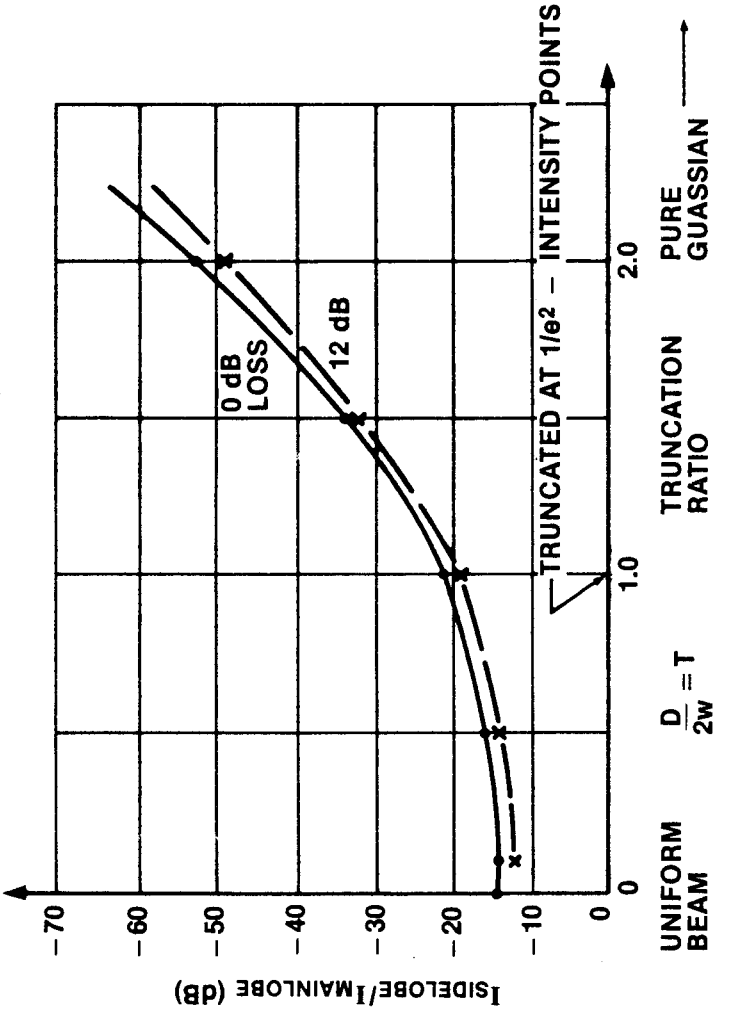

3-19 (a) SIDELOBE LEVEL IN dB VERSUS THE TRUNCATION RATIO T.

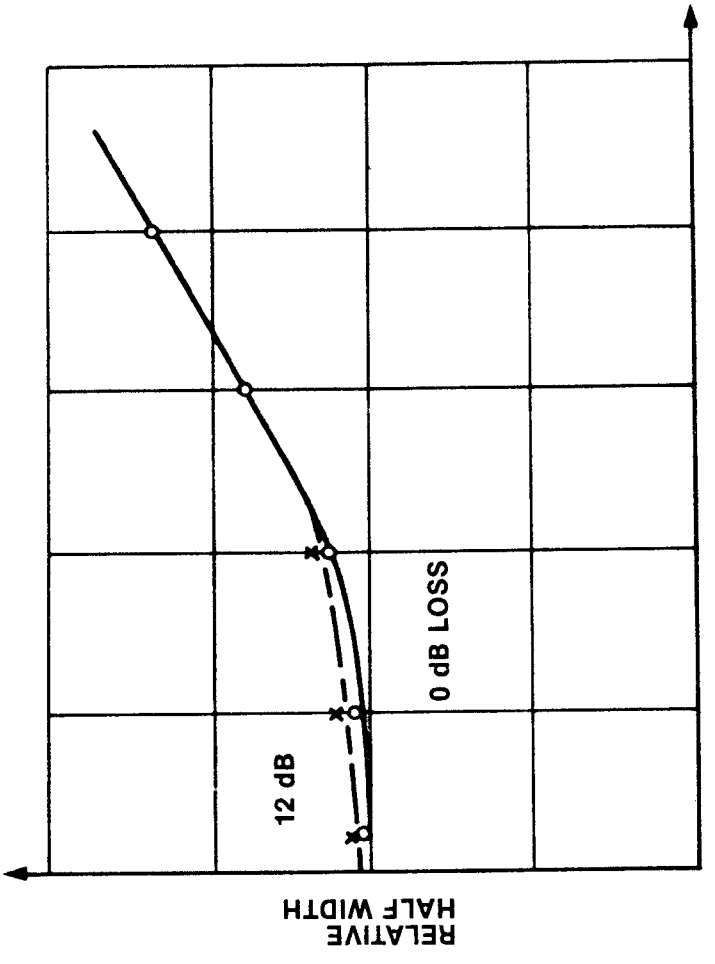

3-19 (b) RELATIVE MAINLOBE HALFWIDTH
VERSUS TRUNCATION RATIO T.

Figure 3-20 Intermodulation of multiple Bragg diffractions.
(a) Intermodulation modes.
(b) Intensity of the intermodulation modes.

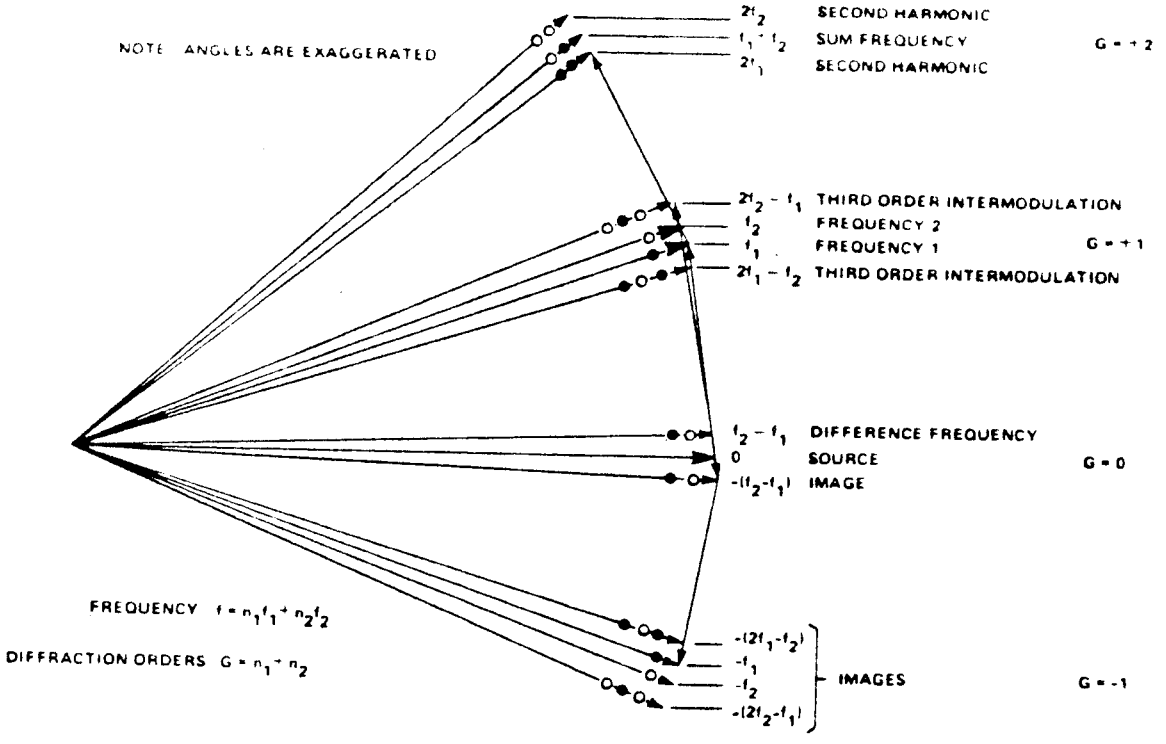
NOTE ANGLES ARE EXAGGERATED
$2f_2$ SECOND HARMONIC
$f_1 + f_2$ SUM FREQUENCY
$2f_1$ SECOND HARMONIC
G = +2
$2f_2 - f_1$ THIRD ORDER INTERMODULATION
f_2 FREQUENCY 2
f_1 FREQUENCY 1
$2f_1 - f_2$ THIRD ORDER INTERMODULATION
G = +1
$f_2 - f_1$ DIFFERENCE FREQUENCY
0 SOURCE
$-(f_2-f_1)$ IMAGE
G = 0
FREQUENCY $f = n_1 f_1 + n_2 f_2$
DIFFRACTION ORDERS $G = n_1 + n_2$
$-(2f_1-f_2)$
$-f_1$
$-f_2$
$-(2f_2-f_1)$
IMAGES
G = -1

(a)

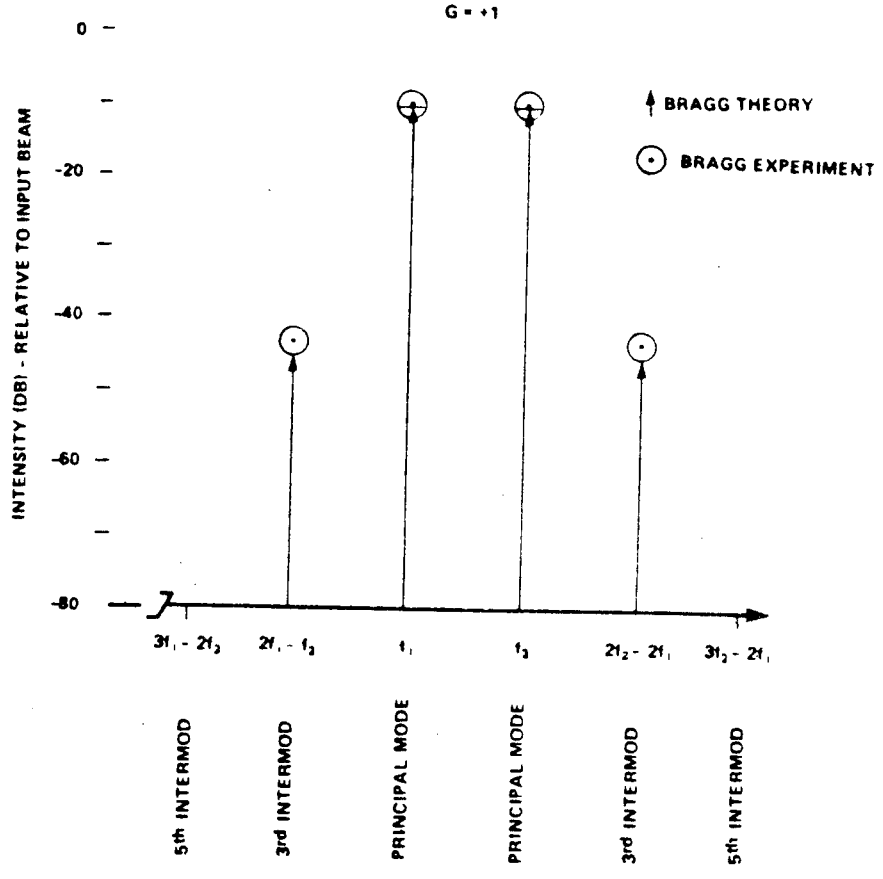
G = +1
0
-20
-40
-60
-80
INTENSITY (DB) - RELATIVE TO INPUT BEAM
BRAGG THEORY
BRAGG EXPERIMENT
$3f_1 - 2f_2$
$2f_1 - f_2$
f_1
f_2
$2f_2 - 2f_1$
$3f_2 - 2f_1$
5th INTERMOD
3rd INTERMOD
PRINCIPAL MODE
PRINCIPAL MODE
3rd INTERMOD
5th INTERMOD

(b)

REFERENCE LISTING - CHAPTER 3

1. A.H. Rosenthal, "Color Control by Ultrasonic Wave Gratings," J. of the Optical Society of America, Vol. 45, No. 9, p. 751, September 1955.
2. R.W. Dixon, "Acoustic Diffraction of Light in Anisotropic Media," IEEE J. of Quantum Electronics, Vol. QE-3, No. 2, p. 85, February 1967.
3. S.E. Harris, R.W. Wallace, "Acousto-Optic Tunable Filter," J. of the Optical Society of America, Vol. 59, No. 6, p. 744, June 1969.
4. I.C. Chang, "Noncollinear Acousto-Optic Filter with Large Angular Aperture," Applied Physics Letters, Vol. 25, No. 7, October 1974.
5. I.C. Chang, "Tunable Acousto-Optic Filters, an Overview," SPIE, Vol. 90, Acousto-Optics, 1976.
6. ITEK Technical Note, "Tunable Acousto-optic Filters," April 1979.
7. T. Yang, A. Watanabe, "Acoustooptic TeO_2 Tunable Filter Using Far-Off-Axis Anisotropic Bragg Diffraction," Applied Optics, Vol. 15, No. 9, p. 2250, September 1976.
8. H.J. Babrov, M.M. Jacobs, "Acoustooptic Tunable Filter Performance in a Starring IR Sensor," Applied Optics, Vol. 18, No. 23, p. 3901, December 1979.
9. D.L. Hecht, "Broadband Acousto-Optic Spectrum Analysis," IEEE Ultrasonic Symposium Proceedings, 1973, p. 98, IEEE Cat. No. 73, CH0807 8SU.
10. B. Chen, T.R. Joseph, J.Y. Lee, T.R. Ranganath, "Integrated Optical Circuits for R.F. Spectrum Analysis," SPIE Proceedings, Vol. 218, p. 8, 1980.
11. C.S. Tsai, L.T. Nguyen, B. Kim, I.W. Yao, "Guided-Wave Acousto-Optic Signal Processors for Wideband Radar Systems," SPIE Proceedings, Vol. 128, p. 68, 1977.
12. D.B. Anderson, "Integrated Optical Spectrum Analyzer: An Imminent 'Chip'", IEEE Spectrum, p. 32, December 1978.
13. D. Mergerian, E.C. Malarkey, "Integrated Optical RF Spectrum Analyzer," Microwave Journal, International Edition, Vol. 23, No. 9, p. 37, September 1980.
14. C.S. Tsai, J.K. Wang, K.Y. Liao, "Acousto-Optic Time Integrating Correlators Using Integrated Optics Technology," SPIE, Vol. 128, Real Time Signal Processing II, 1979, p. 160.
15. N.J. Berg, M.W. Casseday, I.J. Abramovig, J.N. Lee, "Surface Wave Acousto-Optic Signal Processing: Potential and Limitations," SPIE, Vol. 218, p. 98, 1980.
16. D.L. Hecht, "Multifrequency Acoustooptic Diffraction," IEEE Transactions on Sonics and Ultrasonics, Vol. SU-24, No. 1, p. 7, January 1977.
17. "Surface Wave Filters, Design, Construction and Use," Herbert Matthews, Editor, John Wiley & Sons, 1977, Chapter 1, G.W. Farnell.
18. E.G.H. Lean, J.M. White, C.D.W. Wilkinson, "Thin Film Acoustooptic Devices," Proceedings of IEEE, Vol. 64, No. 5, p. 779, May 1976.

19. Naoya Uchida and Nobukazu Niizeki, "Acoustooptic Deflection Material and Techniques," Proceedings of the IEEE, Vol. 61, No. 8, p. 1073, August 1973.

20. Yoshiro Ohmachi, "Acousto-optical Light Diffraction in Thin Film," Journal of Applied Physics, Vol. 44, No. 9, p. 3928, September 1973.

21. I. Ury, S. Margalit, M. Yust, A. Yariv, "Monolithic Integration of Injection Laser and a Metal Semiconductor FET," Applied Physics Letters, Vol. 34, No. 7, p. 430, April 1979.

22. D. Wilt, N. Bar-Chaim, S. Margalit, I. Ury, M. Yust, A. Yariv, "Low Threshold Be Implanted (GaAl)As Laser on Semi-Insulating Substrate," IEEE, Journal of Quantum Electronics, QE-16, No. 4, p. 390, April 1980.

23. T. Fukuzawa, M. Nakamura, M. Hirao, T. Kuroda, J. Umeda, Topical Meeting on Integrated and Guided-Wave Optics (1980).

24. N. Bar-Chaim, M. Lanir, S. Margalit, I. Ury, D. Wilt, M. Yust, A. Yariv, "Be-Implanted [GaAl]As Stripe Geometry Lasers," Applied Physics Letters, Vol. 36, No. 4, p. 233, February 1980.

25. M. Yust, N. Bar-Chaim, S.H. Izadpanah, S. Margalit, I. Ury, D. Wilt, A. Yariv, "A Monolithically Integrated Optical Repeater," Applied Physics Letters, Vol. 35, No. 10, p. 795, November 1979.

CHAPTER 4

THE ELECTRO-OPTIC APPLICATIONS

4.1 Introduction

The electro-optic (EO) effect is a manifestation of the change of refractive index **n** in an acentric crystal induced by an applied electric field. At its linear region, it is usually called Pokels effect. The material response time of the index change corresponds to the electronic lattice relaxation time, which ranges between 10^{-13} to 10^{-14} sec. Thus, for practical applications, the material frequency response of the linear electro-optic effect needs hardly be considered. The magnitude of the index change per unit applied electric field depends on the material coefficient. $LiNbO_3$ has the highest electro-optic coefficient (25 times that of GaAs) among the most commonly used electro-optic crystals, such as $LiNbO_3$, $LiTaO_3$, GaAs, ZnO, etc. (Table 1).

The applications of electro-optic effect in the manipulation of light waves are generally in terms of introducing a phase change to the propagating light waves by the application of an electric field. The most often used generic E-O components are: switched directional couplers[1,2], branched guide interferometer modulators[3] and interdigitated phase grating[4]. All three types have *sub-nanosecond switching* time (limited by the RC time constant of the electrodes). The power requirement is mainly the capacitive displacement power needed. In general, approximately *0.1 mW/MHz* electrical power is required for complete switching or optimal modulation.

Very high speed switching and modulation can be achieved by using traveling wave operation[5,6], where the electrical driving signal is propagated through

the length of the electrodes in the manner of a traveling wave. The switching time is not limited by the RC time constant in this case. Bandwidths up to 15 GHz have been reported[7]. Velocity matching (synchronization) of the traveling microwave and the light wave can further increase the gate speed[8]. Pulses with pulse width shorter than 0.1 picosecond can be generated by this approach.

4.1.1 Switched Directional Couplers

Switched directional couplers use an electrical voltage applied to the electrodes adjacent to or on top of the coupled-mode parallel-guide directional couplers (see section 2.4), to introduce a phase mismatch to the propagating light waves. This electric-field-induced phase mismatch provides externally controllable switching of the light waves propagation between the two parallel waveguides.

Figure 4-1 shows a classical switched directional coupler scheme. The distance between and the interaction length of a pair of matched parallel guides are chosen such that a complete crossover of light from one guide to the other is achieved without an applied electric field. A phase mismatch $\Delta\beta$ produced by an applied electric field offsets the mode coupling between the two parallel guides. When an appropriate electric field is applied, the propagation of light can be switched from a complete crossover state to a straight through state. However, as is shown in Figure 4-1, the cross-over coupling at zero electric field is not complete. The reason for this is the device fabrication which is very difficult. The width, interaction length and spacing of the two parallel guides have to be extremely accurate.

Figure 4-2 shows an improved version of the switched directional couplers, which uses a stepped alternating phase mismatch[2]. The alternating phase

mismatch gives added dimension of freedom to compensate the mode coupling between the two parallel guides. The stringent geometrical requirements on fabrication are thus eased. Although the alternating phase device shown in Figure 4-2 has an identical waveguide structure as the device shown in Figure 4-1, the switching characteristics are superior.

4.1.2 Branched Guide Interferometer

This scheme uses a voltage applied to electrodes adjacent to the branches of a branched waveguide to electro-optically introduce a relative phase shift between the light beams propagating in the two arms of the branched guide[9]. The recombination of the arms results to optical interference and causes intensity modulation of the output beam. The voltage needed for the first extinction to occur depends on the EO interaction length and the material constants. For a 17 mm interaction length in $LiNbO_3$, 3 volts (1.2 volts) is needed for π radian phase shift of TM (TE) polarized light.

Figure 4-3 illustrates the waveguide structure and the intensity of the output beam versus the applied voltage. This structure is widely used in integrated optical logic circuits[10] and optical analog to digital conversion[11,12].

4.1.3 Interdigitated Phase Grating

A phase alternating electric field is applied to a ferro-electric thin film waveguide by applying a voltage to a pair of interdigitated grating electrodes. This periodic electric field results in a periodic index variation. The periodic index variation then causes the guided optical waves to experience an electro-

optical Bragg diffraction. Intensity modulation of the undiffracted and diffracted beams can be controlled by varying the amplitude of the applied voltage. Total diffraction can be achieved at approximately 10 volts.

The distinction between the AO Bragg diffraction described in Chapter 3 and the EO Bragg diffraction described here is that the spatial periodicity of the index variation in the AO Bragg diffraction can be varied within a certain bandwidth by varying the rf frequency applied to the acoustic transducer. In EO Bragg diffraction it is fixed by the interdigitated grating electrodes. Furthermore, the applied voltage in the EO case is DC, thus no multiple diffraction as that in the AO Bragg diffraction occurs. The EO Bragg diffraction is virtually a beam splitter rather than a beam scanner like the AO Bragg diffraction. The switching speed of the EO Bragg diffraction (~nsec) is several magnitudes faster than the AO Bragg diffraction (~μsec).

Figure 4-4 shows the structure and the diffracted/incident beam intensity ratio versus applied voltage of a $LiNb_xTa_{1-x}O_3$ on $LiTaO_3$ grating modulator[4].

4.1.4 Traveling-Wave Devices and Velocity Matched Gates

The device structure of the electro-optic traveling-wave devices (TVD) and velocity matched gates (VMG) are eventually similar to those lumped devices described previously (4.1.1 - 4.1.3). Except that the electrodes have to be very thick to minimize microwave loss. This imposes a serious fabrication difficulty, for (1) the electrode width has to be comparable to the optical waveguide width, which is in the order of a few micrometers, and (2), the lengths of the electrodes often are in the millimeter range.

In typical thin-film and photolithographic processing, we are usually dealing with films of a few hundred Angstroms thickness. A 2 μm thick high quality

metal film could take hours to deposit, and is too thick for etching of micron-size features. Devices have been successfully built nevertheless in research facilities[5,6,7].

4.2 Optical A/D Conversion (Conventional Application I)

4.2.1 Device Configuration

The periodic dependence of output intensity of a branched guide interferometer on the applied voltage can be used to perform analog to digital conversion of an electrical signal using light intensity as a coder.

An example of an E-O A/D converter[11,12] is illustrated in figure 4.5. The least significant bit has the longest EO interaction length since the output intensity variation is the most sensitive to the input voltage variation.

4.2.2 Performance

The performance limitation on the conversion rate and number of bits is governed by the RC time constant of the electrodes of the least significant bit (LSB). For example, with $LiNbO_3$, an electrode length (i.e., EO interaction length) of 3.4 cm at the LSB results in 26 pF capacitance, and is capable of 6 bit accuracy at 1G-sample/sec conversion rates. Increased electrode length would result in higher accuracy or more bits of resolution. However, the conversion rate would decrease. The electrical power requirement is also an important parameter. The power is directly proportional to the electrode capacitance and device bandwidth. Assuming a 300 MHz maximal signal frequency for example being converted at 1 GHz conversion rate and 6 bits accuracy, requires that the

device bandwidth be higher than the maximal signal frequency, say approximately 400 MHz. In this case, the device power dissipation would be 1.6 Watts.

The conversion rate and bits of accuracy can be greatly improved if a traveling-wave approach is employed. The power requirement can be decreased by improving the impedance of the device electrodes.

4.2.3 Systems Considerations

Other components which influence the total system performance is also limited by the photodetector and comparator bandwidths, and the sample and hold circuit. Silicon avalanche photodiodes have cutoff frequencies of approximately 1.5 GHz. Silicon PIN diodes could achieve switching time of tens of picosecond, depending on the active area of the device. GaAs based avalanche photodiodes have achieved 3 GHz speed. Silicon emitter-coupled logic comparators are limited in speed to about 500 MHz. However, GaAs comparators can operate at well over GHz rate.

A unique feature of the EO A/D converter is that the sample and hold circuit can be eliminated by using a mode-locked laser source. A mode-locked semiconductor laser (using external cavity) could provide 20 psec optical pulses for signal sampling. Faster sampling can potentially be achieved by using velocity matched gates. This is an important feature, because the sample and hold circuit is usually the limiting factor of conventional high speed solid state A/D devices. However, the recent development in strobe comparator technique could give aperture time as low as 10 psec, this development may put the benefit of the optical system in question.

Another advantage of the E-O A/D converters is the drastic reduction of the number of comparators needed. In conventional solid-state A/D devices, for an N-bit converter, 2^N-1 comparator are needed. In E-O A/D converters, it takes only N comparators. For a 6-bit device, this is a reduction from 63 comparators to 6. However, ways of effecting this reduction also exist in electrical high speed A/D conversion schemes.

My opinion is that unless the traveling wave approach is used in this type of optical A/D conversion methods to enable much higher conversion rate and a greater number of bits of accuracy, the benefits of an optical system is not significant.

4.3 Vector Subtraction (Conventional Application II)

4.3.1 Introduction

In situations where handling of massive amounts of data is encountered, it is desirable to be able to compress, to selectively store and process the incoming data. A data comparison technique, such as vector subtraction, where incoming data sets are sequentially compared to reference sets, could contribute significantly to the processing time and system economics.

A typical example is earth resource surveying, where extensive digital signal filtering is used. Incoming data from surveying sensors are compared to sets of signature references which indicate possibilities of the presence of resources, or the presence of an undesired signal environment such as clear sea water or an excessive cloud cover. Intelligent decisions need to be made up front to decrease unnecessary data storage and processing loads.

Another conceivable application is "computer vision," in computer aided manufacturing where the shape, position and orientation of objects on a conveyor belt is determined by a computer to assist manufacturing automation. Often, only the information pertaining to the outline of the object is necessary for such computer vision. This "outline" of the object can be conveniently indicated by a sudden change of optical intensity detected by optical scanners. A hardware sequential vector subtraction technique could significantly shorten the computing time, which is often important in the feedback-control functions of automated manufacturing.

4.3.2 Device Description

Two integrated optical devices which address vector subtraction techniques have been under development by Battelle Columbus Laboratories. The first uses a holographic formation technique[13], the other uses branched waveguide interferometry[14].

Holographic Formation

Figure 4-6 illustrates the holographic formation technique. A laser beam is end-fired or grating coupled into a film waveguide. A phase-grating beam splitter splits the laser beam into two branches. Data electrodes and reference electrodes are placed along one branch and phase-controlling electrodes are placed on the other. The voltage across the phase-controlling electrodes are first adjusted such that a null is formed at the intersecting region of the two beams. The reference set and the data set are then biased on the data electrodes. The level of the departure of incoming data sets from the reference sets

could be detected by the departure from null of their hologram formation with the phase controlled beam.

The processing speed of the device is limited by the capacitance of the electrode structure. For one hundred data channels, 100 MHz rates are feasible. A higher processing speed could be achieved for less data channels.

Branched-Guide Interferometry

Figure 4-7 illustrates the concept of a 16 dimensional vector subtraction using branched-guide interferometry. The width of the optical beam at each branch starts at 800 μm and is further divided into sixteen 50 μm wide channels. A horn structure then reduces each channel to 7 μm width. The 32 electrode pads on each branch represent the input ports for the two 16 dimensional vectors. The result of the subtraction is represented by the light level at the recombination of the two arms. 10nsec response time and 8 levels of light intensity resolution are expected for this 16 channel device. The fabrication, however, is not trivial. The symmetry of the two arms and the uniformity of channel lengths are critical for successful performance.

Relevance to Tektronix

These devices could be useful to motion detection in video processing. However, in video motion detection, we compare the current frame information to the previous frame stored in memory. Reading the previous frame out from memory could be a cumbersome operation. However, the integrated optical vector subtraction technique used in conjunction with a high speed optical-disk mass memory could conceivably be a practical video processing hardware.

4.4 The Optical Logic Operations (Conventional Application III)

4.4.1 Introduction

Logic operations can be performed using integrated linear electro-optic devices[10], such as branched guide interferometers or switched directional couplers. The power dissipation is one to two orders of magnitudes lower than the optical logic operations using non-linear optical effects.

The propagation delay per gate is in the order of 20 psec to 30 psec. However, RC load of the data electrodes and the photodetector response time tend to be the limiting factors. The concept is thus more or less academic. However, if traveling-wave operation or velocity matched gates are used in integrated-optical logic circuits, the real speed advantage may be realizable. Propositions of optical logic devices have been made, but neither implementation nor experimentation have been published. The substrate area and the length in particular occupied by an optical logic gate are enormous when compared to either a silicon or a III-V semiconductor device. This factor may indicate that integrated optical logic gates will not be in direct competition with silicon devices. However, there will be specific applications where no large scale integration is needed.

4.4.2 Gate Descriptions

Figure 4-8 illustrates the concept of operation of some fundamental optical logic gates. In the branched-guide devices, voltage level V_o, which causes a π radian phase shift, represents logic level "1"; 0 volt represents logic level "0". In

switched directional coupler devices, the voltage level, which causes complete switching, represents logic level "1"; 0 volt represents logic level "0".

4.5 The Electro-Optic Network Cross-Point Switch, Application at Tektronix

4.5.1 Introduction

A network cross-point switch for optical digital video routing switch application, as mentioned in Chapter 3, could conceivably be implemented electro-optically.

The problem in the electro-optic cross-point switching network[17,18,19] is that the loss and crosstalk is proportional to the number of switching stages, which in turn is proportional to the number of ports. The resulting loss and crosstalk is so large for network sizes larger than 10x10 (Figure 4-9) that it is usually impractical to construct electro-optically.

Typically, a 2x2 electro-optic switching unit has a 0.8% (-21 dB) bending loss and 0.16% (-28 dB) crosstalk. For an NxN network switch, this means:

N	switching stages
N(N-1)/2	switch units
Nx0.8%	bending loss
Nx0.16%	cross talk

In our application, where N = 100, this corresponds to:

100	switching stages
4950	switch units
80%	bending loss
16%	cross talk

The total device size would be approximately 12 cm, since approximately 1.2 mm interaction length is typically needed for single stage electro-optic devices. An 80% crosstalk and a 16% bending loss is not an acceptable performance. A 12 cm device length is not feasible from the practical standpoint.

A scheme to improve these parameters significantly is presented in the following subsection.

4.5.2 An Alternative

The key innovation is a reduction of the number of switching stages while maintaining the network size.

Figure 4-10 shows a concept of composing a 100x100 network switch by using 20 units of 10x10 switches in 2 stages. The total number of switching stages would be reduced to 20 from 100, and the total number of switches would be reduced to 900 (45 on each module) from 4950. The total bending loss would be 16% or better, and the crosstalk would be 5%.

Number of modules	20
Number of switch/module	45
Total switching stage	20
Bending loss	16%
Cross talk	5%
Module length	~1.2 cm
Integration length	~2.4 cm

4.5.3 Advantages and Difficulties

The major advantage of this approach compared to the AO diffraction method (Chapter 3.5) is the simplicity of the voltage controlled switching versus the frequency controlled switching as in the AO approach (3.5). The ease of modular fabrication, the elimination of thin-film lenses (required in the AO approach), and the faster switching speed are additional attractions. The performance, in terms of noise and crosstalk is, however, inferior to the AO approach.

The coupling between the two 10x10 stages could provoke potentially series problems. If the two stages are fabricated on separate substrates and coupled together by optical fibers, a 15% to 50% loss could occur on each fiber-to-substrate joint. If the entire network is fabricated on one single substrate, the geometry and layout of the 100 channeled waveguides connecting the two 10x10 stages would not be trivial. However, based on the knowledge that two crossing optical beams do not affect each other before and after crossing (except a small perturbation), this device fabricated on one single substrate should achieve high performance. A vital experiment to perform for the feasibility of this device is the measurement of the crosstalk between two crossing channeled waveguides[20].

4.6 Opto-Electric Testing of Electronic Circuits (Application at Tektronix)

4.6.1 Introduction

The present semiconductor IC and PC Board testing hardware has a number of shortcomings:

1. Slow clocking rates (~20 MHz) caused by various reasons, most severe of all is the time dispersion of the massive coaxial cables and connectors.
2. Cumbersome and slow mechanical probes, such as mechanically manipulated pogo pins and probe tips.
3. Labor intensive, time consuming connecting schemes.

Except for IDD, most Tek products acquire and display signals, for testing or measurements. Signal acquisition has become more interactive, and now often requires stimulus injection and response inspection. In such interactive acquisitions probing hardware is the first functional element involved.

Leon Orchard of Laboratory Instrument Division is especially keen in removing the above-mentioned inflictions of the present IC and PC board probing methods. In our discussions, he has emphasized the importance of increasing the testing clock rate to above 200 MHz, and to computerize the testing. In this section we will propose a new circuit probing and testing concept (method) utilizing optical injection of stimuli and optical inspection of responses. This method provides high speed (>200 MHz), high isomorphism, isotropism and flexibility. It eliminates mechanical probes and error prone human operations, and makes true automation of probing and testing a possibility.

4.6.2 Optical Injection of the Electrical Stimuli and Optical Inspection of the Responses

The key of this proposed method is to keep the lengths of electrical transmission to a minimum. The electrical stimuli are converted to optical signals as close to the generation equipment as possible. The transmission to the circuit under test (CUT) is implemented optically. The optical stimuli are reconverted into electrical signals as close as possible to the CUT. The electrical responses of the CUT are converted to optical signals as close as possible to the CUT. The transmission to the diagnostic equipment is again implemented optically. The optical to electrical conversion of the response signals is performed as close as possible to the diagnostic equipment. This approach alleviates the pulse dispersion problem in coaxial electrical transmission of conventional probing and thus greatly enhances the bandwidth. The extraordinarily large bandwidth of the optical transmission and the electro-optical devices employed allows high speed dynamic tests or time-multiplexed lower speed dynamic tests.

The conversion from electrical stimuli to optical stimuli can be achieved either by directly modulating semiconductor laser sources, or by an electrically controlled optical switch/modulator external to a laser source. The conversion of the optical replica back to the electrical signals can be executed by photodiodes or photo-trigates.

The response signals can either be electrically inspected and diagnosed, or can be converted to optical signals either by directly driving a semiconductor laser array or by driving an integrated-optical phase modulator. The optical signal is then transmitted by optical fibers to the diagnostic equipment and then converted to electrical signals for inspection.

The programmable connection of the CUT to the stimulus and response opto-electric probes can either be achieved by using a programmable micro-

mechanical switch array, or a novel input/output dual-function opto-electric device proposed at the end of Section 4.6.3 (bi-directional stimulus-response probe).

4.6.3. Probe Descriptions

In this section, two approaches are described. The first approach employs a stimulus probe, a response probe and a micromechanical switch array to couple the two probes to the CUT. The second approach incorporates a novel dual-function optoelectric device to achieve bi-directionality.

Stimulus Probe

Figures 4-11 to 4-12 describe possible optical stimulus probes. A CW laser source (or multiple sources) is coupled into an optical fiber bundle. The optical fibers are coupled to an integrated array of guided wave optical switches (Fig. 4-11a) or modulators (Fig. 4-11b). Each element of the integrated guided-wave switch/modulator array is capable of impressing a pre-programmed electrical test stimulus onto the light beam traveling through the switch or modulator. The modulated optical beams are then coupled into an optical fiber bundle again, and transmitted to the immediate vicinity of the CUT. The ends of the fibers are aligned by a honeycomb and coupled to an integrated array of opto-electric converters (Figure 4-12a, b). The modulated optical beams are then converted to electric signals, buffered and injected into the stimulus ports of the CUT.

Response Probe

Figure 4-13 describes an optical response probe. The response signals from the CUT can be buffered and used to drive an optical interferometer array (Fig. 4-13). The principal C.W. laser beams brought to the interferometer array by the optical fiber bundle are imprinted with the response signals from the CUT by the interferometric modulator. Another fiber-bundle then carries the response signals in optical form, to the immediate vicinity of the diagnostic equipment. The fiber ends are aligned and coupled to an integrated array of conventional photodiodes. The photodiode array converts the optical response signals to electrical signals for inspection and analysis by the diagnostic equipment. Integrated electro-optic devices other than the interferometric type can also be used.

The CUT-to-Probe Interface -- Micromechanical Switch Array

Tek Technology Group is currently developing a current controlled thermally actuated and a voltage controlled static-charge actuated programmable micromechanical switch[21] array. These types of switch arrays can be utilized to configure and reconfigure the connection between CUT and the optical probes. Figure 4-14 is a conceptual description of the proposed coupling scheme between the CUT, the probes, the stimulus generation equipment and the response diagnostic equipment.

The switching time of the micromechanical switching devices (μsec-msec), however, is not fast enough for bi-directional bus applications, in which a specific pin of the CUT may be a stimulus pin at one clock cycle and a response pin at the next clock cycle.

Bidirectional Stimulus/Response Probe

The key to this approach is that each channel can be programmed to be a stimulus (input) or response (output) channel without any mechanical switching. The channel configuration can be altered at very high speeds. This capability is provided by an opto-electric circuitry[22] employing a photodiode and an optical gate (Figure 4-15). When the optical beam addressing the photo-diode D_o is "high" (low), the electrical pulse at the test point would be low (high), thus reconstructing the inverse of the electrical stimulus. This electrical stimulus bit stream is injected into the CUT and at the same time amplified by a buffer G_3 to drive another integrated-optical modulator array (Figure 4-16), which allows optical transmission to the diagnostic equipment.

When the tri-state pin of G_1 is addressed (when the optical beam stimulating G_1 is "high"), the test point is effectively disconnected from the input. The response of the CUT is then amplified by buffer G_3, which drives the integrated-optical modulator (Figure 4-17) and converts the electrical signals to optical pulses to be transmitted to the diagnostic equipment by optical fibers.

Figure 4-16 shows the integrated-optical phase modulator array addressing the opto-electric circuitry shown in Figure 4-15. A pair of independently programmable phase modulators **a** and **b** address the photo-diode D_o and the optically triggered gate G_o correspondingly. This unit forms the stimulus injection side of one dual-function stimulus/response channel.

Figure 4-17 shows the integrated-optical phase modulator array driven by the output V_{G3n} of buffer G_{3n}. This phase modulator array converts the electrical response signals from the CUT or the electrical stimuli injected into CUT to optical signals again and optically transmits them to the immediate vicinity of the diagnostic equipment.

Figure 4-18 shows the conceptual system schematics. The interfacing of the integrated-optical modulator array to the integrated opto-electric conversion circuitry can be achieved by using a multilayer ceramic hybrid approach as suggested in figure 4-19. The connection of the probe test points to the CUT can be achieved by integrating currently available high speed IC connector techniques into the multilayer hybrid package.

4.6.4 Other Optical Approaches in IC Testing

Texas Instruments, Lincoln Laboratories and IBM are pursuing processed IC wafer testing using E-beam. Siemens, Philips and some universities are developing processed IC wafer and die testing using SEM (voltage contrast measurements). Hughes Aircraft Company is developing a photoexcitation scheme using a galvanometer scanned HeNe laser.

Our approach is far superior to the above-mentioned methods for application of field testing ICs on PC boards. For example, a high vacuum chamber is needed for the E-beam and SEM schemes, and two (x,y) slow galvanometers are needed in the Hughes approach. Hughes approach is not capable of high speed dynamic testing.

Distinct advantages can also be rationalized in our approach for testing individual ICs whether packaged or on the wafer. Parallelism, dynamic capability and very high speed nature are the most important features. System cost is also conceivably lower.

4.6.5 Other Advantages

1) Leapfrogging competitions.

2) The "fixture" nature of this subsystem requires no alteration to the conventional ICs and PC board circuitries.

3) All electrical testing algorithms can be adapted.

4) A direct modular adaptation of this probe into the present testing hardware is conceivable, while the ultimate fit is aimed toward the testing equipment of the future.

5) The capability of the technology leaves a very large margin for future speed improvements above 200 MHz. The integrated-optical components have potential for 20 GHz operation when traveling microwave or velocity matching schemes are employed.

6) The method is capable of parallel processing while providing nigh bandwidth for possible time-multiplexed serial processing.

7) This system provides high speed bidirectional, programmable input/output channel configuration which is also applicable to conventional electrical probing.

8) An unspecified number of channels for different testing purposes and environments is possible.

9) The concept can be applied to almost all testing purposes and environments by slight modifications.

10) Ample patent protection.

4.6.6 Major Technological Difficulties

Electro-optic coefficients differ along different crystal axes of the electro-optic material. The effect of an applied electric field on propagating light is thus polarization dependent. Optical fibers (especially multimode fibers) tend to depolarize the originally polarized guided light. Single mode fibers with good mode purity do not depolarize, but do rotate the polarization of the guided light instead. The resultant polarization of the light at the fiber-to-modulator junction depends on the length of the fiber. For practical purposes, the resultant polarization direction is unknown. However, considerable efforts have been reported on ribbon fibers consisting of asymmetric single mode fibers maintaining the polarization of the guided light. It is also possible to design a diffraction grating on the integrated optic waveguide to repolarize the incident light. Successful efforts in fabricating polarization independent integrated-optic devices and active polarization switchers are also taking place at Bell Laboratories[23] and Japanese groups. Their results have been presented at the 3rd International Conference on Integrated Optics and Optical Fiber Communication during April 1981 in San Francisco[24,25,26].

The coupling of light from optical fibers to the integrated-optic device is another problem. No extensive development effort has been devoted to this particular problem to date yet. Integrated-optic research groups, on the other hand, have not been motivated to solve peripheral problems of this nature. A loss of anywhere between 15% to 50% can be expected at each fiber-substrate junction. Fortunately in this application, the power loss is not detrimental. We could compensate the loss by increasing the power output of the external laser source, or by using multiple sources.

4.7 Data Transmission

Optical wavelength division multiplexing technique could drastically increase the information carrying capacity of fiber optical transmission systems without resorting to higher frequency components. Narrow-band (wavelength) optical filters with minimum dispersion are essential for this technique. Integrated optical filters fabricated on $LiNbO_3$ offer superior performance than geometric filters.

Polarization independent filter having a 5 Å bandwidth, 75% peak filter efficiency was successfully demonstrated recently[23] (Figure 4-20). At such narrow bandwidth, a large number of wavelength channels can be multiplexed, and the information carrying capacity of the fiber-optical transmission system economically utilized. Several (N) of the filters like the one shown in Figure 4-20 can be fabricated in sequence on one single substrate, forming an N channel filter. When applied to the fiber-optical transmission system as a multiplexer/demultiplexer, the information carrying capacity is increased by N-fold. Another interesting application of this type of filters is in very high frequency systems where narrow spectral width source is required. An inexpensive LED could be used in conjunction with the filter instead of resolving to more expensive lasers.

A less ambitious multiplexing scheme could be implemented by TE/TM mode multiplexing, using integrated-optical mode splitter[27]. However, this scheme provides only a two fold increase on the information carrying capacity.

Increasing the frequency capability of the optical transmission system (frequency division multiplexing) is though less desirable, nevertheless another possibility. Traveling wave integrated-optical modulators and gates[5,27] are capable of generating optical pulses up to tens of GHz frequency from a CW laser source.

However, this approach is much more costly since high frequency electrical components and photodetectors are required.

Table 4-1

SOME TYPICAL ELECTRO-OPTIC COEFFICIENTS AND REFRACTIVE INDEX CHANGES FOR APPLIED FIELDS OF 10,000 V/cm

Relative Dielectric Constant	*Material*	$\lambda[\mu m]$	n'	$r'[10^{-12}m/V]$	Δn $E=10^4 V/cm$	$V_{\lambda/2}[V]$
28	$LiNbO_3$	0.6328	$2.203(n_\varepsilon)$	$30(r_{33})$	$1.6\text{x}10^{-4}$	1,970
12.3	GaAs	0.9	3.6(n)	$1.2(r_{14})$	$2.8\text{x}10^{-5}$	16,100
8.2	ZnO	0.6328	$2.015(n_\varepsilon)$	$2.6(r_{33})$	$1.1\text{x}10^{-5}$	29,700

Values of n, r, and ε from I.P. Kaminow, "Linear Electrooptical Materials," CRC Handbook of Lasers, Ed. R.J. Pressley, p. 447.

Figure 4-1 A conventional switched directional coupler and its output light intensity versus applied voltage. The waveguide geometry is not optimized for mode coupling due to the stringent geometric requirements.

Figure 4-2 Alternating phase mismatch switched directional coupler and its output light intensity versus applied voltage.

The waveguide geometry is identical to that of the device shown in Figure 4-1. However, the switching characteristics are far superior.

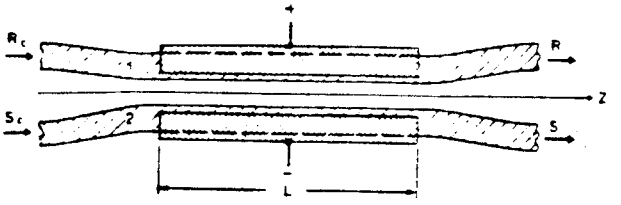
+
R_c
R
Z
S_c
S
-
L

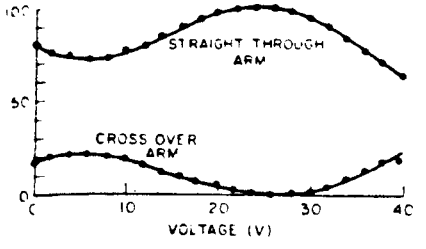
100
50
0
STRAIGHT THROUGH ARM
CROSS OVER ARM
0
10
20
30
40
VOLTAGE (V)

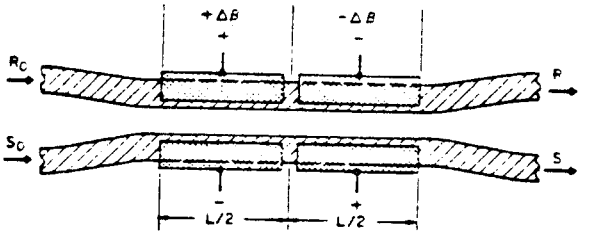
+ΔB
+
-ΔB
-
R_c
R
S_c
S
-
L/2
+
L/2

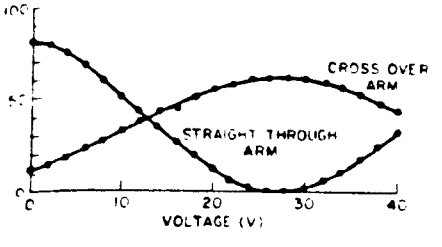
100
50
0
CROSS OVER ARM
STRAIGHT THROUGH ARM
0
10
20
30
40
VOLTAGE (V)

Figure 4-3 Branched guide interferometric phase modulator and its output light intensity versus applied voltage for TE (upper picture) and TM (lower picture) polarized light.

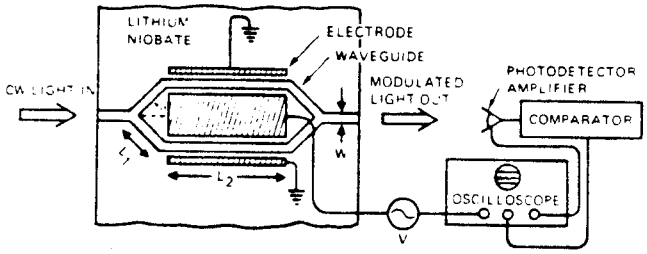
LITHIUM NIOBATE
ELECTRODE
WAVEGUIDE
CW LIGHT IN
MODULATED LIGHT OUT
PHOTODETECTOR AMPLIFIER
COMPARATOR
W
L_2
OSCILLOSCOPE
V

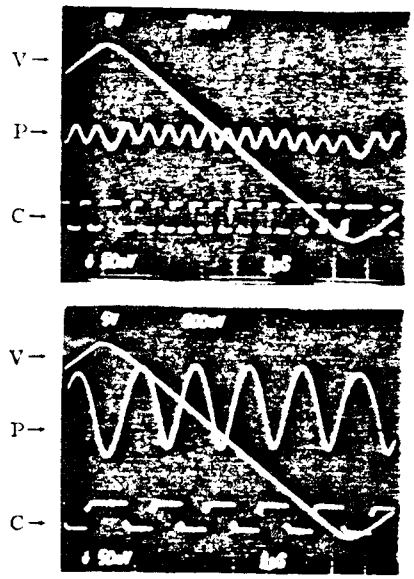
V
P
C
V
P
C

Figure 4-4 Interdigitated Phase Grating (EO Bragg Diffraction) and the diffracted light intensity versus applied voltage.

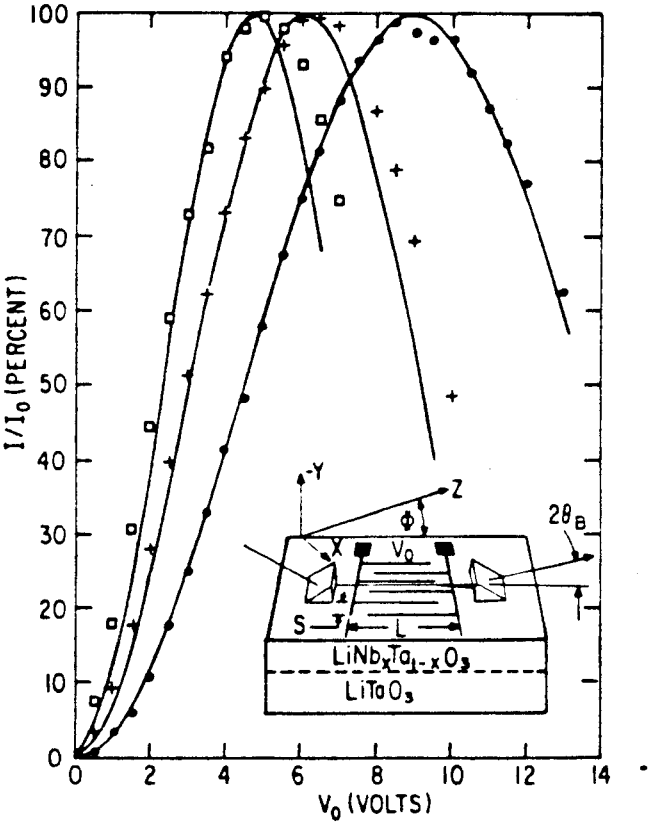
100
90
80
70
60
50
40
30
20
10
0
I/I0 (PERCENT)
0
2
4
6
8
10
12
14
V0 (VOLTS)
-Y
Z
Φ
2θB
X
V0
S
L
LiNbxTa1-xO3
LiTaO3

Figure 4-5 Integrated optical analog to digital converter using branched guide interferometric phase modulators. The least significant bit has the longest electrodes and thus the longest interaction length.

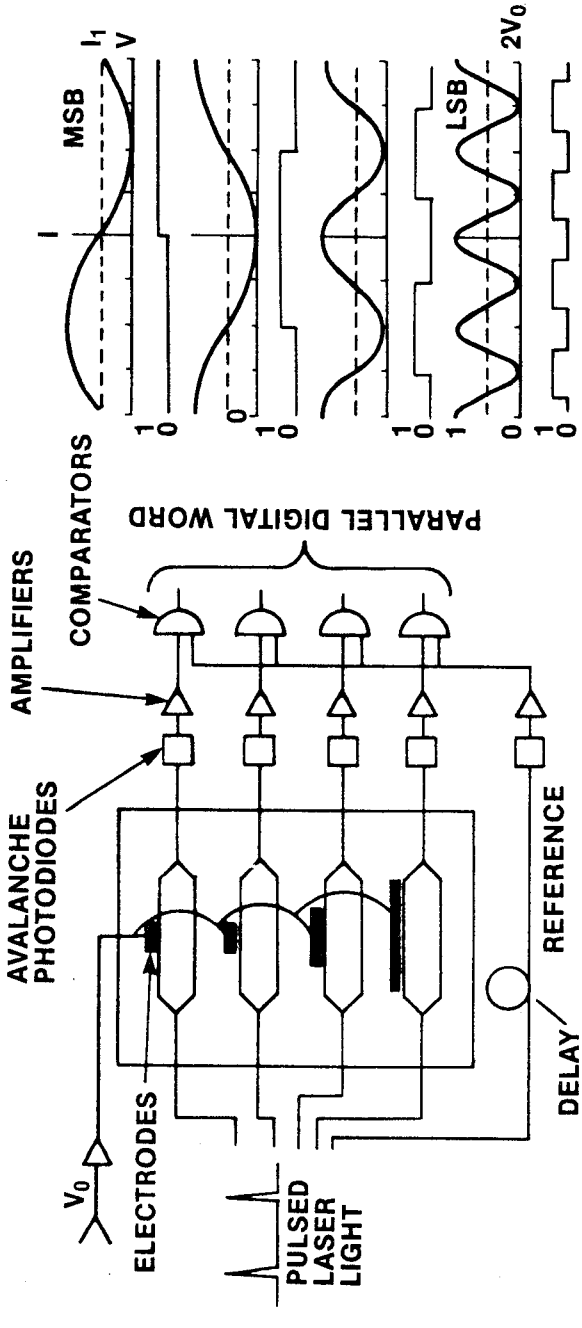
I
MSB
I_1
V
LSB
$2V_0$
1
0
PARALLEL DIGITAL WORD
COMPARATORS
AMPLIFIERS
AVALANCHE PHOTODIODES
ELECTRODES
V_0
PULSED LASER LIGHT
DELAY
REFERENCE

Figure 4-6 Integrated Optical Digital Comparator.

A phase grating beam splitter splits the laser beam into two branches. Data electrodes and reference electrodes are placed along one branch, and phase-controlling electrodes on the other. The voltage across the phase-controlling electrodes are first adjusted such that a null is formed at the intersecting region of the two beams. The reference set and the reverse of the data set are then biased on the reference and data electrodes. The level of the departure of the data set from the reference set could be detected by the departure from null of their hologram formation with the phase controlled beam.

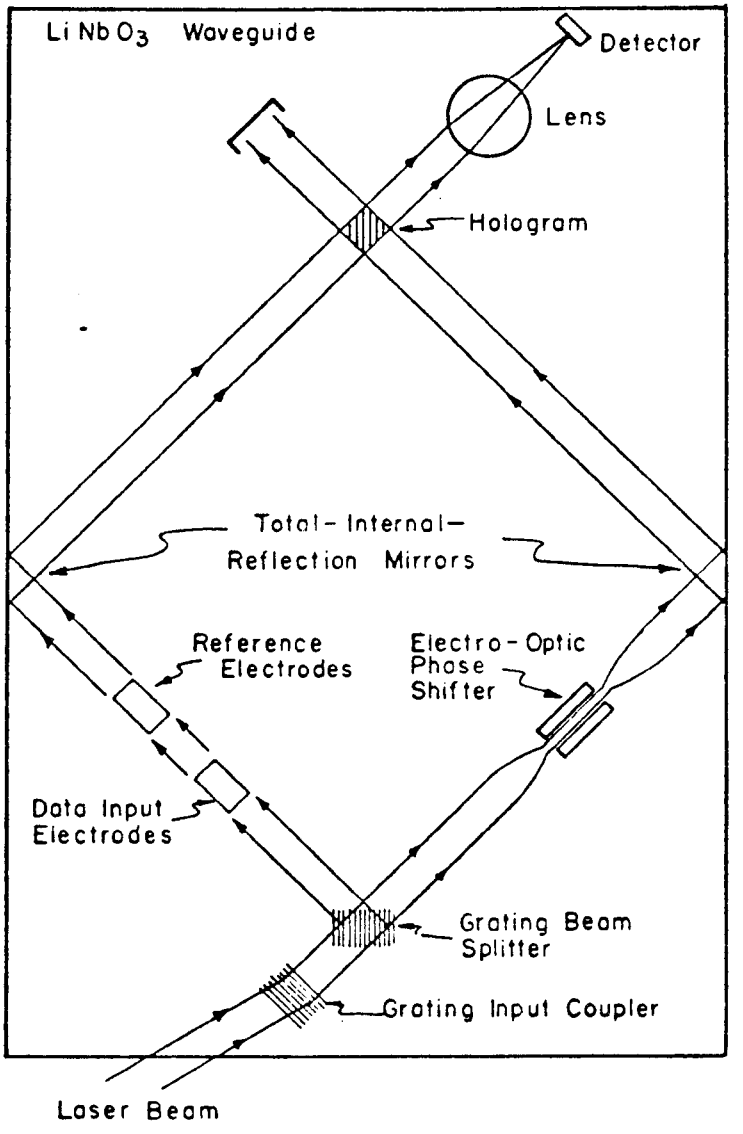
Li Nb O3 Waveguide
Detector
Lens
Hologram
Total-Internal-Reflection Mirrors
Reference Electrodes
Electro-Optic Phase Shifter
Data Input Electrodes
Grating Beam Splitter
Grating Input Coupler
Laser Beam

Figure 4-7 Integrated optical digital data comparator using multi-channel branched guide interferometric phase modulators. The 16 pairs of electrodes on each arm correspond to a 16 dimensional vector (or a 16 bit word). The resultant output light level directly corresponds to the result of the subtraction of the two vectors.

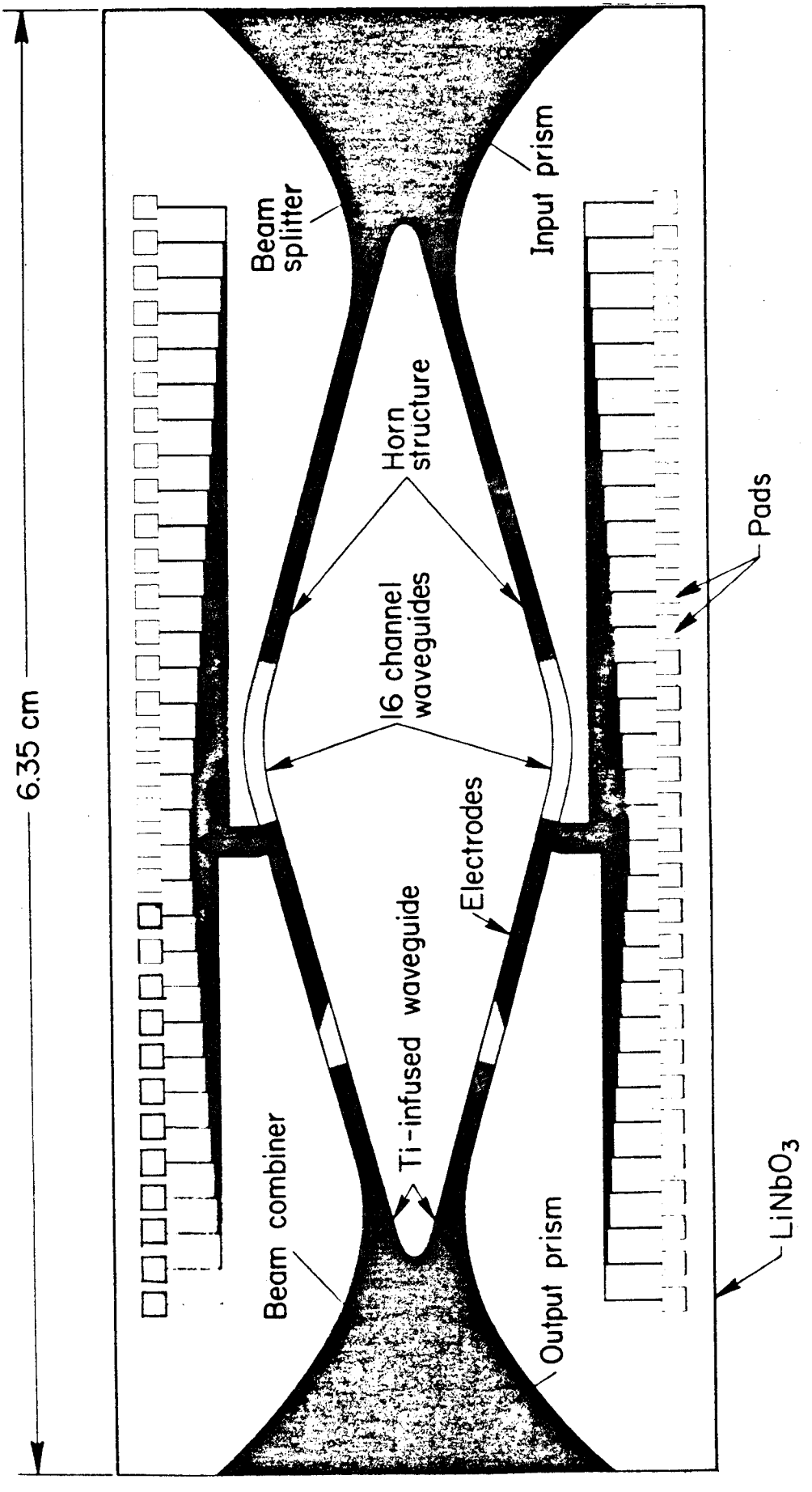
6.35 cm
Beam splitter
Input prism
Horn structure
16 channel waveguides
Pads
Electrodes
Ti-infused waveguide
Beam combiner
Output prism
$LiNbO_3$

Figure 4-8 Some basic integrated-optical logic gates:

(a) Schematic diagram of an optical logic device.

(b) Interferometric phase modulator used as a three input exclusive or gate.

(c) Switched directional coupler used as an exclusive or gate.

(d) Some basic fundamental logic gates.

(e) A device for computing the carry bit k_n and sum bit C_n for the nth stage of a binary adder.

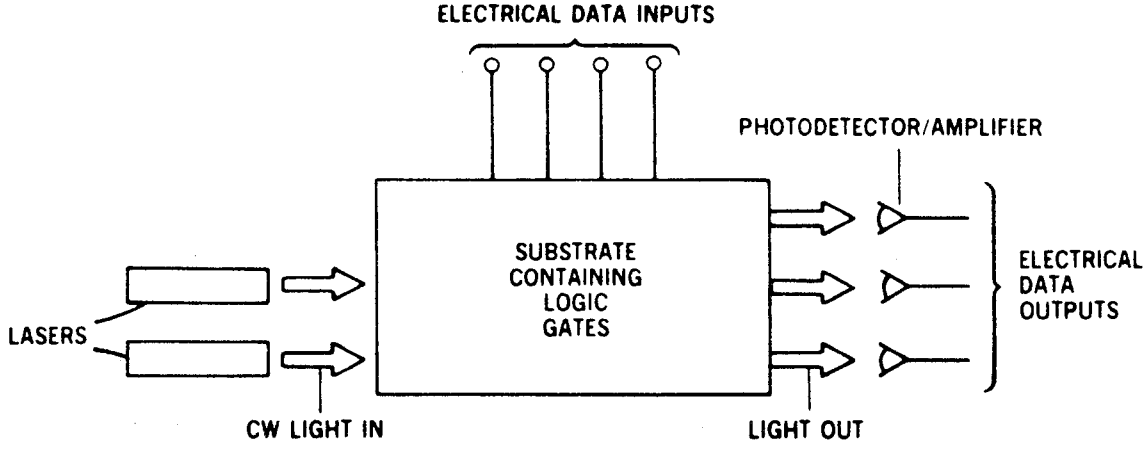
ELECTRICAL DATA INPUTS
PHOTODETECTOR/AMPLIFIER
SUBSTRATE CONTAINING LOGIC GATES
ELECTRICAL DATA OUTPUTS
LASERS
CW LIGHT IN
LIGHT OUT

(a)

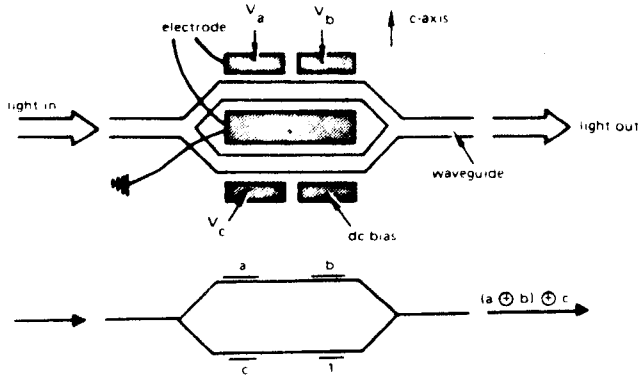
electrode
V_a
V_b
c-axis
light in
light out
waveguide
V_c
dc bias
a
b
c
1
(a ⊕ b) ⊕ c

(b)

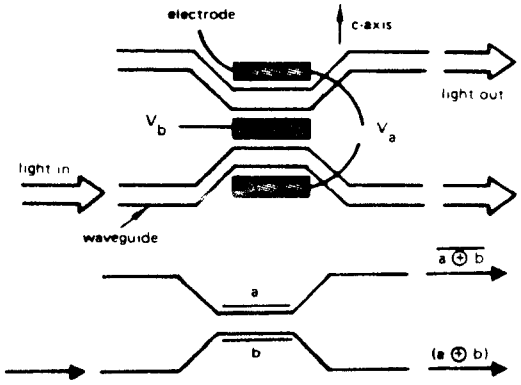
electrode
c-axis
light out
V_b
V_a
light in
waveguide
a
b
$\overline{a \oplus b}$
$(a \oplus b)$

(c)

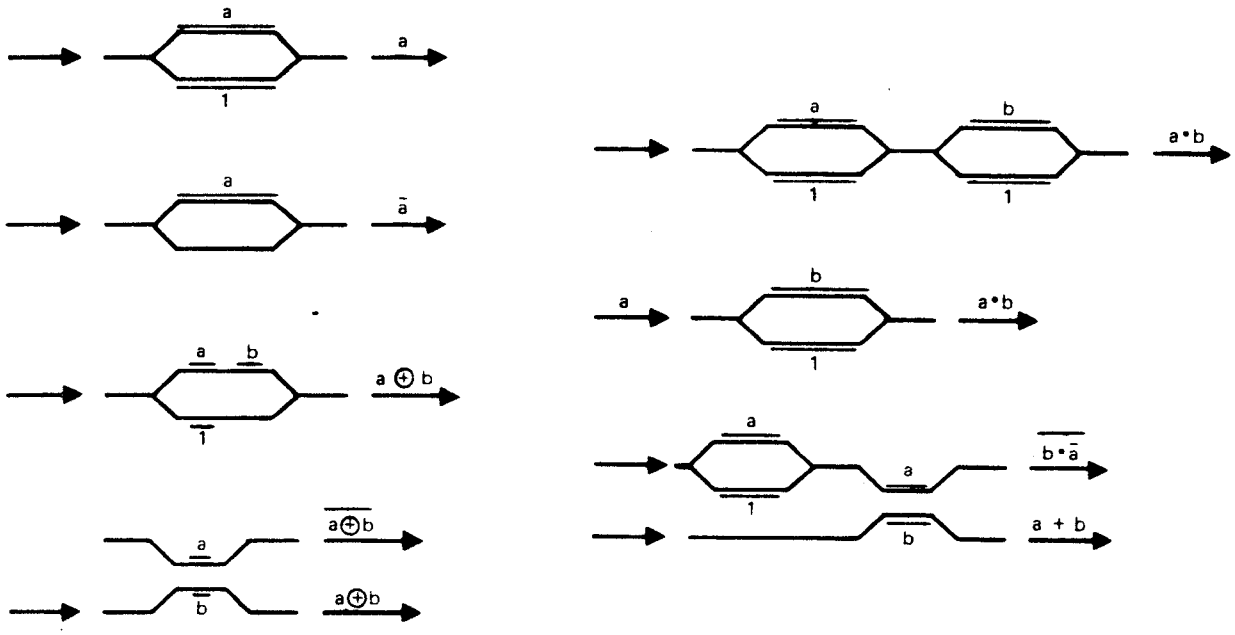
a
a
1
a
ā
a b
a ⊕ b
1
a
a⊕b
b
a⊕b
a
b
a•b
1
1
b
a
a•b
1
a
1
a
b•ā
b
a + b

(d)

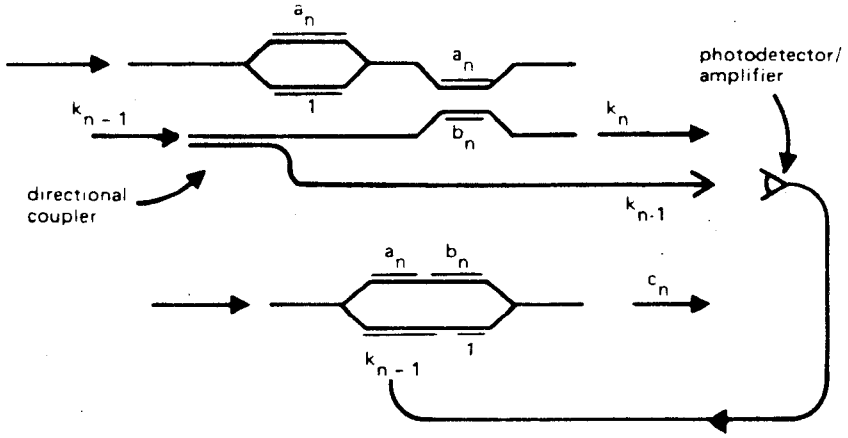
a_n
a_n
1
photodetector/
amplifier
k_{n-1}
k_n
b_n
directional
coupler
k_{n-1}
a_n b_n
c_n
1
k_{n-1}

(e)

Figure 4-9 Schematic diagram of a conventional approach to a 10x10 network switch.

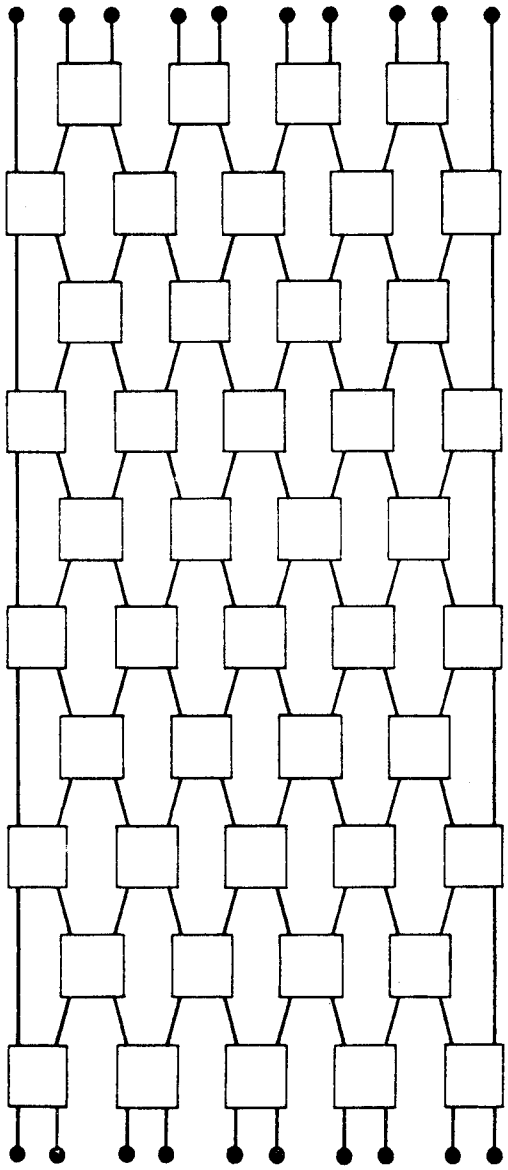

Figure 4-10 A two-stage 100x100 network switch composed of 20 units of 10x10 network switches.

The nth output channel of the mth unit in the left-hand column is connected to the mth input channel of the nth unit in the right-hand column.

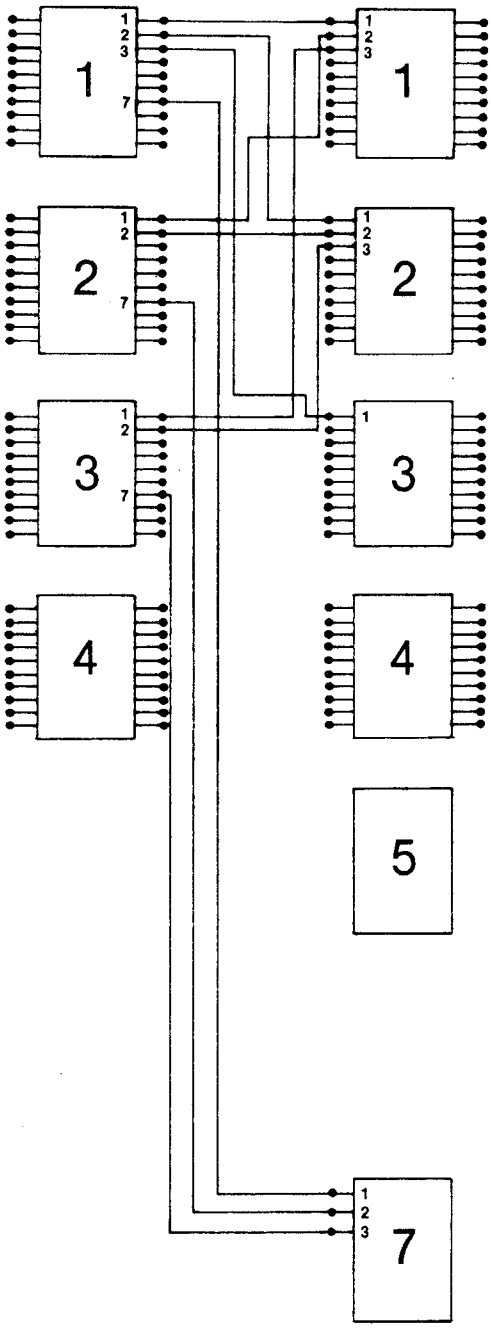
1
2
3
7
1
2
3
1
2
3
2
7
1
2
3
2
3
1
2
7
1
3
4
4
5
1
2
3
7
10
10

Figure 4-11 Integrated-optic Stimulus Probes.

(a) Integrated array of switched directional couplers: The output channels are aligned and coupled, via optical fibers to the corresponding pairs of photodiodes in the integrated opto-electric converter array shown in Figure 4-12 (a). Each switched directional coupler can switch the light beam from either one of the two output channel waveguides to the other, thus activating either photodiode in each corresponding pair.

(b) Integrated array of interferometric phase modulators: Depending on the voltage applied on the electrodes, the output light intensity could be either high or low. Each output port is aligned and coupled to the corresponding photodiode in the integrated opto-electric converter array shown in Figure 4-12 (b).

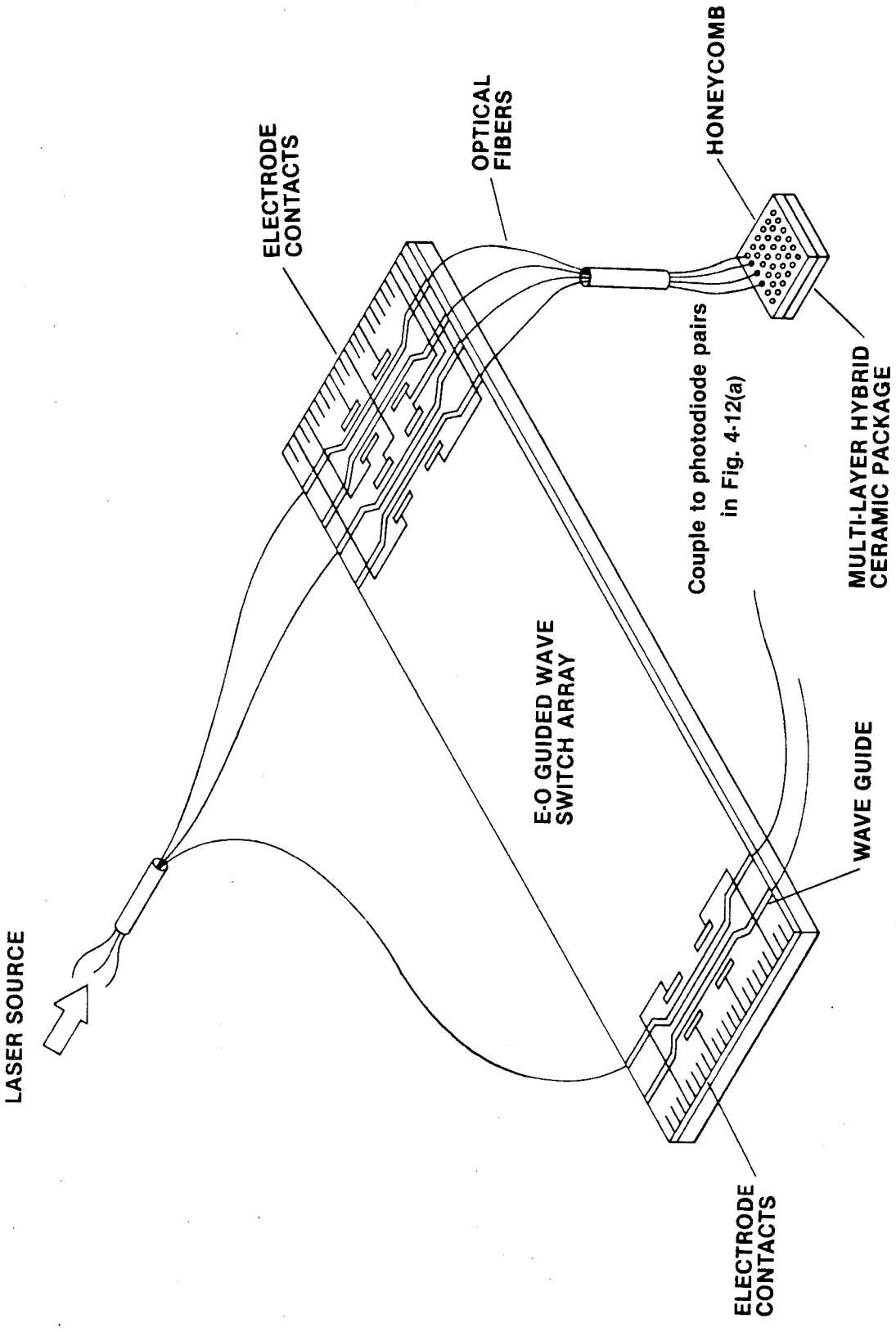
LASER SOURCE
ELECTRODE CONTACTS
OPTICAL FIBERS
HONEYCOMB
Couple to photodiode pairs in Fig. 4-12(a)
MULTI-LAYER HYBRID CERAMIC PACKAGE
E-O GUIDED WAVE SWITCH ARRAY
WAVE GUIDE
ELECTRODE CONTACTS

(a)

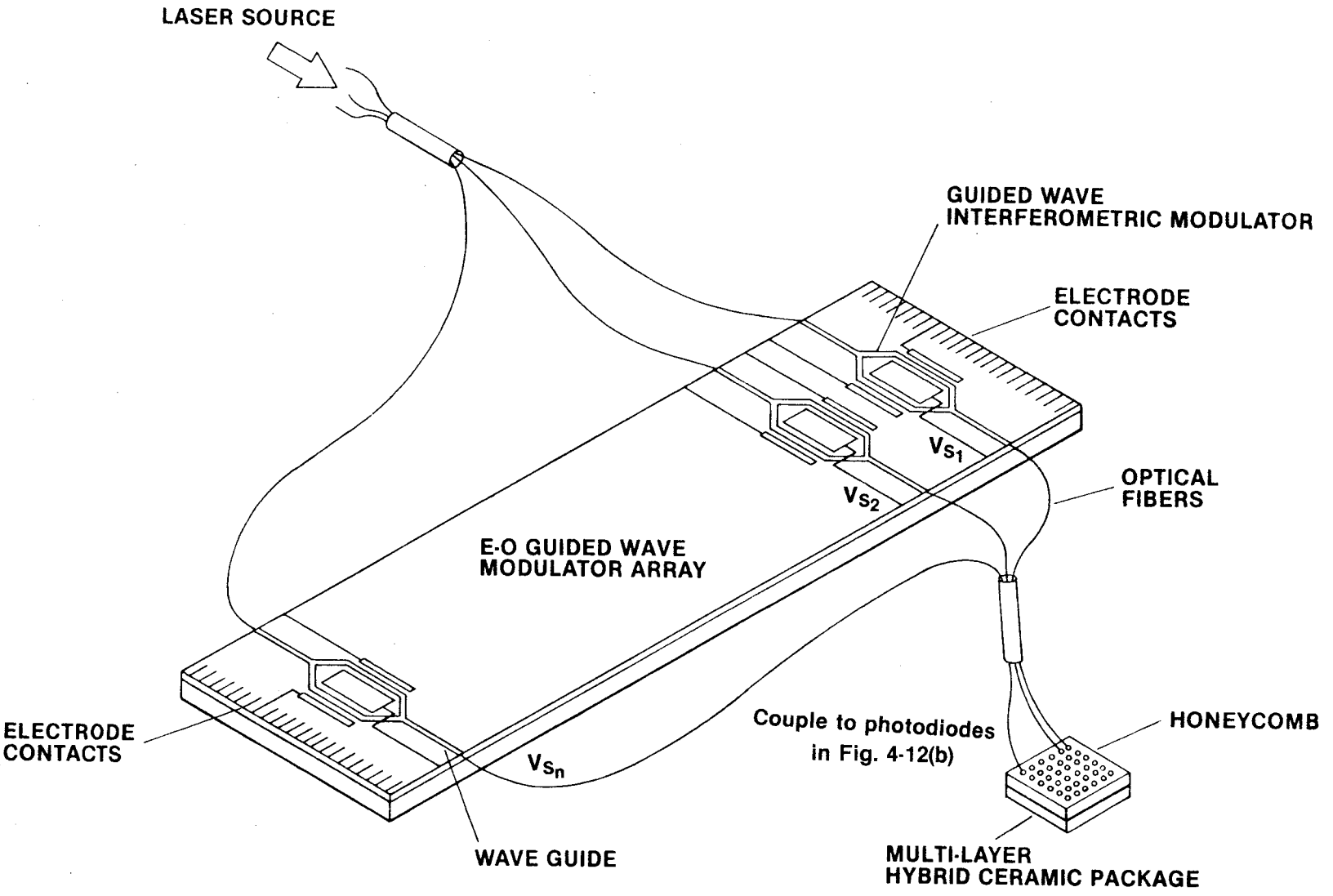

(b)

V_{S_n} = STIMULUS SIGNALS

Figure 4-12 Opto-electric Converters.

(a) Dual Diode Approach.

When photodiode D_1 is activated, the output voltage level would be "high". When diode D_2 is activated, the output would be at "ground" level, or low. The buffer serves to clean up the pulses and to boost the output current level to suit the logic family of the circuit under test (CUT). The honeycomb configuration is also indicated in the lower half.

(b) Single Diode Approach.

When the light level addressing D_o is "high" the output voltage level of the circuit is at "V", or "high". When the addressing light level is "low", the output voltage level is at "ground".

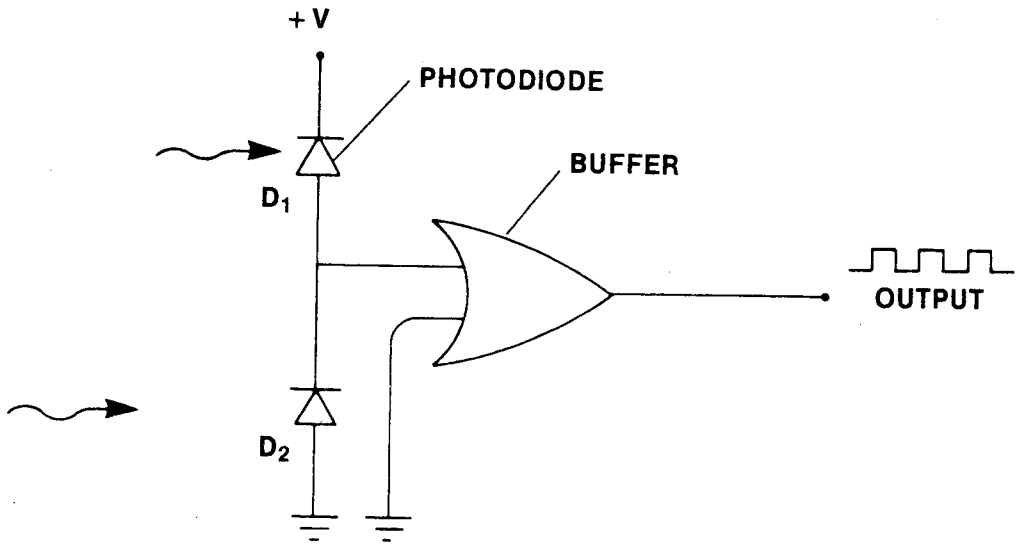
+V
PHOTODIODE
BUFFER
D_1
D_2
OUTPUT

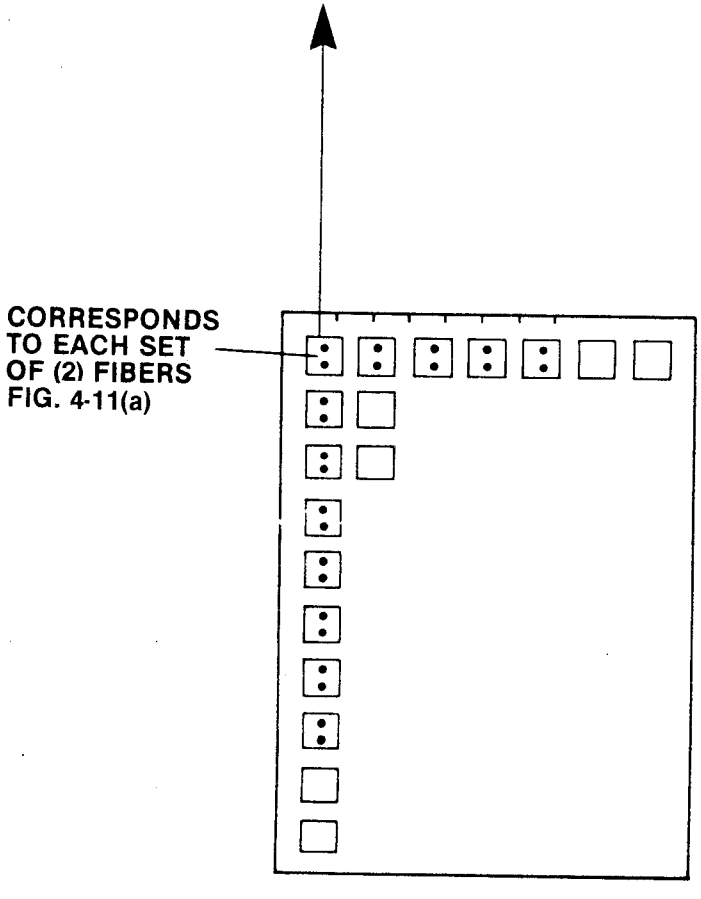
CORRESPONDS
TO EACH SET
OF (2) FIBERS
FIG. 4-11(a)

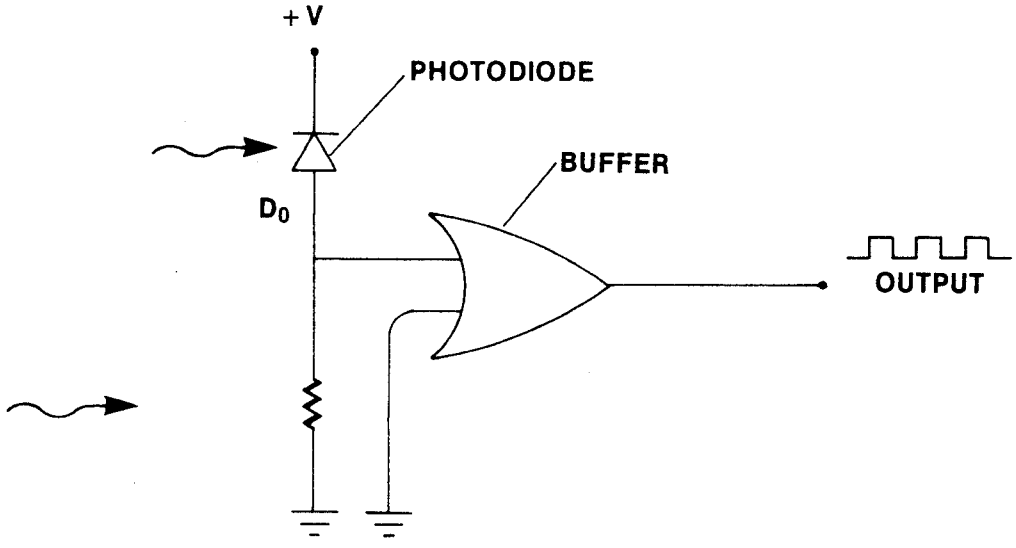
+V
PHOTODIODE
BUFFER
D_0
OUTPUT

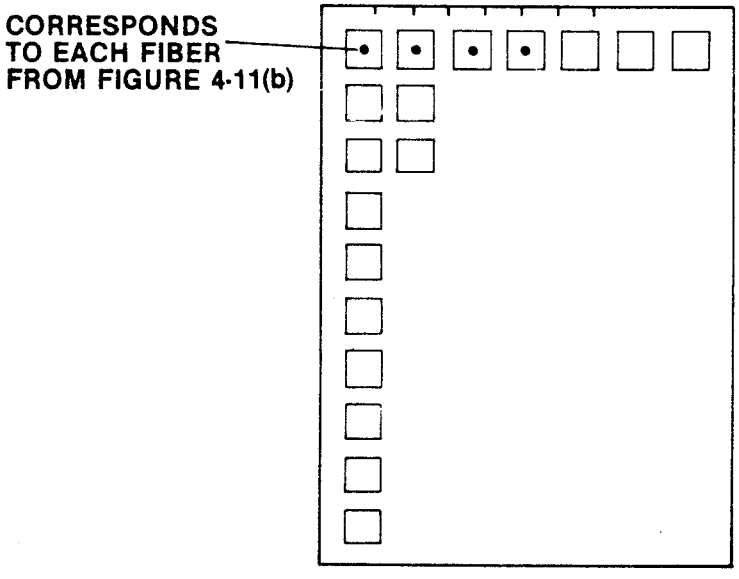
CORRESPONDS
TO EACH FIBER
FROM FIGURE 4-11(b)

Figure 4-13 Integrated-optic Response Probe.

The response signals V_{Pn} from the circuit under test (CUT) drive the interferometric phase modulator array to create an optical replica of the response signals of the CUT. Optical fibers carry this replica to a conventional photodiode array near the diagnostic equipment. There the optical signals are reconverted to electrical signals.

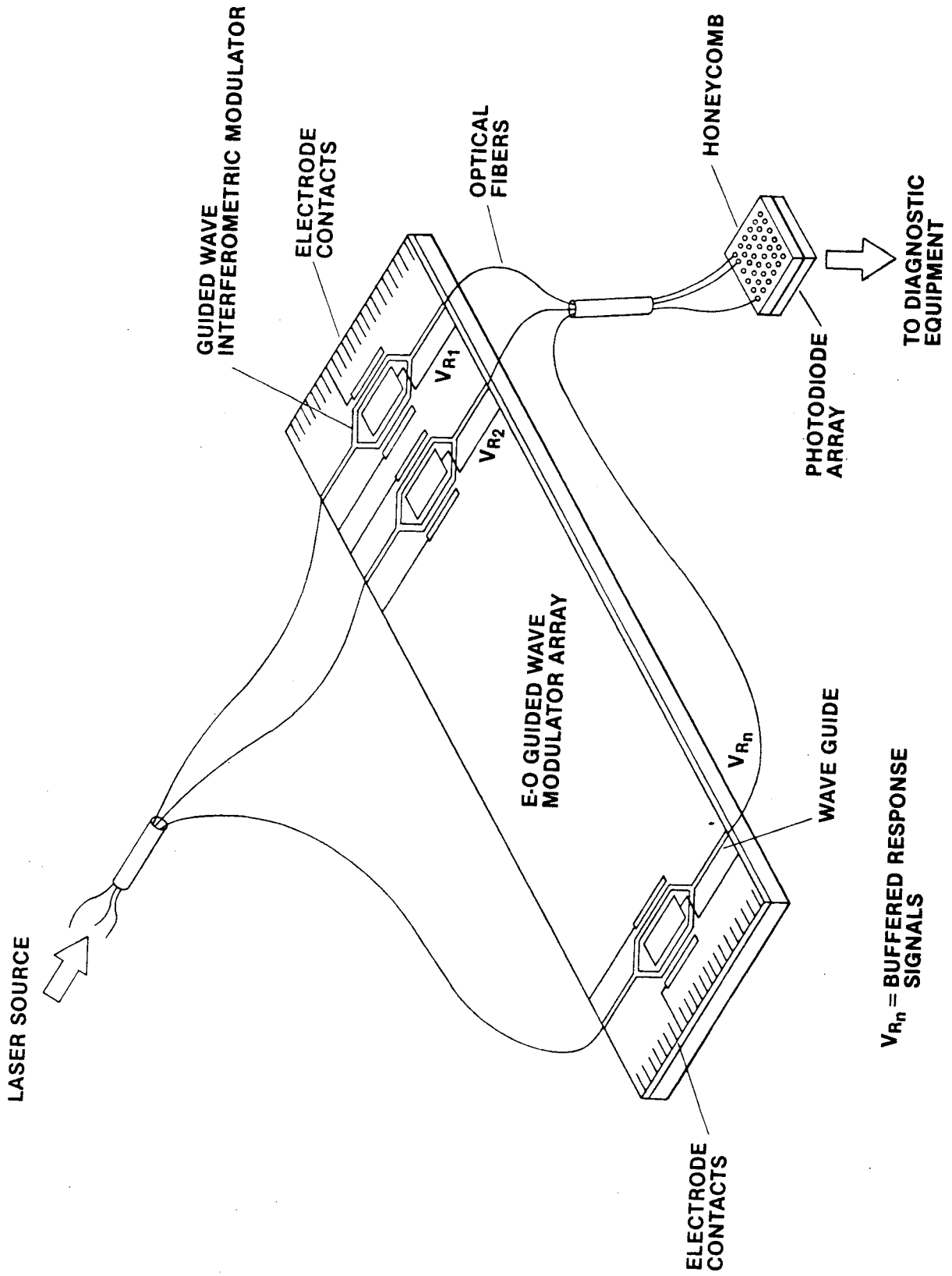
GUIDED WAVE INTERFEROMETRIC MODULATOR
ELECTRODE CONTACTS
OPTICAL FIBERS
HONEYCOMB
TO DIAGNOSTIC EQUIPMENT
PHOTODIODE ARRAY
V_{R_1}
V_{R_2}
E-O GUIDED WAVE MODULATOR ARRAY
V_{R_n}
WAVE GUIDE
LASER SOURCE
ELECTRODE CONTACTS
V_{R_n} = BUFFERED RESPONSE SIGNALS

Figure 4-14 The system schematic diagram of the optical stimulus-response probe using micromechanical switch array as a vehicle for probe configuration and reconfiguration.

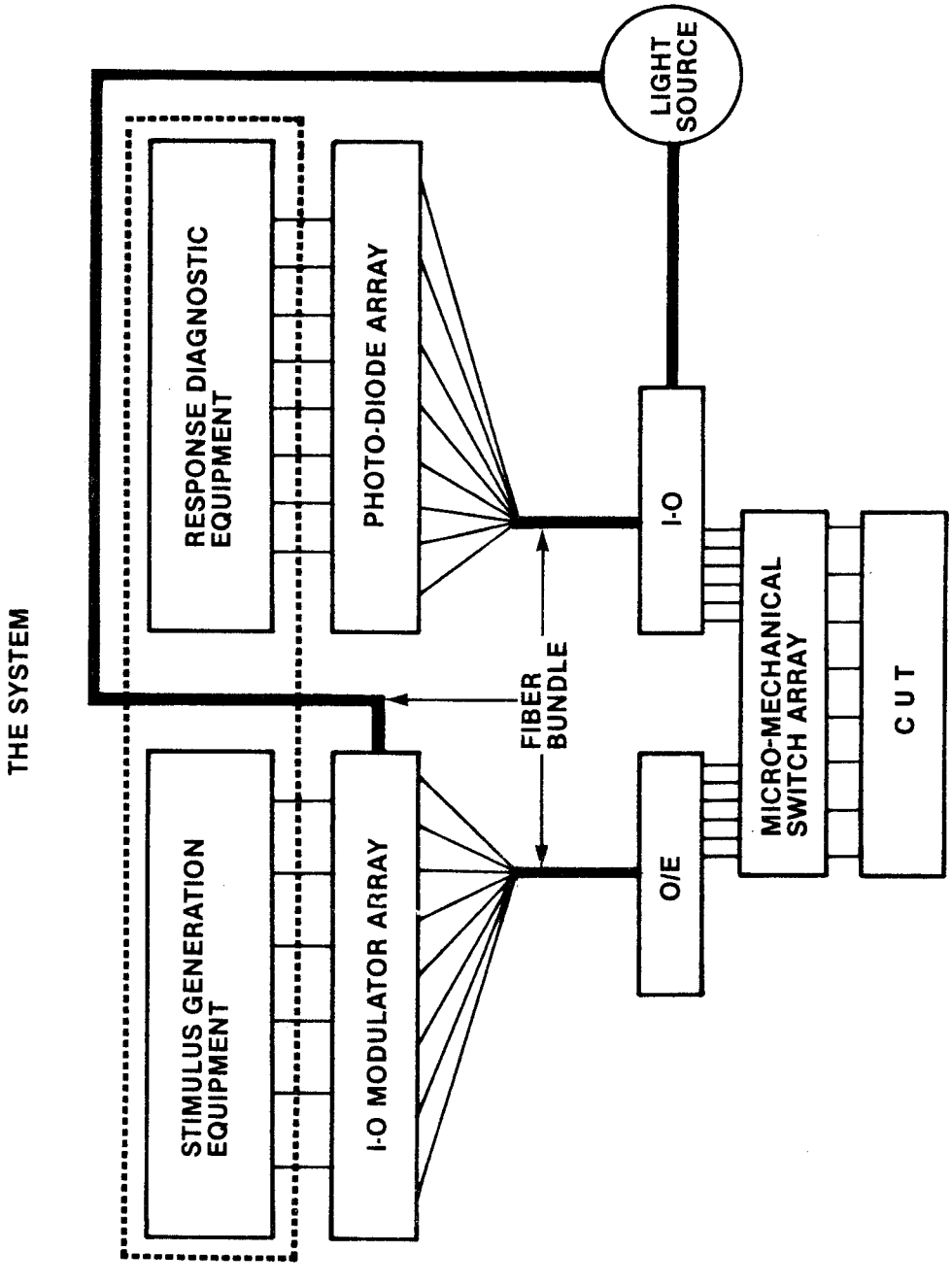
THE SYSTEM
LIGHT SOURCE
RESPONSE DIAGNOSTIC EQUIPMENT
PHOTO-DIODE ARRAY
I-O
MICRO-MECHANICAL SWITCH ARRAY
C U T
FIBER BUNDLE
STIMULUS GENERATION EQUIPMENT
I-O MODULATOR ARRAY
O/E

Figure 4-15 The schematic diagram of an input/output bidirectional opto-electric conversion circuitry. Each channel requires two independently programmable light beams. The stimulus data to the CUT is detected by G_0, buffered by G_1 and injected into CUT. When the diode D_0 is activated, it forces G_1 into a floating output state, effectively disconnecting G_1 from the CUT. In this case, a response signal from the CUT is buffered by G_3, which in turn drives the corresponding optical modulator in Figure 4-17.

When G_1 is *not* in the floating output state, the injected voltage to the CUT by G_1 is also buffered by G_3, converted to optical signal and transmitted to diagnostic equipment.

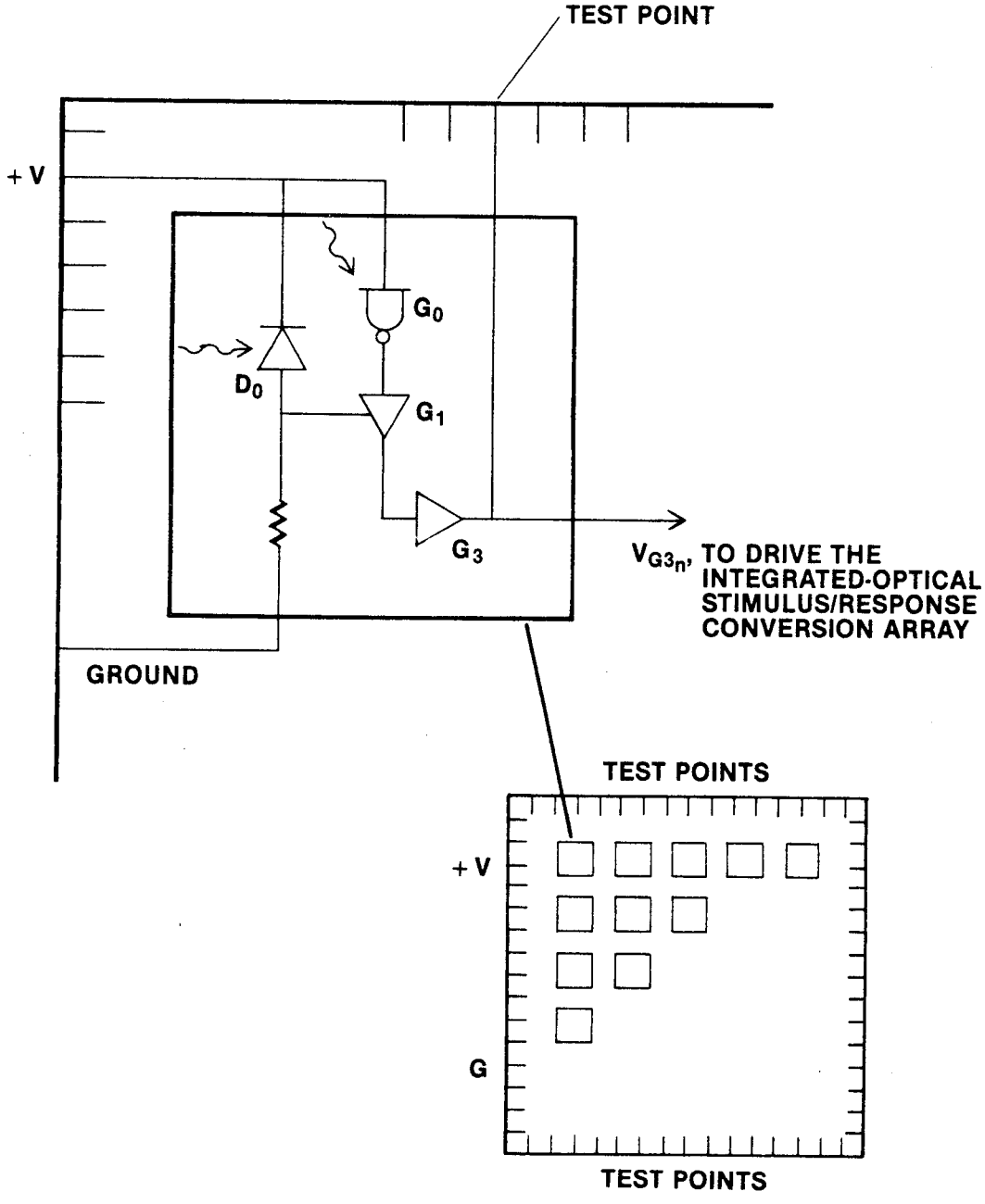
TEST POINT
+V
G_0
D_0
G_1
G_3
V_{G3_n}, TO DRIVE THE INTEGRATED-OPTICAL STIMULUS/RESPONSE CONVERSION ARRAY
GROUND
TEST POINTS
+V
G
TEST POINTS

Figure 4-16 An integrated-optical modulator array addressing the bidirectional opto-electric converter array shown in Figure 4-15. A two-stage switched directional coupler could achieve the same functionality as a pair of interferometric phase modulators shown in this figure.

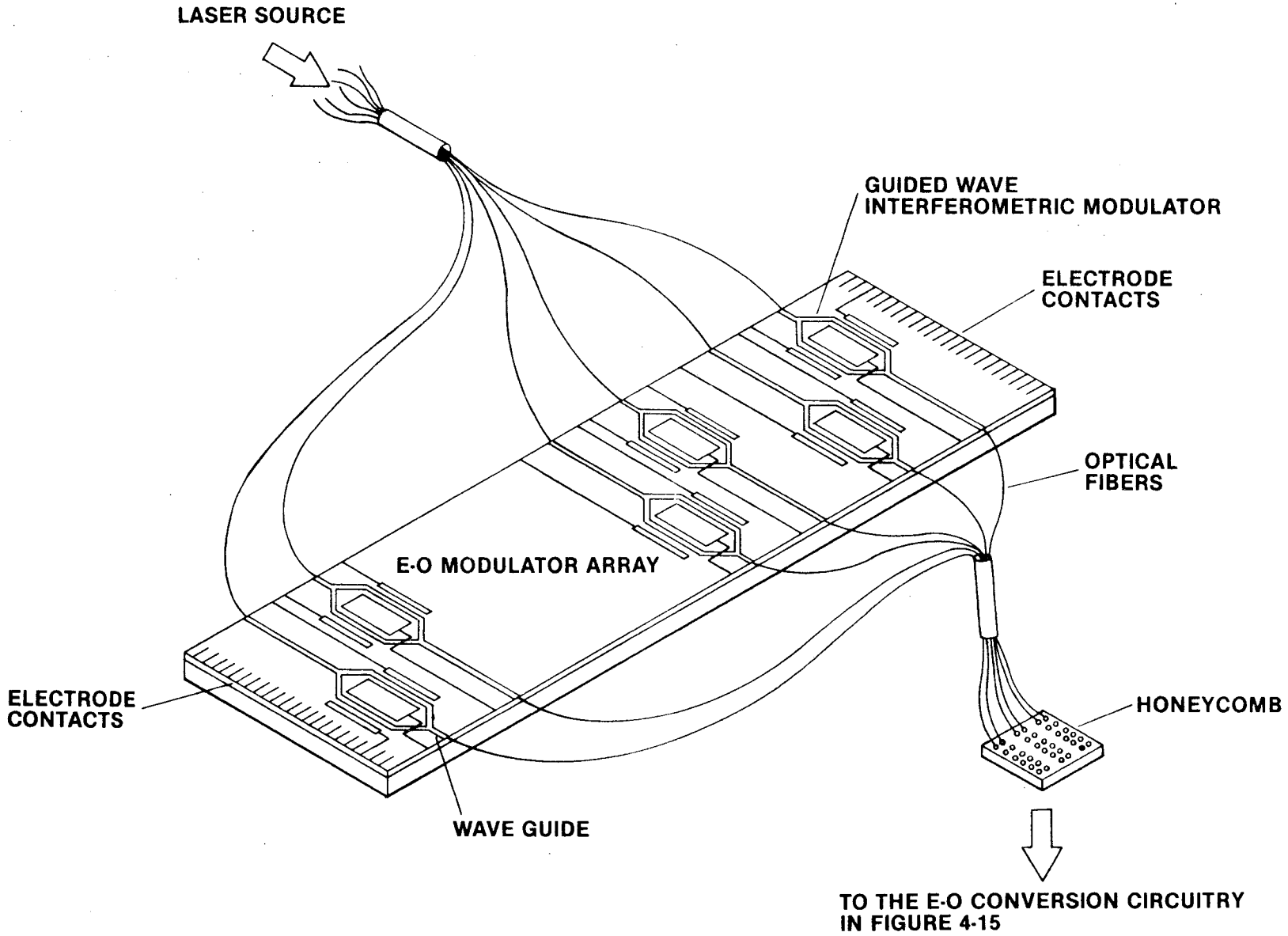
LASER SOURCE
GUIDED WAVE
INTERFEROMETRIC MODULATOR
ELECTRODE
CONTACTS
OPTICAL
FIBERS
E-O MODULATOR ARRAY
ELECTRODE
CONTACTS
HONEYCOMB
WAVE GUIDE
TO THE E-O CONVERSION CIRCUITRY
IN FIGURE 4-15

Figure 4-17 The Stimulus/Response Feedback Integrated-Optical Modulator Array.

The output voltage V_{G3n} of gates G_{3n} from Figure 4-15 drive these modulators to obtain an optical replica of signals at the test points whether stimuli or responses. The optical replica are then transmitted to the diagnostic equipment and converted to electrical signals by a photodiode array.

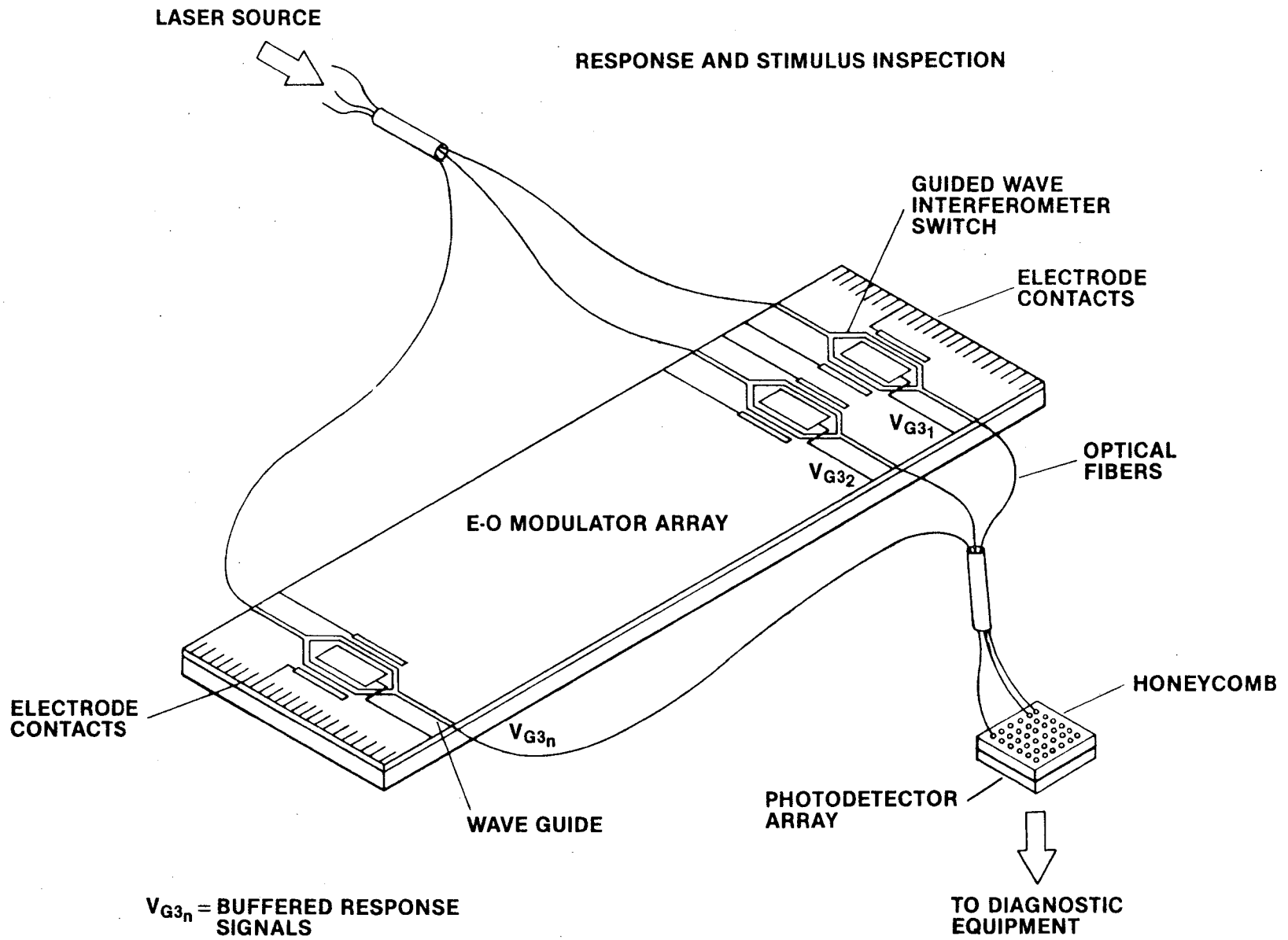
LASER SOURCE
RESPONSE AND STIMULUS INSPECTION
GUIDED WAVE INTERFEROMETER SWITCH
ELECTRODE CONTACTS
V_{G3_1}
V_{G3_2}
OPTICAL FIBERS
E-O MODULATOR ARRAY
HONEYCOMB
ELECTRODE CONTACTS
V_{G3_n}
WAVE GUIDE
PHOTODETECTOR ARRAY
TO DIAGNOSTIC EQUIPMENT
V_{G3_n} = BUFFERED RESPONSE SIGNALS

Figure 4-18 The Conceptual System diagram of the bidirectional stimulus/ response probe.

THE SYSTEM

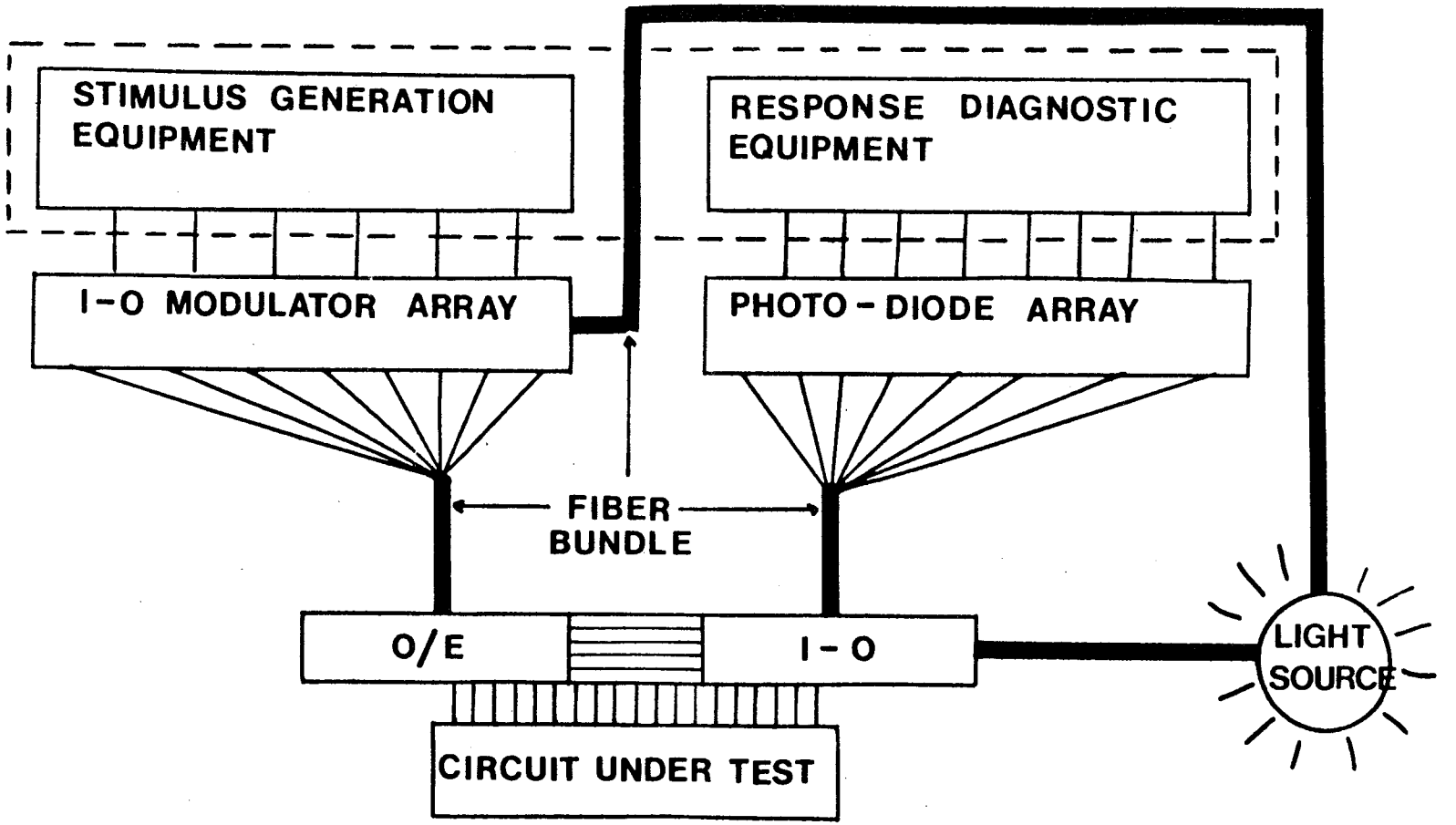
STIMULUS GENERATION EQUIPMENT
RESPONSE DIAGNOSTIC EQUIPMENT
I-O MODULATOR ARRAY
PHOTO-DIODE ARRAY
FIBER BUNDLE
O/E
I-O
LIGHT SOURCE
CIRCUIT UNDER TEST

Figure 4-19 The interfacing of the integrated-optical components, the opto-electric component and the circuit under test.

This multilayer ceramic hybrid circuit in conjunction with the available high frequency connector techniques used in high frequency Tek products is a proposed solution.

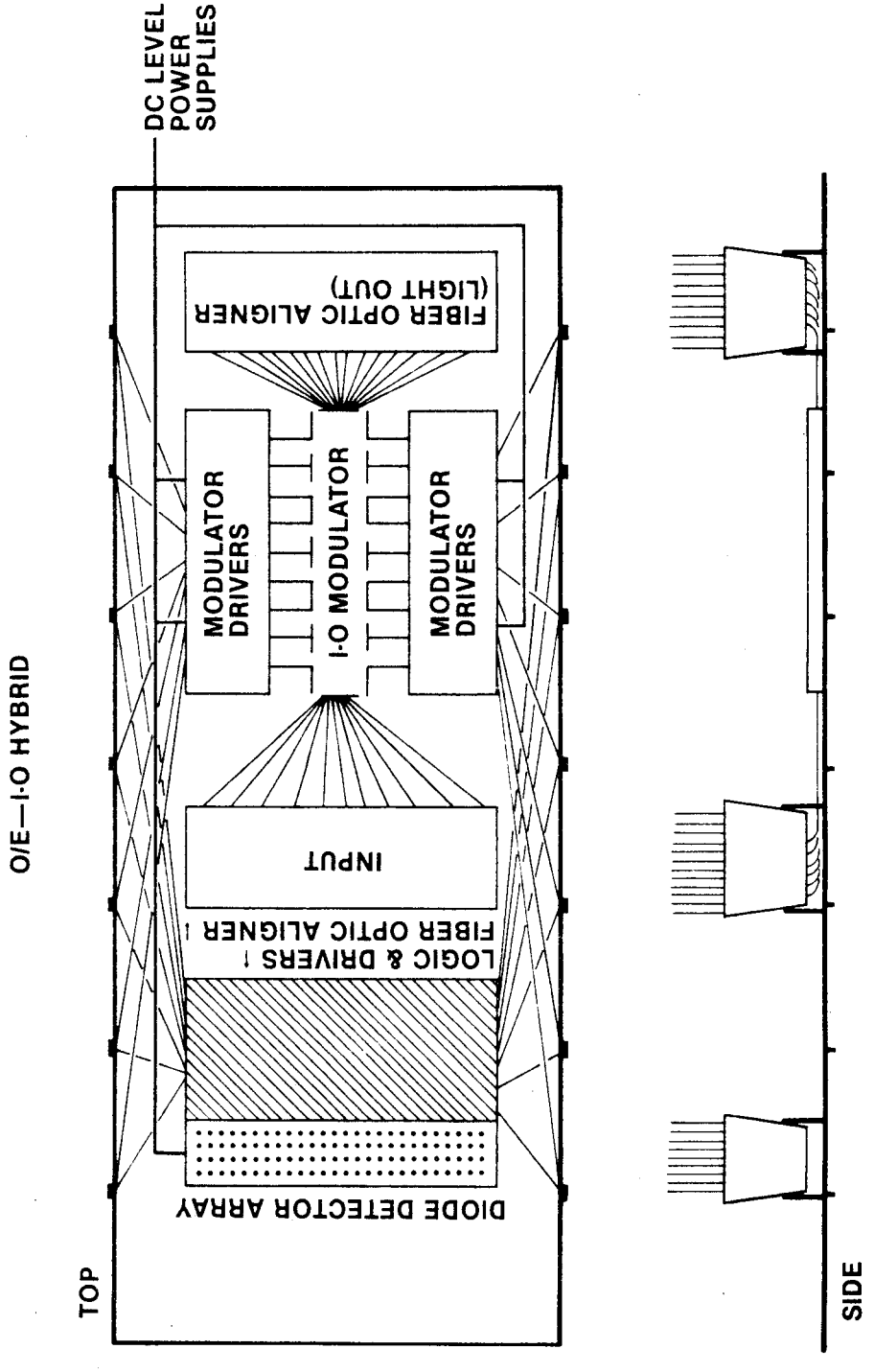
O/E—I-O HYBRID
DC LEVEL POWER SUPPLIES
FIBER OPTIC ALIGNER (LIGHT OUT)
MODULATOR DRIVERS
I-O MODULATOR
MODULATOR DRIVERS
INPUT
LOGIC & DRIVERS
FIBER OPTIC ALIGNER
DIODE DETECTOR ARRAY
TOP
SIDE

Figure 4-20 A polarization independent integrated-optical narrow band wavelength filter.

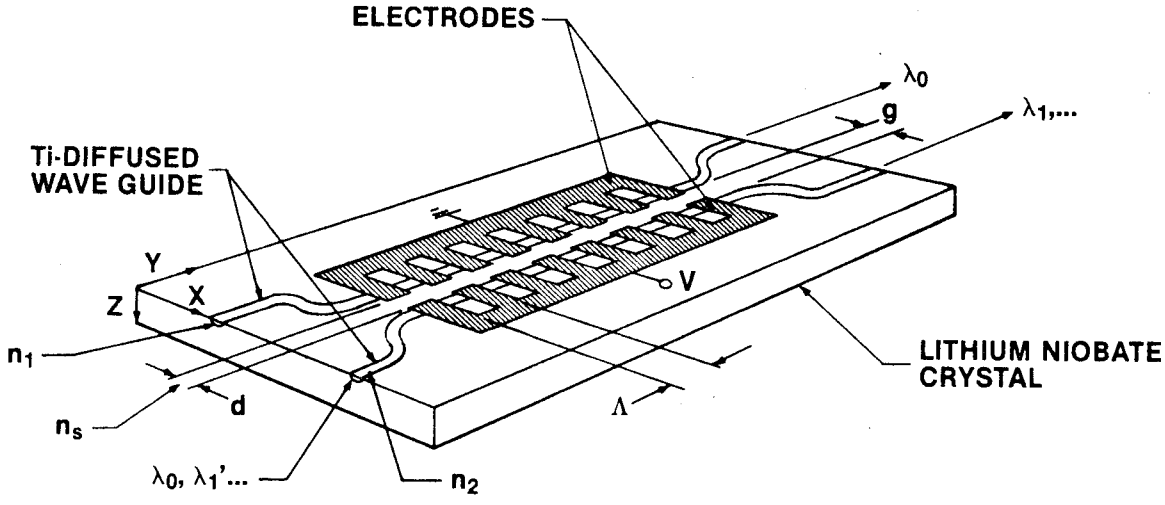
ELECTRODES
λ_0
λ_1,...
g
Ti-DIFFUSED
WAVE GUIDE
Y
Z
X
V
n_1
n_s
d
Λ
LITHIUM NIOBATE
CRYSTAL
λ_0, λ_1'...
n_2

REFERENCE LISTING - CHAPTER 4

1. M. Papuchon et al, "Electrically Switched Optical Directional Coupler: COBRA," Appl. Phys. Lett., Vol. 27, p. 289, September 1975.
2. R.V. Schmidt, H. Kogelnik, "Electro-optically Switched Coupler with Stepped $\Delta\beta$ Reversal Using Ti-Diffused $LiNbO_3$ Waveguides," Appl. Phys. Lett., Vol. 28, No. 9, p. 503, May 1976.
3. Y. Ohmachi, J. Noda, "Electro-Optic Light Modulator with Branched Ridge Waveguide," Appl. Phys. Lett., Vol. 27, No. 10, p. 544, November 1975.
4. J.M. Hammer, W. Phillips, "Low-Loss Single-Mode Optical Waveguides and Efficient High-Speed Modulators of $LiNb_xTa_{1-x}O_3$ on $LiTaO_3$," Appl. Physics Letters, Vol. 24, No. 11, p. 545, June 1974.
5. Masayuki Izutzu, Yasukuni Yamanl, Tadasi Sueta, "Broad-Band Traveling-Wave Modulator Using a $LiNbO_3$ Optical Waveguide," IEEE J. Quantum Electronics, Vol. QE-13, No. 4, p. 287, April 1979.
6. Masayuki Izutzu, Takushi Itoh, Tadasi Sueta, "10 GHz Bandwidth Traveling-Wave $LiNbO_3$ Optical Waveguide Modulator," IEEE J. Quantum Electronics, Vol. QE-14, No. 6, p. 394, June 1978.
7. Tadasi Sueta, Masayuki Izutzu, "High-Speed Guided-Wave Optical Components," Technical Digest, IOOC '81, TUM2, San Francisco, California, April 27-29, 1981.
8. E.A.J. Marcatili, "Optical Subpicosecond Gate," Applied Optics, Vol. 19, No. 9, p. 1468, May 1980.
9. W.E. Martin, "A New Waveguide Switch/Modulator for Integrated Optics," Applied Physics Letters, Vol. 26, No. 10, p. 562, May 1975.
10. H.F. Taylor, "Integrated Optical Logic Circuits," Technical Digest, Topical Meetings on Integrated and Guided-Wave Optics," TuC4-1, January 16-18, 1978.
11. H.F. Taylor, "An Optical Analog to Digital Converter - Design and Analysis," IEEE J. Quantum Electronics, Vol. QE-15, No. 4, p. 210, April 1979.
12. F.J. Leonberger, "High Speed Electro-Optical Signal Conversion Devices," Proceedings SPIE, Vol. 218, p. 41, February 6-7, 1980, Los Angeles, California.
13. C.M. Verber, D.W. Vahey, V.E. Wood, R.P. Kenan, "An Integrated Optics Processor for Multichannel Data," IOOC '77, B1-3, Tokyo, Japan.
14. C.M. Verber, R.P. Kenan, "Integrated Optical Circuit for Performing Vector Subtraction," Proceedings SPIE, Vol. 218, p. 23, February 6-7, 1980, Los Angeles, California.
15. J.H. Marburger, F.S. Felber, "Theory of a Lossless Nonlinear Fabry-Perot Interferometer," Physical Review A, Vol. 17, No. 1, p. 335, January 1978.
16. D.A.B. Miller, S.D. Smith, "Optical Bistability and Signal Amplification in a Semiconductor Crystal: Applications of New Low-Power Nonlinear Effects in InSb," Appl. Phys. Lett., Vol. 35, No. 9, p. 658, November 1979.

17. H.F. Taylor, "Optical-Waveguide Connecting Networks," Electronics Letters, Vol. 10, No. 4, p. 41, February 1974.

18. R.V. Schmit, L.L. Buhl, "Experimental 4x4 Optical Switching Network," Electronics Letters, Vol. 12, No. 22, p. 575, October 1976.

19. R.A. Soref, "Optical Switch Study," NTIS AD/A 007009, February 1975.

20. T. Horimatsu, H. Nakajima, E. Miyauchi, "TE/TM Mode Splitter Using An Intersecting Waveguide," Technical Digest, IOOC '81, TU13, p. 68.

21. K.E. Petersen, "Micromechanical Light Modulator Array Fabricated on Silicon," Applied Physics Letters, Vol. 31, No. 8, p. 521, October 1977.

22. Rudi Hendel, "Laser Processing Program Proposal," Unpublished.

23. R.C. Alferness, Applied Physics Letters, Vol. 35, p. 748, 1979.

24. R.C. Alferness, L.L. Buhl, "Polarization Independent Optical Filter Using Interwaveguide TE/TM Conversion," "Waveguide Electro-optic Polarization Transformer," Technical Digest IOOC '81, TU 12, TU 14, p. 68, April 27-29, 1981, San Francisco, California.

25. N. Tsukada, T. Nakayama, "Polarization Insensitive Integrated-Optic Switch: A New Approach," Technial Digest IOOC '81, TU 15, p. 70.

26. C.H. Bulmer, R.P. Moeller, "Fiber Coupled Phase-Shifter for Use in Optical Gyroscopes," Technical Digest IOOC '81, WL5, p. 130.

27. Kubota, Junichi Noda, Osamu Mikami, "Traveling Wave Optical Modulator Using A Directional Coupler $LiNbO_3$ Waveguide," IEEE, J. Quantum Electronics, Vol. QE 16, No. 7, p. 754, July 1980.

CHAPTER 5

SOURCES AND DETECTORS

Optical sources and photodetectors are two vast fields by themselves. It is quite impossible to cover all the aspects of these subjects. This chapter is not intended to be a comprehensive survey, but rather an overview from the applications standpoint.

5.1 Sources

Semiconductor light emitting diodes (LED) and laser diodes are the preferred light sources for fiber optical systems because of their compactness and cost effectiveness. The laser diodes are the practical choice for integrated-optical systems and other high data rate applications because of their much narrower spectrum spread and higher modulation bandwidth.

Because of the transmission loss characteristics of optical fibers, longer wavelength sources (1.3 μm and 1.5 μm) are preferred, especially in long distance optical fiber systems. In short distance data transmission and signal processing applications the wavelength is not a major factor.

The lifetime of both LED and lasers have made great progress during the past 3 years. The measured lifetime now exceeds 40,000 hours. Many manufacturers of laser diodes are now specifying 100,000 hours of CW lifetime. When modulated, the lifetime was observed to be shorter. However, definitive data is not yet available.

5.1.1 LED versus Laser Diodes

LED

Fabrication of LED is a more mature technology. LED has higher construction tolerances and thus is cheaper. Its optical output power is approximately linear with the driving current. The temperature dependence of its power/current characteristics is relatively small, requiring no temperature regulation circuitry.

However, the emission spectrum of LED is broad (300 ~ 500 Å), resulting in a larger pulse dispersion. The modulation capability is limited by the carrier lifetime (100 MHz - 200 MHz). The radiance energy is low, because of the relatively large beam divergence (120° x 40°), resulting in a low coupling efficiency to waveguides (<10%).

Laser Diodes

Laser diodes have more critical construction tolerances and thus are more expensive than LED. Their threshold current and quantum efficiency vary with temperature, thus requiring temperature regulation circuitry. Their linearity of output power vs. current characteristics depends on the operating conditions.

However, when biased with DC at threshold, laser diodes can be modulated at above 1 GHz rate. The emission linewidth is narrow (<20 Å), resulting to much smaller pulse dispersion. The relatively high radiance power (40° x 10° beam divergence) enables a higher coupling efficiency (~60%) to waveguides.

Conclusion

LED is preferred for its lower cost in lower bit rate (<100 MHz), short dis-

tance applications. Laser diode is the only practical choice for higher bit rate (>200 MHz) and long distance applications.

5.1.2 Short Wavelength Sources versus Longwave Length Sources

Short wavelength (0.8 ~ 0.9 μm) sources are typically based on GaAlAs/GaAs technology, which is more mature when compared to the (InGa) (AsP)/InP technology for longer wavelength (1.1 ~ 1.65 μm) sources.

To match the fiber properties, 1.3 μm and 1.5 μm are the most attractive wavelengths. Various buried heterostructure (InGa) (AsP)/InP devices at these wavelengths have been extensively studied for several years[1-7].

Performances of various LEDs are listed in Table 5-1. The power vs. current characteristics of a typical GaAlAs/GaAs LED and a typical InGa AsP/InP LED are illustrated in Figures 5-1 and 5-2.

The power vs. current characteristics at various temperatures of a typical GaAlAs/GaAs double heterostructure (DH) laser diode and a typical (InGa) (AsP)/InP to DH to laser diode are illustrated in Figures 5-3 and 5-4.

5.1.3 Power Efficiency

The power efficiency of LED and laser diodes are influenced by the internal quantum efficiency, the crystalline structure, the recombination region, the threshold current (for laser diodes) and the operating temperature and current.

The differential quantum efficiency η_{diff} can be calculated as follows:

$$\eta_{diff} = \eta_i \frac{ln\ (1/R)}{\propto L + ln\ (1/R)},$$

where η_i is the internal quantum efficiency, R is the facet reflectivity and $\propto$ is

the cavity absorption coefficient and L is the cavity length.

The optical power P emitted by a laser diode can be calculated as follows:

$$P = \frac{h\nu}{e}(I - I_{th})\,\eta_{diff} \quad ,$$

where I is the operating current, I_{th} is the threshold current, η_{diff} is the differential quantum efficiency, and $h\nu$ is the photon energy which is equivalent to the band gap energy E_g.

The power efficiency is then:

$$\eta_p = \frac{P}{I^2 R_s + I\,h\nu/e} \quad ,$$

where R_s is the junction resistivity.

The power efficiency of LED can be similarly calculated. For both LED and laser diode the power efficiencies range typically from a few percent to approximately 10%.

The quantum efficiencies of various LEDs are listed in Table 5-1. The quantum efficiency and threshold current of laser diodes are both temperature dependent, typically as shown in Figure 5-5.

5.2 Detectors

The most important parameters of a photodetector are its quantum efficiency, noise, responsivity (Amp/Watt), and its response time.

The quantum efficiency determines the responsivity of the device. The responsivity and noise determine the signal to noise ratio of the device. The response time determines the frequency bandwidth of the device. The quantum efficiency and responsivity are both spectral dependent. The detector noise is often represented in combination with the responsivity as "noise equivalent

power" (NEP), defined as the bandwidth normalized optical flux input which results in a signal to noise ratio of 1.

5.2.1 Quantum Efficiency and Responsivity

Quantum efficiency is defined as the ratio of the number of useful photoelectrons released to the number of incident photons, i.e.,

$$\eta_Q = \frac{\#\ of\ photoelectrons}{\#\ incident\ photons}$$

Quantum efficiency can be related to the responsivity, the Ampere current generated per Watt incident optical power as follows:

$$\eta_Q = \frac{(P_o \cdot S)/e}{P_o/h\upsilon} = \frac{hc}{e\lambda_o} \cdot S$$

Where P_o is the incident optical power,
S is the responsivity in Amp/Watt,
e is the electron charge,
h is Planck's constant,
ν is the optical frequency,
λ_o is the optical wavelength.

For assumed values of quantum efficiency, the spectral responsivity can be calculated as illustrated in Figure 5-6.

The quantum efficiency of a photodetector can be determined at each wavelength by plotting the measured responsivity at each wavelength on Figure 5-6. As an example, the spectral responsivity and associated quantum efficiency of a Mitsubishi Electric avalanche photodiode (PD1000) is illustrated in Figure 5-7.

Antireflection Coating

For a photodiode of only moderate quality, the internal quantum efficiency for the photons absorbed in the semiconductor is nearly 100%. However, a significant fraction of the photon flux is reflected at the device surface because of the discontinuity in the index of refraction. The reflection coefficient for normal incidence at the boundary of air, n=1, and the semiconductor, $n \approx 3.5$, is:

$$R = \frac{(n_1 - n_2)^2}{(n_1 + n_2)^2} \approx 30\%.$$

An anti-reflection coating of thickness ¼ of the interested wavelength, with refractive index between that of the air and the semiconductor is used to optimize the effective quantum efficiency.

For silicon devices, an 80% effective quantum efficiency is quite common. GaAs based devices normally have 60% to 70% quantum efficiency.

5.2.2 Response Time

The response time of a photodetector is determined by the larger of the carrier transit time across the depletion region, or the product of the diode load resistance and capacitance. The transit time in most direct-gap photodiodes is approximately 10 psec. Thus, the response time is RC limited. The capacitance of a photodiode with 100 μm diameter is typically 1 pf. The RC limited risetime is approximately 100 psec. Faster devices can be made by reducing the device active area. However, the optical flux would decrease correspondingly unless focusing optics is implemented. The load resistance R is also closely tied to the signal to noise ratio of the device. A balance has to be reached between optimizing the response time and the signal to noise ratio.

5.2.3 Signal to Noise Ratio

The sources of noise in a photodetection system are: 1) shot noise in the optical signal, 2) shot noise and thermal noise in the photodetector, and 3) excess noise generated in the detector by avalanche gain and 4) the external amplifier noise.

The photocurrent generated by the incident optical power P_o can be expressed as:

$$I_p = 2\frac{P_o}{h\nu}\cdot\eta_Q\cdot e.$$

Associated with the average photocurrent I_p, is a mean square shot noise

$$\bar{i}_{sp}^2 = 2eI_pB,$$

where B is the modulation frequency (i.e., post-detection bandwidth).

A reasonably good semiconductor laser has a shot noise (background) power 50 dB below its signal power:

$$P_B \approx 10^{-5}P_o.$$

This generates an additional noise current in the photodetector

$$I_B = 2\frac{P_B}{h\nu}\cdot\eta_Q\cdot e,$$

and a mean square shot noise

$$\bar{i}_B^2 = 2eI_BB.$$

The shot noise caused by the dark current I_D in the photodetector is:

$$\bar{i}_d^2 = 2eI_DB.$$

For devices with avalanche gain the mean square noise in the amplified current can then be written as follows:

$$\overline{i_n^2} = 2e\,(I_p + I_D + I_B)\,B\,M^2\,F(M)$$

where M is the multiplication gain and F(M) is the excess noise factor caused by the multiplication.

Detector thermal noise and the amplifier noise can be accounted for by an added mean square noise current

$$\overline{i_T^2} = \frac{4kT_{eff}\,B}{R_L}$$

where k is the Boltzmann's constant, R_L is the load resistance of the photodiode and T is the effective noise temperature which includes the detector thermal noise as well as the noise added to the system by the external amplifier. For an FET amplifier circuit, the effective noise temperature is approximately 1000K.

The photodiode load resistance R_L can be chosen as large as possible to minimize the thermal noise, within the limit of the bandwidth requirement and the diode capacitance:

$$B = \frac{1}{2\pi R_L C}.$$

Finally, the signal to noise power ratio can be written as:

$$\frac{S}{N} = \frac{\tfrac{1}{2}\,I_P^2\,M^2}{2e\,(I_P+I_B+I_D)\,BM^2F(M)+(4kT_{eff}\,B/R_L)}.$$

$$= \frac{\tfrac{1}{2}\,(2P_o\eta_Q\,e/h\nu)^2}{2e\,\{(2\eta_Q\,e/h\nu)\,(P_o+P_B)+I_D\}\,BF(M)+(4kT_{eff}\,B/M^2R_L)}$$

The noise equivalent power (NEP) quoted in most photodiode specifications usually disregard the external amplifier noise and the optical source shot noise.

A 10^{-14} $W/\sqrt{Hz}$ to 10^{-16} $W/\sqrt{Hz}$ NEP is commonly obtained in off-the-shelf photodiodes.

5.2.4 Devices

Device Type

Most commonly used semiconductor photodetection devices are p-n junction photodiodes, p-i-n photodiodes and avalanche photodiodes (APD), as shown in Figures 5-8 to 5-10 respectively. Responsivities and quantum efficiences of various high speed (70-80 psec) photodiodes are illustrated in Figure 5-11. The responsivity versus characteristics of a typical APD is illustrated in Figure 5-12.

Wavelengths

The spectral response of silicon devices cuts off at 1.1 μm. For longer wavelength applications, germanium or GaInAs devices are usually adapted. Germanium devices[8] have an absorption edge at 1.6 μm as shown in Figure 5-13. GaInAs devices have an absorption edge at 1.7 μm as shown in Figure 5-14.

Detection Speed

Response times of 50 psec have been reported for silicon p-i-n photodiodes and 100 psec for GaAlAs avalanche devices. Thin film amorphous silicon photodetectors[9] (Figure 5-15) have potential to achieve switching time below 40 psec. The fabrication of such a device is very simple. However, the sensitivity is low (~$3x10^{-4}$ collecting efficiency).

5.3 Integrated Laser Array, Translasers and Integrated Repeaters

When higher power optical source is required in a system application, an integrated array of synchronous lasers can satisfy the power requirement while retaining the compactness of the source. Bell Laboratories and Mitsubishi Electric both have achieved the integration of more than fifteen synchronous lasers on a chip. Wide application of this type of integration is expected in the near future.

It is also desirable from cost standpoint to integrate the laser together with its driving transistor.

Amnon Yariv and his associates at Caltech have been working on this prospect for several years. Both MESFET[10] and bipolar[11] (Figure 5-16) approaches have been experimented with GaAlAs material. A typical common emitter current gain of 900 and a 60 mA laser threshold current were reported.

The natural development following the translasers would be integrating the photodetective function with the regeneration function, i.e., integrated repeaters (Figure 5-17). This is especially useful to the optical video production switcher (Chapter 3), where we suffer large signal attenuation due to the "1 to N" switching. The Caltech group has done significant work in this area[12]. However, array integration has not been attempted, which is necessary for application in large network switching systems such as our video production switcher.

Table 5-1

COMPARATIVE LED DATA

Material	Wavelength (μm)	Quantum Efficiency (%)	Highest Emitted Power (mW)	Radiance (W/cm -Sr) at [current] (mA)	Maximum Modulation Bandwidth (MHz)
GaAs (HOMO, S.E.)	0.9	~1%	-	25[300]	450[a]
InGaAs (HOMO, S.E.)	1.06	~1%	-	15[100]	150[a]
InGaAsP/InP (DH) (S.E.)	1.2	3%	~6 mW	50[100]	90[a]
AlGaAs (DH, S.E.)	0.85	7.6%	14 mW	100[150]	10[b]
AlGaAs (DH, E.E.)	0.85	~1%	8 mW	1000[4000]	200[a]
AlGaAs (DH, S.E.)	0.82	~3%	15 mW	200[300]	17[a]

Code: HOMO - Homojunction; DH - double-heterojunction; S.E. - Surface-emitter with etched well (Burrus type); E.E. - Edge-emitter; (a) - 3 dB reduction in optical power; and (b) - 6 dB optical power reduction.

Figure 5-1 The output power vs. input current characteristics of an GaAlAs/GaAs LED at various operating temperatures.

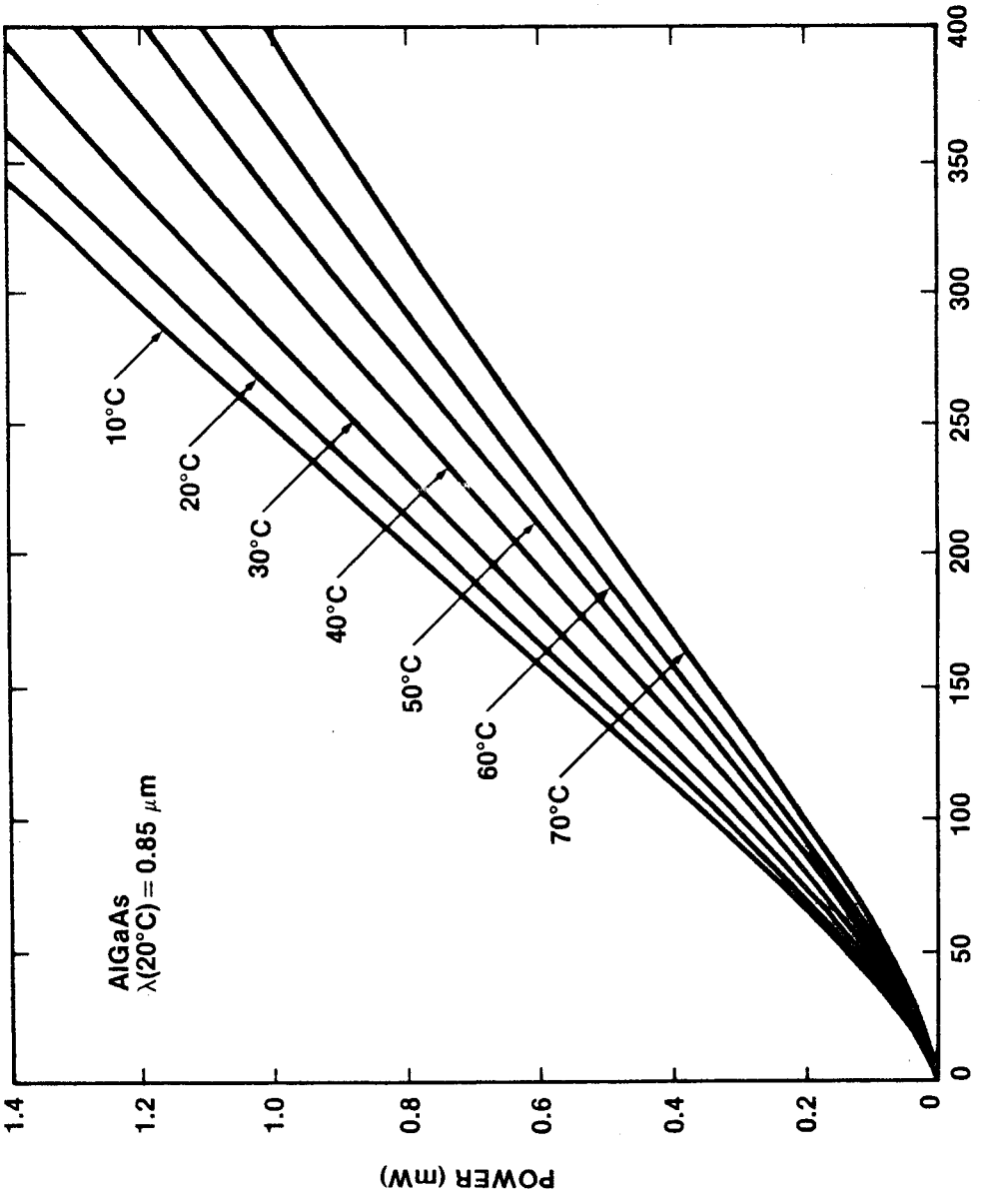
AlGaAs
λ(20°C) = 0.85 μm
10°C
20°C
30°C
40°C
50°C
60°C
70°C
POWER (mW)
0
0.2
0.4
0.6
0.8
1.0
1.2
1.4
0
50
100
150
200
250
300
350
400

Figure 5-2 The output power vs. input current characteristics of an (InGa)(AsP)/InP LED at various operating temperatures.

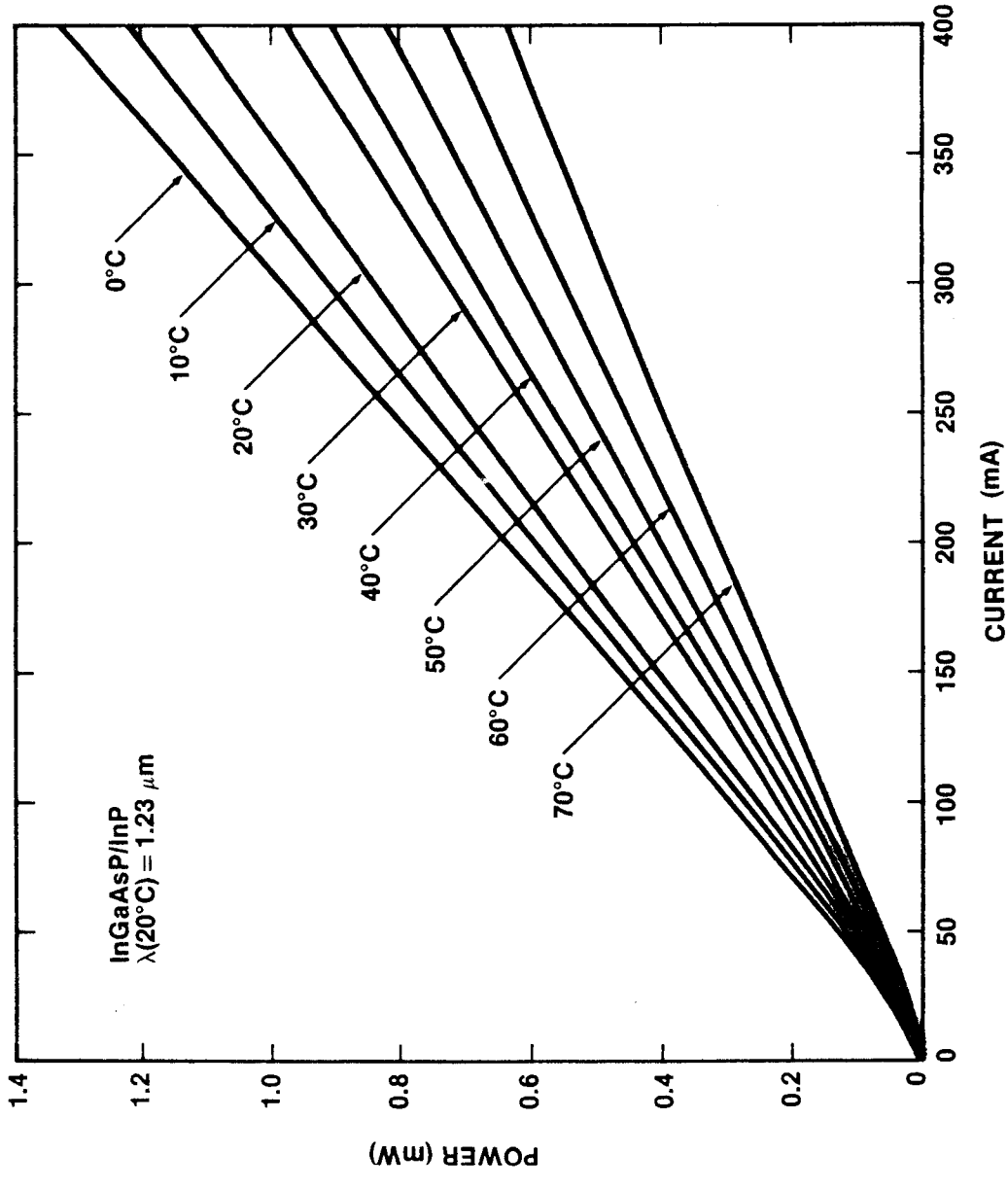
InGaAsP/InP
λ(20°C) = 1.23 μm
0°C
10°C
20°C
30°C
40°C
50°C
60°C
70°C
POWER (mW)
CURRENT (mA)
0
0.2
0.4
0.6
0.8
1.0
1.2
1.4
50
100
150
200
250
300
350
400

Figure 5-3 The output power vs. input current characteristics of a GaAlAs/GaAs double heterostructure laser at various operating temperatures.

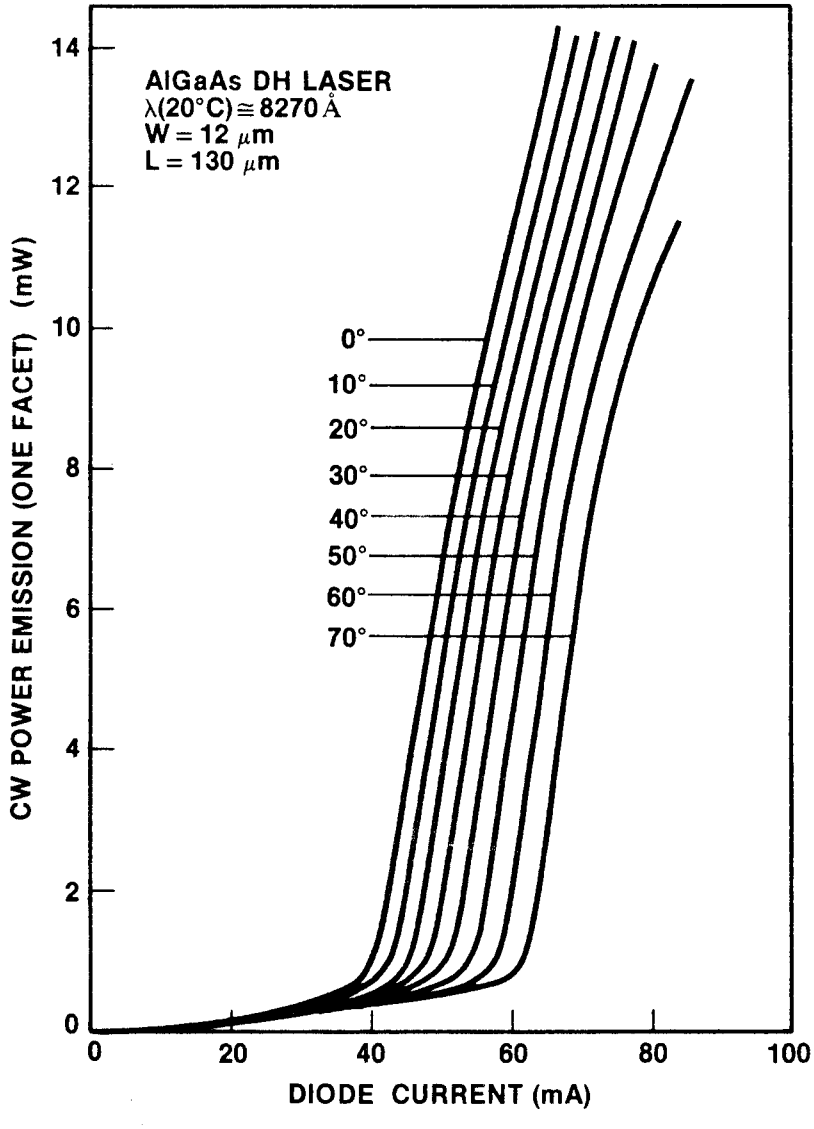
AlGaAs DH LASER
λ(20°C)≅8270 Å
W = 12 μm
L = 130 μm
0°
10°
20°
30°
40°
50°
60°
70°
CW POWER EMISSION (ONE FACET) (mW)
DIODE CURRENT (mA)
0
2
4
6
8
10
12
14
0
20
40
60
80
100

Figure 5-4 The output power vs. input current characteristics of an (InGa)(AsP)/InP laser at various operating temperatures.

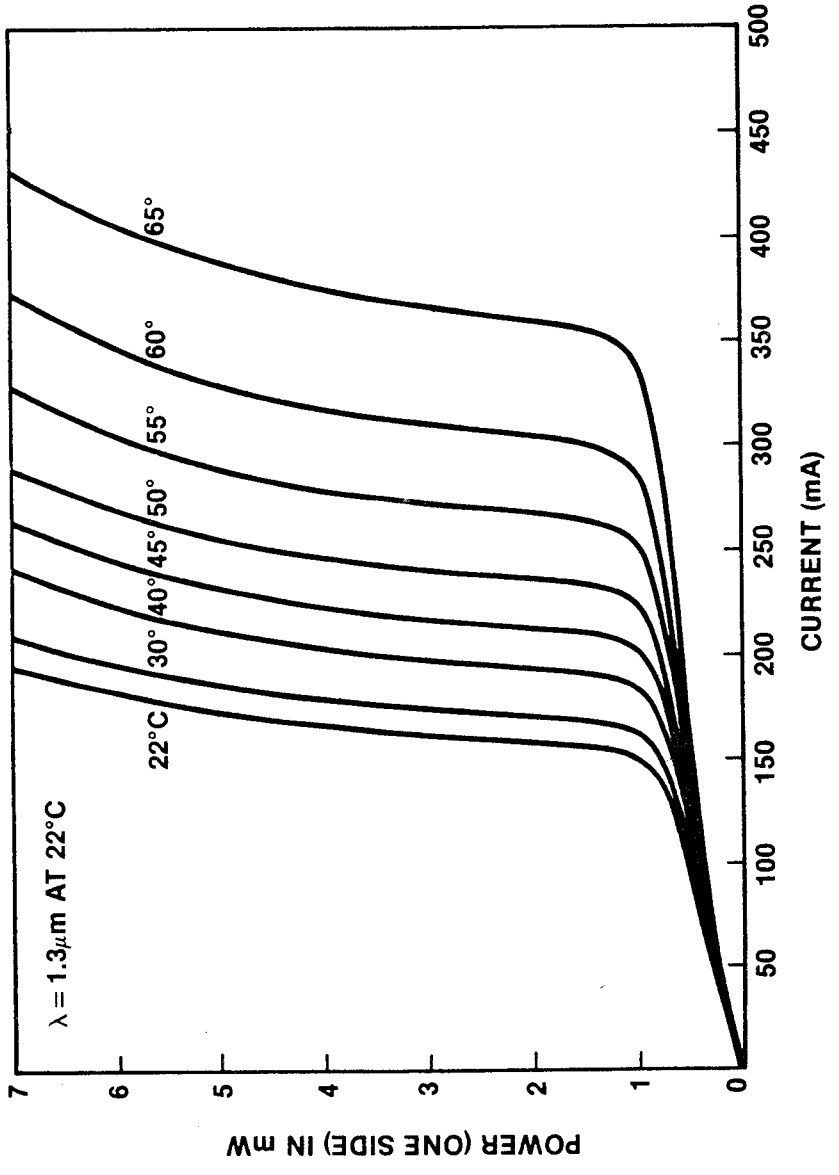
POWER (ONE SIDE) IN mW
0
1
2
3
4
5
6
7
CURRENT (mA)
50
100
150
200
250
300
350
400
450
500
22°C
30°
40°
45°
50°
55°
60°
65°
λ = 1.3μm AT 22°C

Figure 5-5 Temperature dependence of threshold current and external quantum efficiency of a Mitsubishi Electric GaAlAs/GaAs transverse junction stripe laser diode.

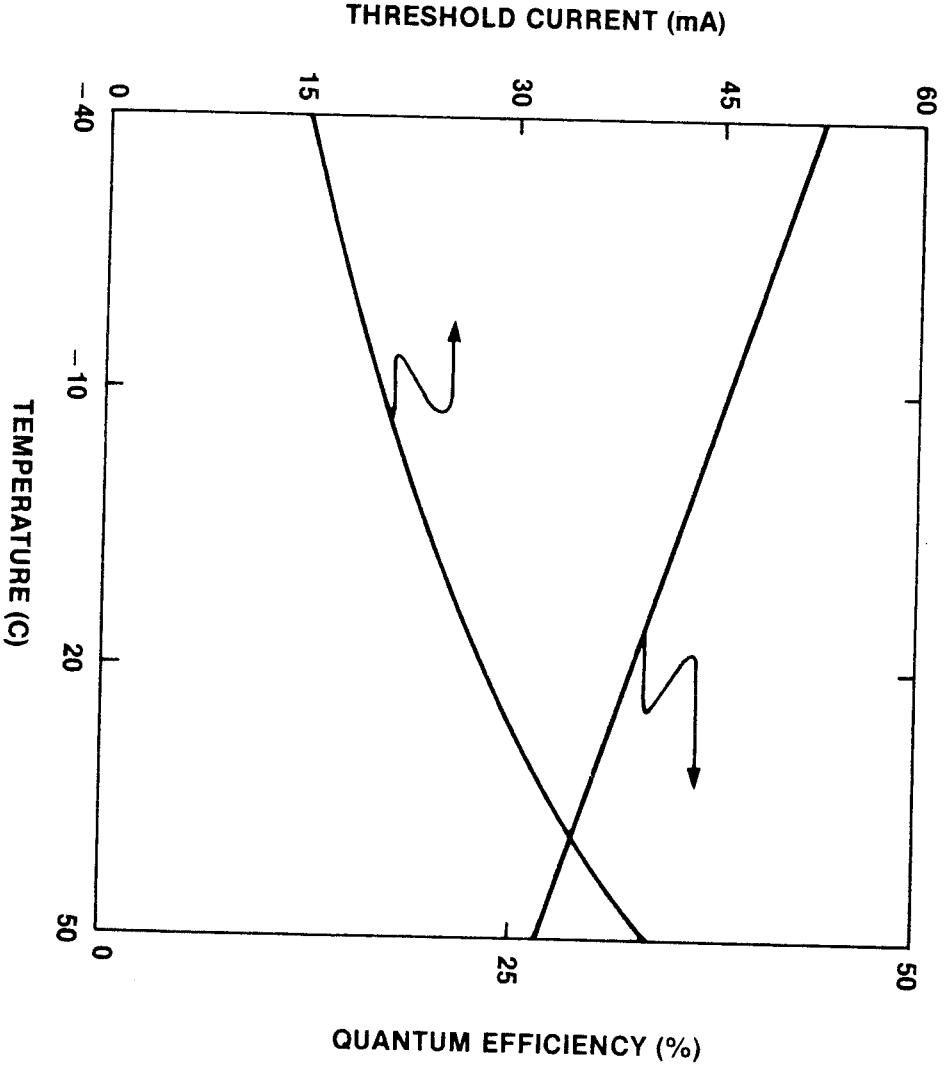
THRESHOLD CURRENT (mA)
0
15
30
45
60
-40
-10
20
50
TEMPERATURE (C)
0
25
50
QUANTUM EFFICIENCY (%)

Figure 5-6 The responsivity vs. wavelength characteristics of photodetectors at assumed values of quantum efficiences.

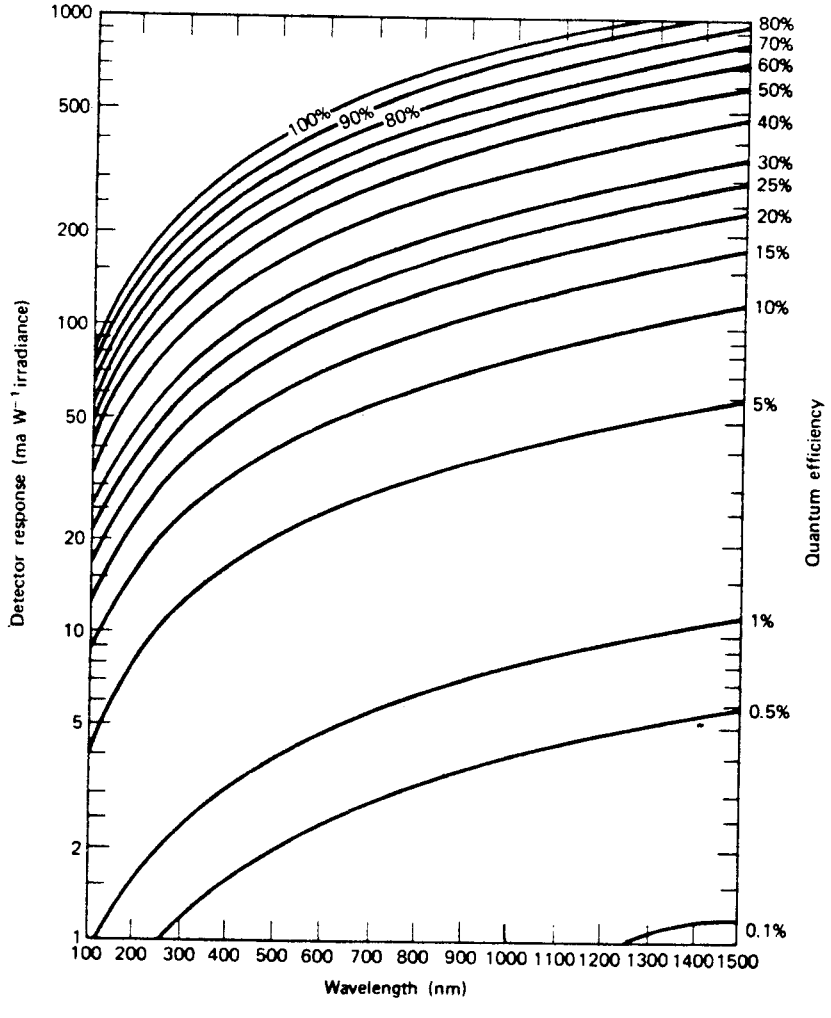
Detector response (ma W⁻¹ irradiance)
1000
500
200
100
50
20
10
5
2
1
100%
90%
80%
80%
70%
60%
50%
40%
30%
25%
20%
15%
10%
5%
1%
0.5%
0.1%
Quantum efficiency
100 200 300 400 500 600 700 800 900 1000 1100 1200 1300 1400 1500
Wavelength (nm)

Figure 5-7 Responsivity and associated quantum efficiency versus wavelength characteristics of a Mitsubishi Electric silicon avalanche photodiode.

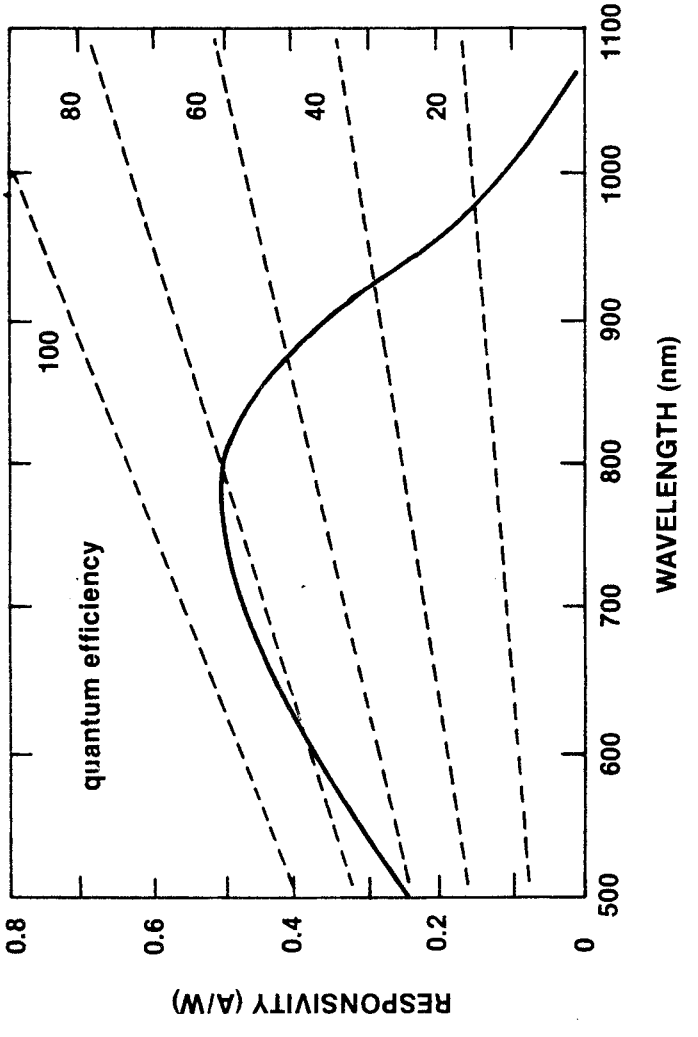
RESPONSIVITY (A/W)
0.8
0.6
0.4
0.2
0
500
600
700
800
900
1000
1100
WAVELENGTH (nm)
quantum efficiency
100
80
60
40
20

Figure 5-8 Schematic diagram of a p-n junction photodiode.

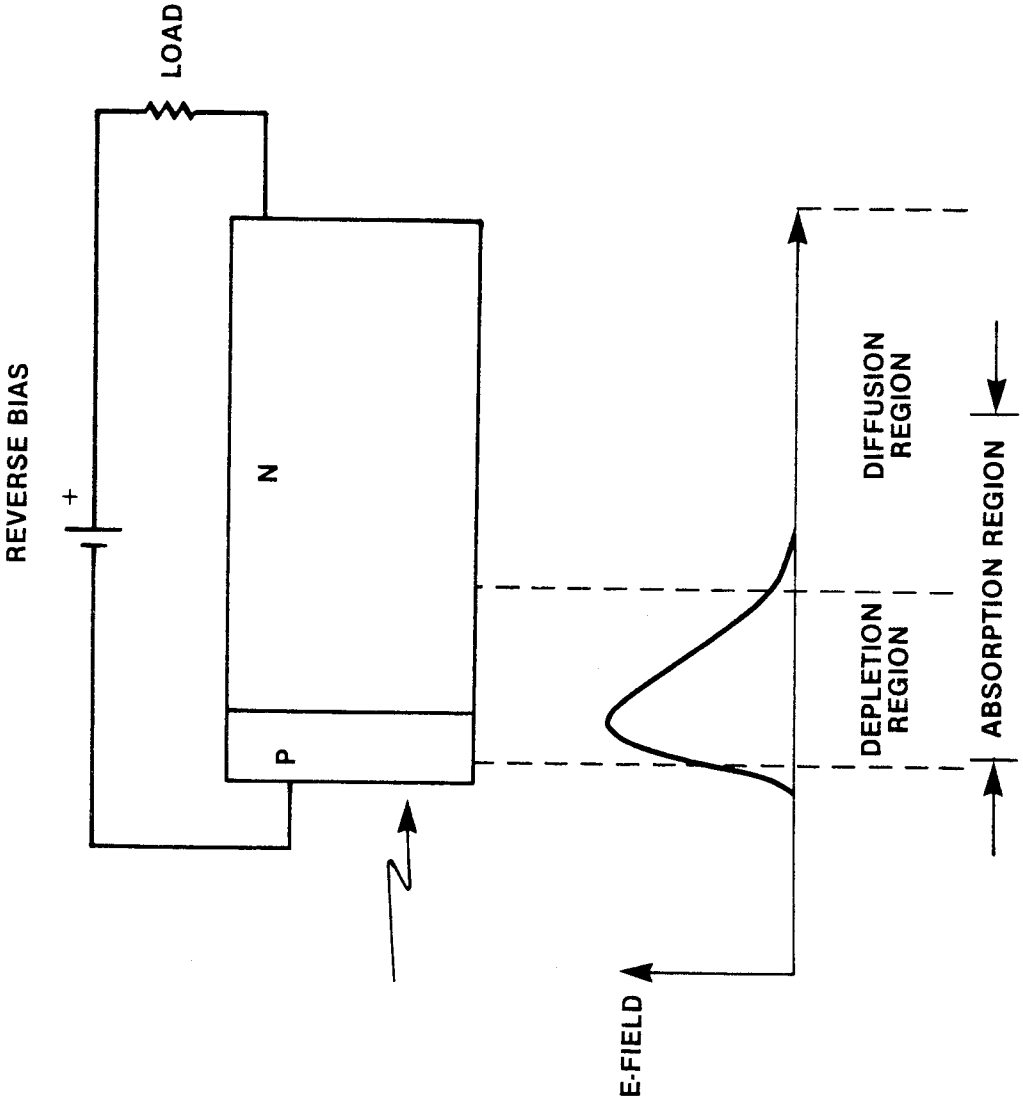
LOAD
REVERSE BIAS
+
N
P
E-FIELD
DIFFUSION REGION
DEPLETION REGION
ABSORPTION REGION

Figure 5-9 Typical p-i-n photodiode geometry.

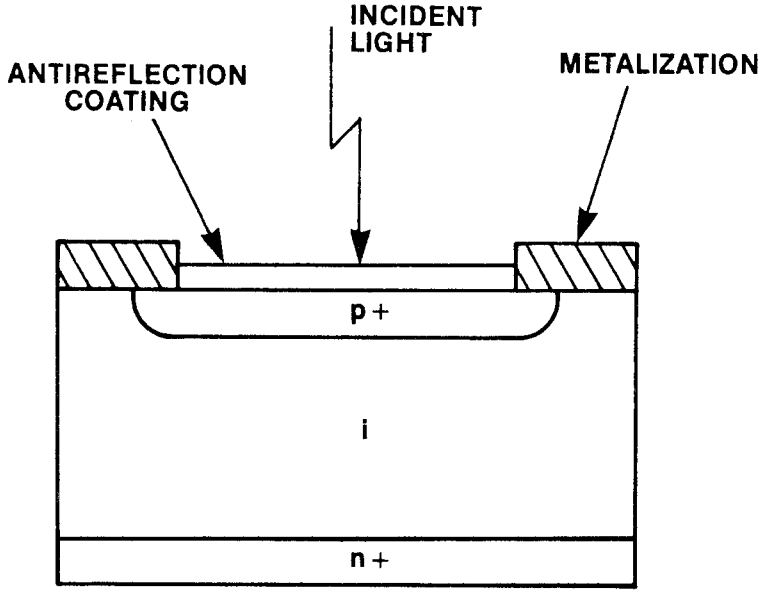
INCIDENT
LIGHT
ANTIREFLECTION
COATING
METALIZATION
p+
i
n+

Figure 5-10 Typical avalanche photodiode geometry.

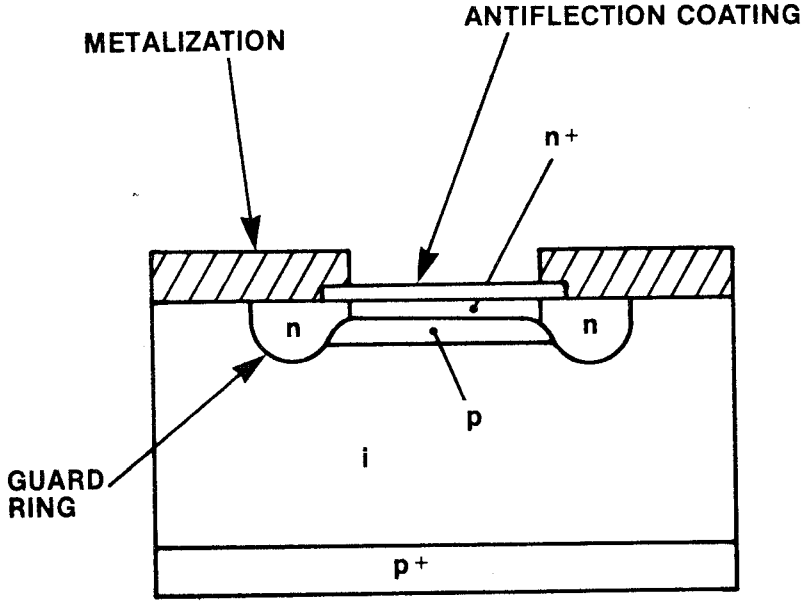
METALIZATION
ANTIFLECTION COATING
n+
n
n
p
i
GUARD
RING
p+

Figure 5-11 The spectral responsivity and quantum efficiency of typical high speed p-n and p-i-n photodiodes.

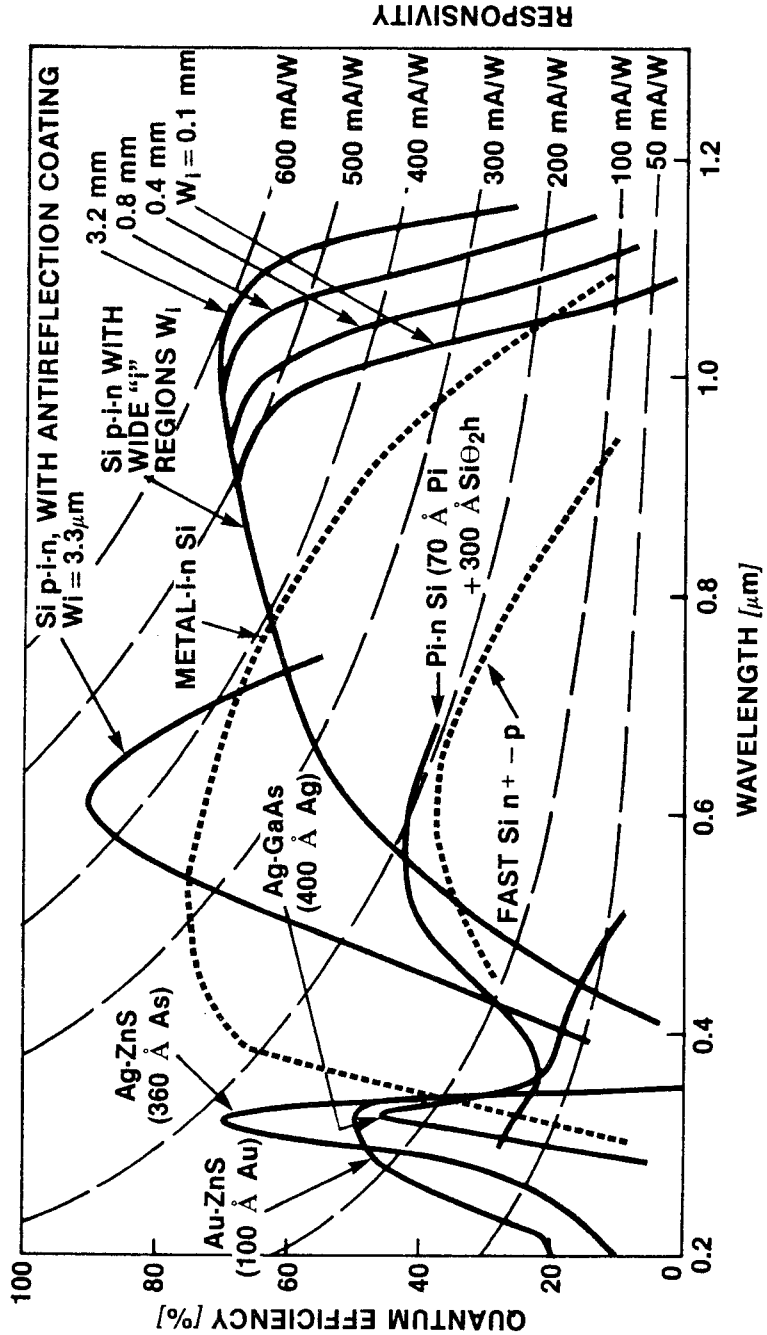
RESPONSIVITY
QUANTUM EFFICIENCY [%]
WAVELENGTH [μm]
100
80
60
40
20
0
0.2
0.4
0.6
0.8
1.0
1.2
600 mA/W
500 mA/W
400 mA/W
300 mA/W
200 mA/W
100 mA/W
50 mA/W
3.2 mm
0.8 mm
0.4 mm
W_i = 0.1 mm
Si p-i-n WITH WIDE "i" REGIONS W_i
Si p-i-n, WITH ANTIREFLECTION COATING Wi = 3.3μm
METAL-i-n Si
Pi-n Si (70 Å Pi + 300 Å SiO2h
FAST Si n+ – p
Ag-GaAs (400 Å Ag)
Ag-ZnS (360 Å As)
Au-ZnS (100 Å Au)

Figure 5-12 The responsivity vs. bias voltage of a typical avalanche photodiode at various operating temperatures.

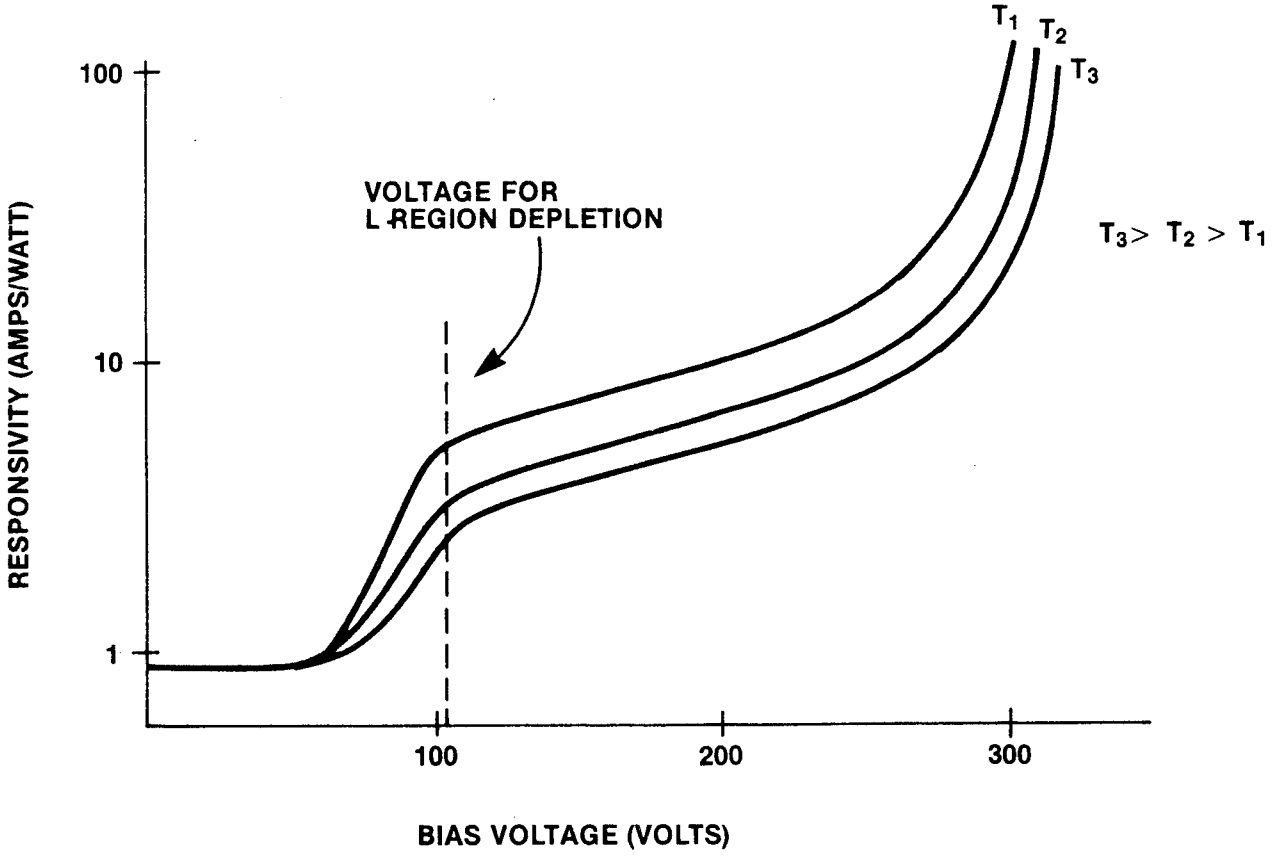

FIG. 5.12 RESPONSIVITY VS VOLTAGE FOR A TYPICAL APD

Figure 5-13 Experimental and calculated results of internal quantum efficiency dependence on n+ layer thickness of germanium avalanche photodiodes, as a function of light wavelength.

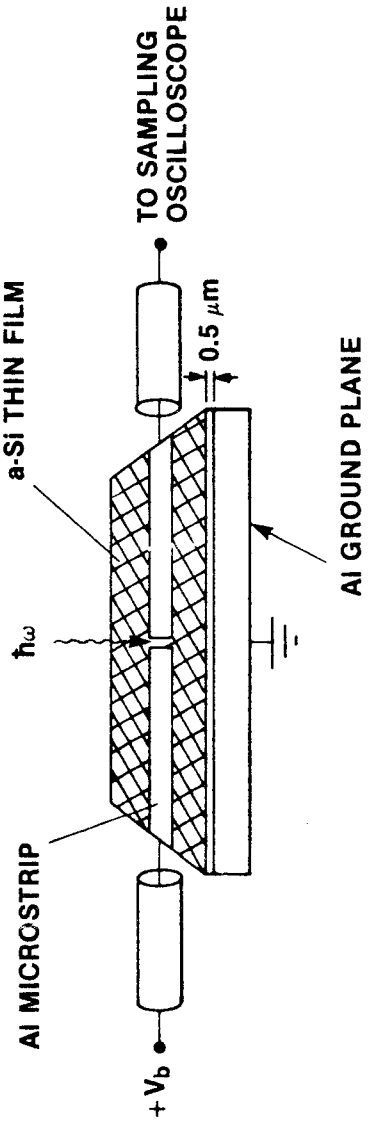
TO SAMPLING OSCILLOSCOPE
0.5 μm
a-Si THIN FILM
hω
Al GROUND PLANE
Al MICROSTRIP
+Vb

Figure 5-14 Photoresponse of $Ga_{0.47}In_{0.53}As$, a direct bandgap photodiode with an absorption edge at 1.7 μm. The spectral response is shown for:

(a) direct incidence, and

(b) through the substrate.

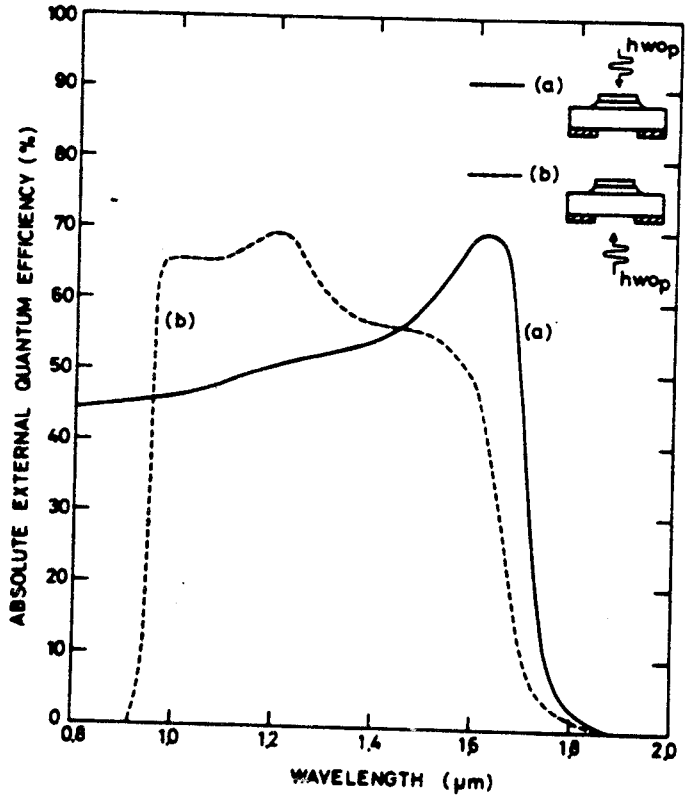
ABSOLUTE EXTERNAL QUANTUM EFFICIENCY (%)
WAVELENGTH (μm)
(a)
(b)
hwop
hwop
100
90
80
70
60
50
40
30
20
10
0
0.8
1.0
1.2
1.4
1.6
1.8
2.0

Figure 5-15 Schematic drawing of amorphous silicon photodetector geometry. The end-on electrodes formed a microstrip transmission line. A small gap in the centre was used as the active area of the detector.

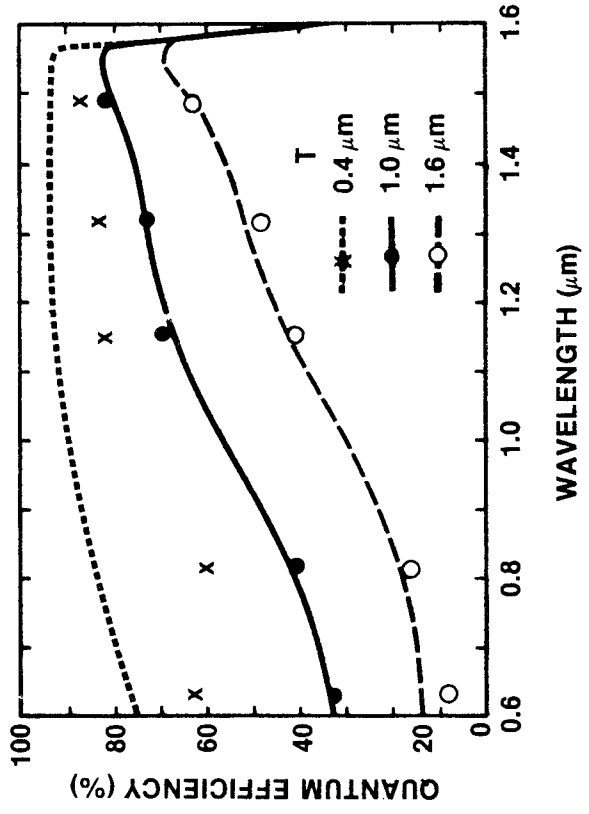
QUANTUM EFFICIENCY (%)
100
80
60
40
20
0
0.6
0.8
1.0
1.2
1.4
1.6
WAVELENGTH (μm)
T
0.4 μm
1.0 μm
1.6 μm

Figure 5-16 Monolithically integrated transistor-laser (translaser) formed by Be ion implantation.

(a) Schematic diagram of the device.

(b) Cross section of the device structure.

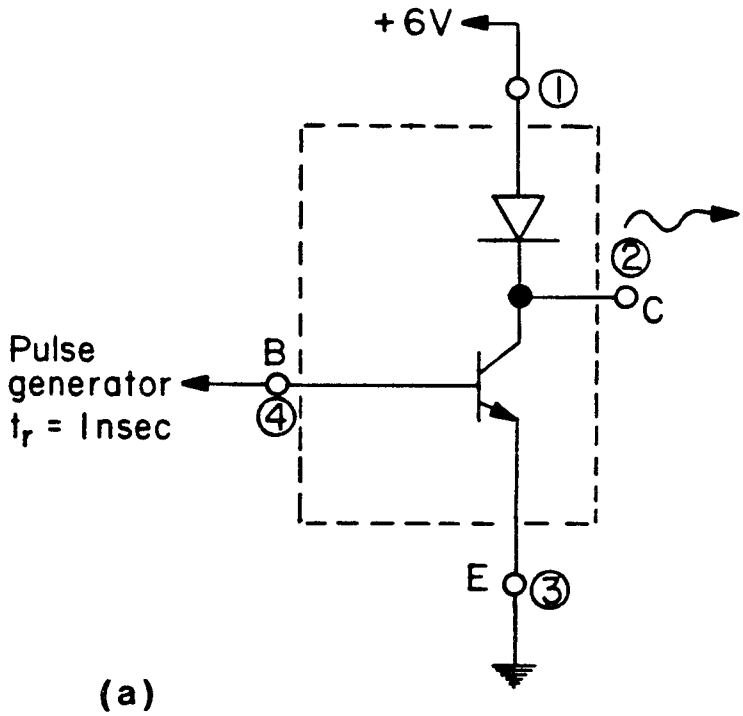
+6V
①
②
C
Pulse
generator
t_r = Insec
B
④
E
③

(a)

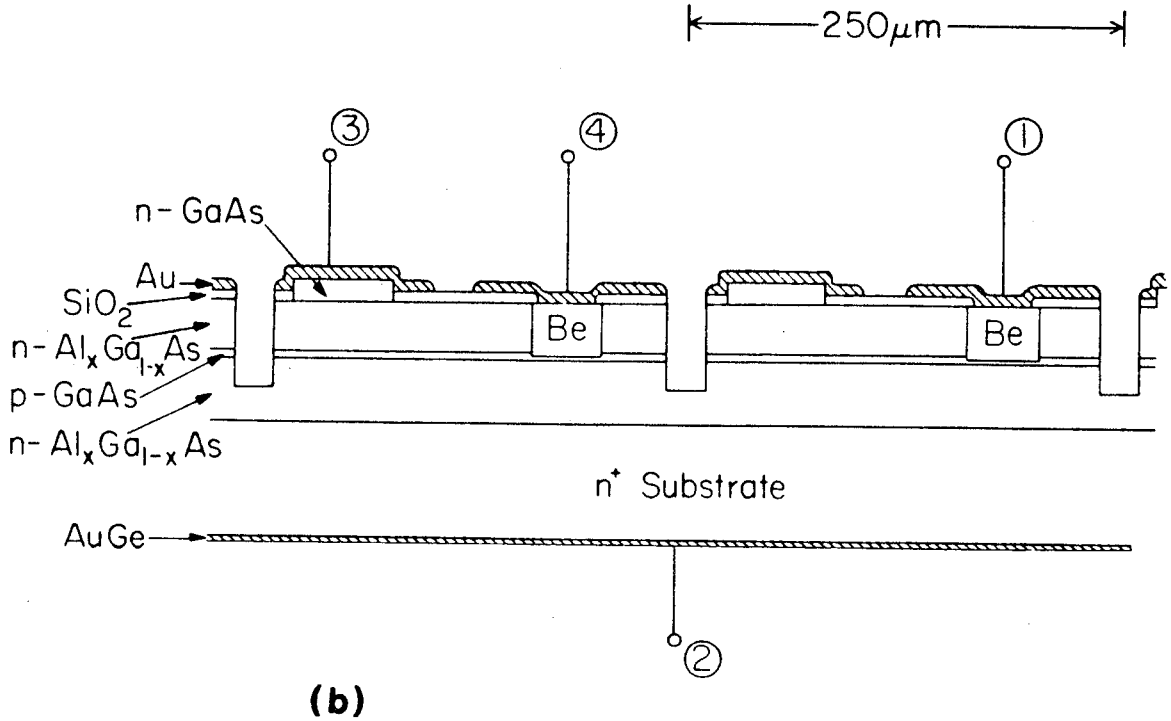
250μm
③
④
①
n-GaAs
Au
SiO_2
n-$Al_xGa_{1-x}As$
p-GaAs
n-$Al_xGa_{1-x}As$
Be
Be
n^+ Substrate
AuGe
②

(b)

Figure 5-17 Monolithically integrated optical repeater.

(a) Schematic diagram of the repeater and external bias sources.

(b) Schematic view of the device structure.

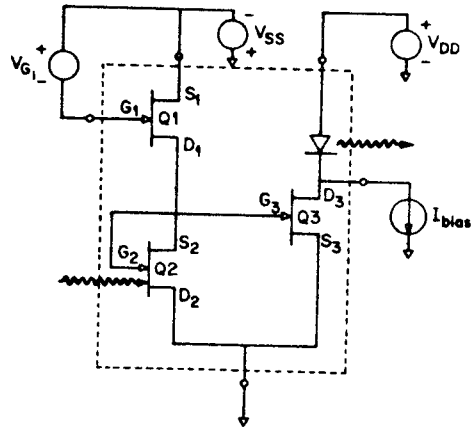
V_{G_1}
V_{SS}
V_{DD}
S_1
G_1
Q1
D_1
G_3
D_3
Q3
S_3
I_{bias}
G_2
S_2
Q2
D_2

(a)

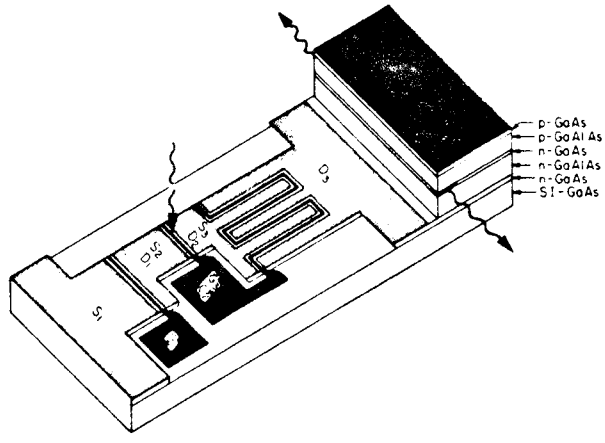
p-GaAs
p-GaAlAs
n-GaAs
n-GaAlAs
n-GaAs
SI-GaAs
Q_3
G_3
D_3
S_3

(b)

REFERENCE LISTING - CHAPTER 5

1. J.J. Hsieh, C.C. Shen, "GaInAsP-InP Double-Hererostructure Lasers for Fiber Optic Communications," Fiber and Integrated Optics, Vol. 1, No. 4, p. 357, 1977.
2. R.E. Nohory, M.A. Pollack, W.D. Johnston, Jr., R.L. Barns, "Bandgap Versus Composition and Demonstration of Vagar's Law for $In_{1-x}GaAs_yP_{1-y}$ Lattice Matched to InP," Applied Phys. Lett., Vol. 33, No. 7, p. 659, October 1978.
3. H. Nishi et al., "Self-Aligned Structure InGaAsP/InP DH Lasers," Appl. Phys. Lett., Vol. 35, No. 2, p. 232, August 1979.
4. T. Murotani et al., "InGaAsP/InP Buried Crescent Laser Emitting at 1.3 μm with Very Low Threshold Current," Electron. Lett., Vol. 16, No. 14, p. 566, July 1980.
5. Y. Itaya, Y. Saematzu, S. Katayama, K. Kishino and S. Arai, "Low Threshold Current Density (100) GaInAsP/InP Double Heterostructure Lasers for Wavelength 1.3 μm," Japan. J. Appl. Physics, Vol. 18, No. 9, p. 1759, September 1979.
6. P.D. Greene, G.D. Henshall, "Growth and Characteristics of GaInAsP/InP Double Heterostructure Lasers," Solid State and Electron Devices, Vol. 3, No. 6, p. 174, November 1979.
7. Sections TUA, TUD, "Longwavelength Sources and Detectors," Technical Digest, IOOC '81, San Francisco, California, April 27-29, 1981.
8. Hiroaki Ando et al., "Characteristics of Germanium Avalanche Photodiodes in the Wavelength Region of 1-1.6 μm," IEEE J. Quantum Electronics, Vol. QE-14, No. 11, p. 804, November 1978.
9. D.H. Auston, P. Lavallard, N. Sol and D. Kaplan, "An Amorphous Silicon Photodetector for Picosecond Pulses," Appl. Phys. Lett., Vol. 26, No. 1, p. 66, January 1980.
10. I. Ury, S. Margalit, M. Yust and A. Yariv, "Monolithic Integration of an Injection Laser and A Metal Semiconductor Field Effect Transistor," Appl. Phys. Lett., Vol. 34, No. 7, p. 430, April 1979.
11. J. Katz, N. Bar-Chaim, P.C. Chen, S. Margalit, I. Ury, D. Wilt, M. Yust and A. Yariv, "A Monolithic Translaser Using GaAs/GaAlAs Bipolar Transistor and Heterostructure Laser," to be published.
12. M. Yust, N. Bar-Chaim, S.H. Izadpanah, S. Margalit, I. Ury, D. Wilt, and A. Yariv, "A Monolithically Integrated Optical Repeater," Appl. Phys. Lett., Vol. 35, No. 10, p. 795, November 1979.

APPENDIX A

Fabrication processes of thermodiffused $Ti:LiNbO_3$ thin-film waveguide:

1) Carefully clean $LiNbO_3$ substrate, using additional "spin-scrub" procedure.
2) Evaporate 400 Å thick titanium film on the polished side of the $LiNbO_3$ substrate.
3) Load the Ti-coated $LiNbO_3$ substrate into diffusion oven.
4) Bubble Argon through water to achieve a 50% partial pressure.
5) Adjust gas flow to approximately 2 to 3 liters/minute.
6) Ramp oven temperature up slowly to 980° C. (at approximately 200° C./hr. rate). If oven has no ramping capability, slowly push the sample into the oven at intervals, allowing substrate to warm up gradually. It is important that the increase of the substrate temperature be gradual. Otherwise, the thermo stress would shatter the $LiNbO_3$ crystal.
7) Thermodiffuse Ti into $LiNbO_3$ at 980° C. in argon/water vapor (1:1) atmosphere for 5 hours.
8) Cool gradually in oxygen/water vapor (1:1) atmosphere.
9) If channel waveguides are desired, pattern the Ti film with lithographic technique before thermodiffusion.
10) After waveguide is fabricated, electrodes could be deposited for electro-optic applications; or SAW transducers could be fabricated on top of the waveguide.

Bob Miller (extension 5362) is familiar with the substrate cleaning procedures and the electrode and SAW transducer processes.

Bob Zimmerman (extension 6392) and **Bob Beckman** are familiar with the Titanium deposition procedure.

Dick Osterman (extension 5237) is familiar with the thermo diffusion procedure.

It is important to avoid contaminants, especially during the sample handling in between the processes.